9620

NAME OF AUTHOR......Shigeo....Mikoshiba...........

TITLE OF THESIS...Electrical...Breakdown.............
.......between..Cylindrical..Electrodes.
.............in....a....Plasma...........

UNIVERSITY.U...of...Alberta.....................

DEGREE FOR WHICH THESIS WAS PRESENTED.....Ph-.D-.........

YEAR THIS DEGREE GRANTED.........1971...................

Permission is hereby granted to THE NATIONAL LIBRARY

OF CANADA to microfilm this thesis and to lend or sell copies

of the film.

The author reserves other publication rights, and

neither the thesis nor extensive extracts from it may be

printed or otherwise reproduced without the author's

written permission.

(Signed)....S. Mikoshiba....

PERMANENT ADDRESS:
.....#4...11606 —132 st.
.....Edmonton....41...
.....Alberta.........

DATED...June...28......1971

THE UNIVERSITY OF ALBERTA

ELECTRICAL BREAKDOWN BETWEEN CYLINDRICAL ELECTRODES IN A PLASMA

by

Ⓒ SHIGEO MIKOSHIBA

A THESIS

SUBMITTED TO THE FACULTY OF GRADUATE STUDIES

IN PARTIAL FULFILMENT OF THE REQUIREMENTS FOR THE DEGREE

OF DOCTOR OF PHILOSOPHY

DEPARTMENT OF ELECTRICAL ENGINEERING

EDMONTON, ALBERTA

FALL, 1971

UNIVERSITY OF ALBERTA

FACULTY OF GRADUATE STUDIES

The undersigned certify that they have read,
and recommend to the Faculty of Graduate Studies for
acceptance, a thesis entitled "Electrical Breakdown
between Cylindrical Electrodes in a Plasma" submitted
by Shigeo Mikoshiba in partial fulfilment of the
requirements for the degree of Doctor of Philosophy.

....
Supervisor

....

....

....

....
External Examiner

Date...June 14, 1971...   ....

ELECTRICAL BREAKDOWN BETWEEN CYLINDRICAL ELECTRODES IN A PLASMA

ABSTRACT

A breakdown voltage of as low as 40 volts has been observed between cylindrical electrodes immersed in a flowing argon plasma which indicates that some mechanism other than the usual spark discharge mechanism is present. There is strong evidence that at plasma densities in the range 10^9 to 10^{16} cm^{-3}, the breakdown is triggered by electrons ejected from the cathode due to the intense electric field in the cathode sheath. Another is the high concentration of neutral particles in the boundary layer around the electrode surface. The exact theory of this phenomenon is presented and shows good agreement with experimental measurements.

It is hoped that the results presented in this thesis will be applicable to the reignition mechanism after current zero of a.c. circuit breakers and to the triggering mechanisms of unipolar arcs, vacuum gaps and short gaps.

During the course of this research a new technique of measuring the electrical conductivity as well as new theories for the variation of the electromagnetically driven plasma velocity and for the ion current collection of a probe aligned parallel to the collision dominated plasma flow were developed.

ACKNOWLEDGEMENTS

TABLE OF CONTENTS

CHAPTER VI   EXPERIMENTS ON THE BREAKDOWN BETWEEN CYLINDRICAL ELECTRODES

IN A PLASMA

CHAPTER VII   DISCUSSIONS ON THE BREAKDOWN THEORY AND EXPERIMENTS

LIST OF TABLES

LIST OF FIGURES

LIST OF SYMBOLS AND PHYSICAL CONSTANTS

In this thesis MKSA practical units will be used throughout unless otherwise stated. The symbols used frequently are listed below. Some of them will be used in different specifications, which will be noted from time to time.

$A = \dfrac{m}{m_H}$ — particle weight normalized by the weight of proton; $A=40$ for Ar and $A=1/1836$ for electron

$c_1 = \sqrt{\dfrac{\gamma P_1}{\rho_1}} = \sqrt{\dfrac{\gamma k T_1}{m}}$ — sound speed in an undisturbed region in the shock tube; $c_1=321$ m/s for Ar at 300°K

$D_a = \dfrac{k(T_i + T_e)}{m_i \nu_i}$ — ambipolar diffusion coefficient; $D_a=0.036$ m^2/s for Ar$^+$ at $T_i = T_e = 10^4$°K and 1 mmHg

$D_i = \dfrac{k T_i}{m_i \nu_i} \propto \dfrac{1}{n_0}$ — diffusion coefficient for ions

$d = r_s - r_p$ — sheath thickness

$e = 1.602 \times 10^{-19}$ — electronic charge

I — electric current in Amperes

j — electric current density in A/m^2

$j_d = Z n_i e \sqrt{\dfrac{Z k T_e}{e m_i}}$ — ion saturation current density when $T_e \gg T_i$; $j_d = 1.4 \times 10^{-18} n_e \sqrt{T_e}$ for Ar$^+$

$j_e = n_e e \sqrt{\dfrac{k T_e}{2 \pi m_e}}$ — electron random current density; $j_e = 2.48 \times 10^{-16} n_e \sqrt{T_e}$

j_i — ion saturation current density; $j_i = j_d$ or j_r or ... etc.

$j_r = Z n_i e \sqrt{\dfrac{k T_i}{2 \pi m_i}}$ — ion random current density; $j_r = 0.92 \times 10^{-18} n_i \sqrt{T_i}$ for Ar$^+$

J — electric current per unit length in A/m

$k = 1.38 \times 10^{-23}$ — Boltzmann constant

L — length of electrostatic probe (or electrode)

m	mass of particle
$m_e = 9.11 \times 10^{-31}$	mass of electron
$m_H = 1.673 \times 10^{-27}$	mass of proton
$M = u_2/c_1$	normalized particle velocity behind the shock front
$M_1 = U/c_1$	Mach number of incident shock front
n	number density of particles in m^{-3}
	$n(m^{-3}) = 3.22 \times 10^{22} p(mmHg) \times 300/T(°K)$
N	number of particles per unit length in m^{-1}
P_1	initial pressure in the shock tube
Q_e	momentum transfer collision cross section of neutrals for electrons; $Q_e = 7 \times 10^{-21} m^2$ for Ar (Fig. 2.1)
Q_i	ionizing collision cross section for neutrals-electrons (Fig. 5.1)
r_p	radius of electrostatic probes (or electrodes)
r_s	radius of sheath
$Re = \dfrac{\rho u L}{\eta}$	hydrodynamic Reynold's number
$R_E = \dfrac{u L}{Da}$	electric Reynold's number
S	area of probe (electrode) surface
T	temperature
u	particle velocity
U	speed of shock front
$\bar{v} = \sqrt{\dfrac{8kT_i}{\pi m_i}}$	average speed; $\bar{v} = 22.9\sqrt{T_i}$ for Ar
$v_p = \sqrt{\dfrac{2kT_i}{m_i}}$	most probable speed; $v_p = 20.3\sqrt{T_i}$ for Ar
V_b	breakdown voltage
V_c	energy bank capacitor charging voltage
V_d	applied voltage between floating double probes

$V_f = \frac{kT_e}{e} \ln \frac{j_e}{j_i}$ floating potential

V_i ionization potential; $V_i = 15.69$ for Ar

V_p probe potential with respect to plasma

z distance from the shock driver mouth

z ionic charge

α degree of ionization

α first Townsend ionization coefficient

α_e ion-electron recombination coefficient;

$\alpha_e = 2 \times 10^{-16}$ m^3/sec for Ar^+

$\gamma = \frac{f+2}{f}$ specific heat ratio; $\gamma = 5/3$ for Ar   (f is the degree of freedom; f=3 for monatomic gas and f=5 for diatomic gas)

γ secondary electron emission coefficient

$\varepsilon_0 = 8.855 \times 10^{-12}$ permittivity of vacuum

η frictional viscosity (Fig. 4.6)

$\lambda \propto \frac{1}{n_0}$ mean free path between neutrals-neutrals of a kind;

$\frac{\lambda(T)}{\lambda(T_0)} = \frac{T_0 + C}{T_0} \cdot \frac{T}{T+C}$,   where C is the Sutherland constant. For Ar C=170°K (when T<600°K) and at 1 mmHg, $\lambda(0°C) = 8.1 \times 10^{-5}$ m and $\lambda(300°K) = 8.4 \times 10^{-5}$ m

$\lambda_D = \sqrt{\frac{\varepsilon_0 k T_e}{e^2 n_e}} = 69\sqrt{\frac{T_e}{n_e}}$ Debye's shielding distance

$\lambda_e = \frac{1}{n_e Q_e}$ mean free path between electrons and neutrals;

$\lambda_e = 4\sqrt{2}\lambda$, except for rare gases. For Ar, $\lambda_e = 4.0 \times 10^{-3}$ m at 0°C and 1 mmHg

$$\lambda_i \propto \frac{1}{n_0}$$

mean free path of ions in their own neutral gas $\lambda \leq \lambda_i \leq \sqrt{2} \lambda$. The factor $\sqrt{2}$ applies when

$$\bar{v}_{ion} \gg \bar{v}_{neutral}$$

$$\mu_0 = 4\pi \times 10^{7}$$

permeability of vacuum

$$\mu_i = \frac{e}{m_i \nu_i} \propto \frac{1}{n_0 \sqrt{T_0}}$$

ion mobility; $\mu_i = 0.12$ m^2/V·sec for Ar^+ in Ar at 0°C, 1 mmHg

$$\nu_i = \frac{\bar{V_i}}{\lambda_i} = n_0 Q_i \bar{V_i} \propto n_0 \sqrt{T_0}$$

momentum transfer collision frequency for ions and neutrals. $\nu_i = 2.0 \times 10^7$ sec^{-1} for Ar^+ in Ar at 0°C and 1 mmHg

$$\rho = nm$$

mass density

$$\sigma$$

electrical conductivity

$$\chi = \frac{eV}{kT_e}$$

normalized voltage

$$\omega_p = \sqrt{\frac{e^2 n_e}{\varepsilon_0 m_e}} = 56.4 \sqrt{n_e}$$

plasma frequency

$$\omega_{pi} = \sqrt{\frac{e^2 n_i}{\varepsilon_0 m_i}} = 1.32 \sqrt{\frac{n_i}{A}}$$

ion plasma frequency

Subscripts

0	quantities of neutral particles
1	quantities in initial conditions
2	quantities in incident shocks
3	quantities in reflected shocks
5	quantities in stagnated shocks
W	quantities at the wall of electrode

CHAPTER I   INTRODUCTION

In the course of plasma density measurements with floating
double Langmuir probes in a high density plasma, it was found that
at an applied voltage between the probes greater than a certain
critical value depending on the plasma density, a sudden increase
in the probe current, which cannot be explained by the existing probe
theories, was observed. From its current-voltage characteristics it
was deduced that this current increase was due to electrical
breakdown between probes. The breakdown voltage, however, was very
different from that predicted by the well known Paschen's Law (as low
as 40 volts was observed), which indicated that some mechanism other
than the Paschen breakdown mechanism was responsible. The same low
voltage breakdown phenomena in high density plasmas have also frequently
been observed at many other laboratories.

We find a similar and a very important example of this breakdown
phenomena in a plasma in a reignition after current zero of alternating-
current circuit interrupting devices. During the post arc period, i.e.,
during a few microseconds after current zero the gas conductivity
between the electrodes is quite high due to the heat generated by
the previous arc. If the ionization of the interelectrode gas is
sufficient the recovery voltage may break down the gap and re-establish
the arc.

Another important example occurs in a high density, high

temperature plasma in contact with an insulated metal wall. As the temperature increases, the floating potential of the wall becomes higher (negatively) than the ionization potential of the ambient gas and the unipolar arc (arc which joins a metallic electrode (cathode) to a plasma (anode)) can be established (1.1).

Electrical breakdown of vacuum insulation is a problem of considerable practical importance owing to the increasingly widespread application of so-called vacuum insulation in high voltage devices such as particle accelerators, x-ray tubes, high frequency low-loss condensers, etc. Field emission and charged particle accumulation in front of the cathode are often responsible for this kind of breakdown and so the breakdown mechanism for this case is similar to the one discussed here. (In the case of vacuum breakdown the neutral gas is generated by the vaporization of anode material.)

The importance of a study of the electrical strength of gases with high ionization and high temperature is, therefore, clear. Nevertheless the works of Sharbaugh et.al.(1.2) and Lee et.al. (1.3) seem to be the only existing studies on the breakdown phenomena in the plasma. In their studies, however, the range of the charged particle density was not wide (0.1-4×10^{10} cm^{-3}), the neutral density not known, and so an exact theory was not given. Thus it is an urgent requirement to measure the breakdown voltages as a function of the plasma density and also to develop a theoretical explanation.

As is usual in any electrical breakdown experiment , there are many factors to be taken into account (e.g. surface conditions of the electrodes, gas-electrode interactions, charged particle effects, etc.) for the development of a breakdown theory. Consequently this

thesis deals with the aspects of surface chemistry to solid state physics, as well as plasma physics and gas dynamics, including the boundary layer problems.

An electromagnetically driven shock tube was used for the production of the sample plasma. The plasma thus produced had many desirable properties:

(1) A very wide range of plasma density can be provided ($n_e=10^9$ - 10^{16} cm^{-3}). Below $n_e=10^9$ cm^{-3}, the breakdown mechanism approaches that of Paschen breakdown; i.e., Crowe's theory (1.4) on the effect of space charge on the breakdown voltage becomes applicable. The mechanism in this density region is therefore already known.

(2) A wide range of combinations of plasma and neutral density can be obtained. Since the plasma density and the neutral density are the two ruling factors, this option is important.

(3) Electrons, ions and neutrals are in thermal equilibrium. They are thermalized at the first stage of their acceleration in the shock driver and when being tested, they are in an "after glow" period when a Maxwellian velocity distribution can be expected.

(4) Rankine-Hugoniot relations can be used under some restrictions to evaluate the densities and temperatures of both ionized and neutral particles. This simple and reliable method of determining especially the neutral density cuts the experimental effort considerably.

(5) The plasma has a well defined flow velocity with respect to the electrode system. In many plasmas where electrical breakdown occurs, such as the plasma in the circuit breaker, flash over in an electrical motor, theta-pinched plasma, plasma created by plasma gun, there is a motion of ionized and neutral gas relative to the electrode system

and this flow effect would have a considerable influence on the breakdown voltage. Thus this property is important.

The contents of this book are as follows:

Chapter II The theories of plasma properties and electrostatic probes used in the later part of this thesis are briefly summarized. The first part of the chapter is mainly concerned with the transport phenomena, and the second part with ion sheath current theory and with the modified floating double probe theory which applies to our experimental situations.

Chapter III The apparatus used in this experiment is explained and the diagnostic techniques used are described. In section 3.2.5 a newly developed technique of measuring the plasma conductivity is discussed in detail.

Chapter IV The plasma used in this experiment is examined. In the first half a new model of the electromagnetically driven shock tube is used to derive a theory for the plasma velocity in the shock tube. In the second half the experimentally determined plasma parameters using many diagnostic techniques are tabulated.

Chapter V Many models of the sheath and electrode configuration are examined one by one to provide a solid ground for determining the most appropriate theory to account for the breakdown mechanism between electrodes in the plasma.

Chapter VI The various breakdown measurements are described.

Chapter VII The model of the breakdown mechanism based on the theories in Chapter V is developed and compared with the results in Chapter VI. This is also compared with existing theories and

experimental results.

The numerical solutions which appear frequently in this thesis were carried out using the IBM 360 computer at the University of Alberta with either Fortran IV or APL languages.

(1.1) A.E. Robson and P.C. Thonemann: Proc. Phys. Soc. $\underline{73}$ 502 (1959)
       D.W. George and P.H. Richards: Brit. J. Appl. Phys. $\underline{1}$ 1171 (1968)
(1.2) A.H. Sharbaugh, P.K. Watson, D.R. White, T.H. Lee & A. Greenwood:
       A.I.E.E. Trans. Pt. III, P.A.S. $\underline{80}$ 333 (1961)
(1.3) T.H. Lee, A.N. Greenwood & D.R. White: I.E.E.E. Trans. P.A.S. $\underline{84}$
       1116 (1965)
(1.4) R.W. Crowe, J.K. Bragg & V.G. Thomas: Phys. Rev. $\underline{96}$ 10 (1954)

CHAPTER II   PLASMA PROPERTIES AND ELECTROSTATIC PROBES

2.1 ELECTRICAL CONDUCTIVITY OF PLASMA

2.1.1 Slightly Ionized Gas

Consider a Lorentzian gas where ions are neglected. Minority particles (electrons) lose momentum by colliding with the majority particles (neutrals) having a collision frequency of ν_m. If ν_m can be considered to be independent of electron energy, the mobility (μ) and diffusion constant (D) can be derived from the Boltzmann equation as,

$$\mu = \frac{e}{m_e \nu_m} \qquad \text{and} \qquad D = \frac{\overline{v^2}}{3\nu_m} .$$

(2.1)

If the electrons have a Maxwellian velocity distribution, we find that the mean free path of electrons in neutrals can be expressed as,

$$\lambda_e = \frac{1}{n_0 Q_e} = \frac{\overline{v}}{\nu_m} = \frac{1}{\nu_m}\sqrt{\frac{8 k T_e}{\pi m_e}} ,$$

(2.2)

where Q_e and n_0 are the collision cross section of the neutrals for scattering electrons and the neutral molecule number density, respectively. Therefore Eq. 2.1 becomes,

$$\mu = \frac{\sqrt{\pi}\, e}{\sqrt{8 m_e k T_e}\, n_0 Q_e}$$

(2.3)

$$D = \frac{k T}{m \nu_m} = \frac{\sqrt{\pi k T}}{\sqrt{8 m_e}\, n_0 Q_e} .$$

(2.4)

Now the electrical conductivity takes the form, $\sigma = n_e e \mu$. This

was calculated for the case of a slightly ionized gas of rigid elastic spherical molecules by Chapman and Cowling (2.1) more rigorously with their results that,

$$\sigma = \frac{1.132 \times 3\sqrt{\pi}\, n_e\, e^2}{8\sqrt{2 m_e k T_e}\ n_0 Q_e} = 3.85 \times 10^{-12} \frac{n_e}{n_0 Q_e \sqrt{T_e}} \quad (mhos/m). \qquad (2.5)$$

The values of Q_e for argon were obtained by Townsend and Bailey (2.2) and shown in Fig. 2.1.

2.1.2 Fully Ionized Gas

If an electron with velocity v encounters an ion, the electron is scattered by the Coulomb force. The collision frequency for momentum transfer is obtained by using the laws of conservation of momentum and angular momentum, as,

$$\nu_m = \frac{n_i Z^2 e^4 \ln \Lambda}{4\pi \varepsilon_0^2 m_e^2 v^3}, \qquad (2.6)$$

where Λ is the ratio of Debye's shielding distance, λ_D, and the impact parameter, b_0. For a Maxwellian distribution,

$$\Lambda = \frac{\lambda_D}{b_0} = \frac{12\pi (\varepsilon_0 k T)^{\frac{3}{2}}}{Z e^3 \sqrt{n_e}}. \qquad (2.7)$$

When the electron temperature exceeds about $4 \times 10^5 \,^\circ K$, Λ must be reduced because of quantum mechanical effects by a factor of $(4.2 \times 10^5/T)^{\frac{1}{2}}$.

The mobility can be found as in the case of a slightly ionized gas, except that neutral particles are replaced by ions, with a different collision frequency which is now largely dependent on v, as,

$$\mu = \frac{64\sqrt{2\pi}\,\varepsilon_o^2\,(kT)^{\frac{3}{2}}}{Z^2 e^3 n_i \ln\Lambda} \,. \tag{2.8}$$

To obtain an accurate expression for σ in an ionized gas, electron-electron encounters must be taken into account. The result given by Spitzer and Harm (2.3) may be expressed in the form,

$$\sigma = \gamma_E n_e e \mu = \frac{2.63\times10^{-2}\,\gamma_E\,T^{\frac{3}{2}}}{Z \ln\Lambda} \quad (mhos/m), \tag{2.9}$$

with the expression of Eq. 2.8, where values of γ_E which depends on the ionic charge, Z, are given as,

Z	1	2	4	16	∞
γ_E	0.583	0.683	0.785	0.923	1

Thus in the important case of $Z=1$, we have,

$$\sigma = 1.53\times10^{-2}\,\frac{T^{\frac{3}{2}}}{\ln\Lambda} \quad (mhos/m). \tag{2.10}$$

The results obtained above are based on the assumption that the electric field is sufficiently small so that the potential energy gained across one mean free path is negligible compared to kT.

(2.1) S. Chapman and T.G. Cowling: "The Mathematical Theory of Non-Uniform Gases" Cambridge Univ. Press, London Secs. 18.12, 14.12 and 10.53 (1960)
(2.2) J.S. Townsend and V.A. Bailey: Phil. Mag. 43 593 (1922), 44 1033 (1922)
(2.3) L. Spitzer & R. Harm: Phys. Rev. 89 977 (1953)
L. Spitzer: "Physics of Fully Ionized Gases"

2.1.3 Moderately Ionized Gas

For the electrical conductivity of a moderately ionized gas, the approximation of

$$\frac{1}{\sigma} = \frac{1}{\sigma_c} + \frac{1}{\sigma_d}$$ (2.11)

can be used, where σ_c is the conductivity of a slightly ionized gas (Eq. 2.5) where the close encounters between the electrons and the neutral particles dictate the electron mobility, and σ_d is the conductivity of a completely ionized gas (Eq. 2.9) where the distant encounters between the ions and electrons dominate the situation. By comparing the relative magnitude of the close and distant encounter terms for argon, the two terms σ_c and σ_d will be equal at about 7000°K, or a degree of ionization of about 10^{-4}. At temperatures higher than about 8000°K ($\alpha > 10^{-3}$), the close encounter term will become so insignificant that the resultant conductivity will be practically the same as σ_d.

FIG. 2.1   Effective elastic

collision cross section of argon

atoms for scattering electrons as

a function of electron temperature

(2.2).
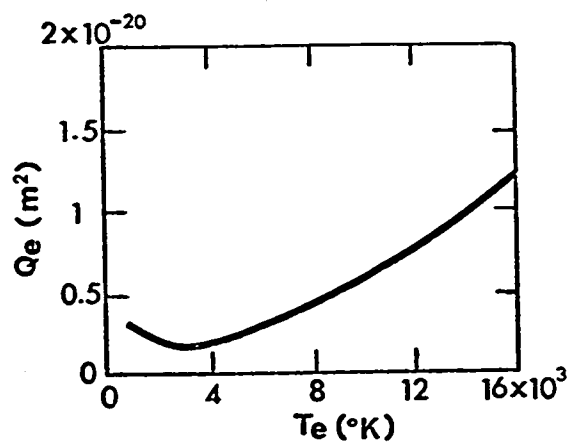
FIG. 2.2 $\Lambda(\tau)$ of Eq. 2.57 (2.15).
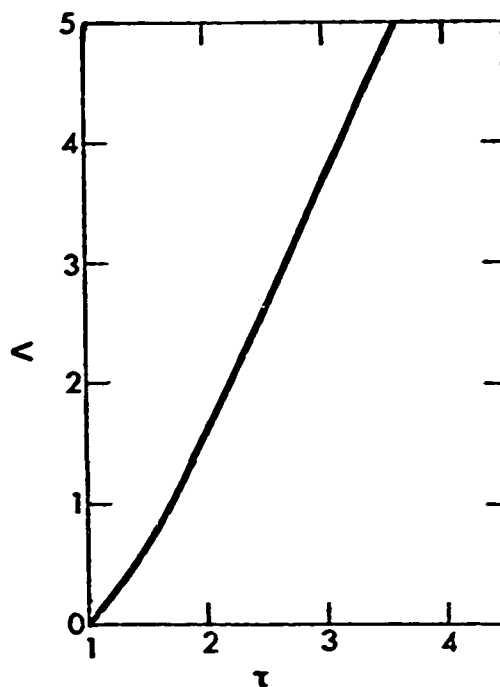
2.2 TRANSPORT PHENOMENA OF PLASMA

2.2.1 Self-Collision Time

The self-collision time, t_c, is defined by $1/2\nu_m$ when the test particle is the same kind as the field particles, and the test particle has a velocity of $(3kT/m_f)^{\frac{1}{2}}$, as (2.4),

$$t_c = \frac{6\sqrt{3}\,\pi\varepsilon_o^2\,\sqrt{m}\,(kT)^{3/2}}{nZ^4 e^4\, \ln\Lambda\,\left(\Phi(\sqrt{1.5}) - G(\sqrt{1.5})\right)} = \frac{11.4\times10^6\, A^{\frac{1}{2}}\, T^{\frac{3}{2}}}{nZ^4\, \ln\Lambda}\quad (\text{sec}) \qquad (2.12)$$

Here we have let m equal to Am_H, where m_H is the mass of unit atomic weight. t_c provides a measure both of the time required to reduce substantially any lack of isotropy in the velocity distribution and also of the time required for the distribution of kinetic energies to approach the Maxwellian distribution. The value of t_c determines also the value of γ to be used for computing T in an adiabatic compression. If the compression is slow compared to t_c, γ equals 5/3 (three dimensional compression). For compression more rapid than t_c, γ will equal 2 or 3 depending on whether the compression is perpendicular to the lines of magnetic force (two dimensional compression) or parallel to magnetic force (one dimensional compression).

2.2.2 Equipartition Time for Charged Particles

Let us suppose that the test particles and the field particles

---

(2.4) S. Chandrasekhar: "Principles of Stellar Dynamics" Univ. of Chicago Press (1942)

both have Maxwellian velocity distributions, but with different kinetic temperatures T and T_f. The rate at which equipartition of energy is established between two groups of particles is called the time of equipartition and expressed by Spitzer (2.5) as,

$$t_{eq} = \frac{3\sqrt{2}\,\pi^{\frac{3}{2}}\varepsilon_o^2\, m m_f k^{\frac{3}{2}}}{n_f Z^2 Z_f^2 e^4 \ln\Lambda} \cdot \left(\frac{T}{m} + \frac{T_f}{m_f}\right)^{\frac{3}{2}}$$

$$= 5.87 \times 10^6 \frac{A A_f}{n_f Z^2 Z_f^2 \ln\Lambda} \left(\frac{T}{A} + \frac{T_f}{A_f}\right)^{\frac{3}{2}}. \tag{2.13}$$

For a proton-electron mixture,

$$\frac{t_c(\text{proton})}{t_c(\text{electron})} \approx 43 \qquad \frac{t_{eq}}{t_c(\text{proton})} = 43 \qquad \frac{t_{eq}}{t_c(\text{electron})} = 1836. \tag{2.14}$$

2.2.3 Equipartition Time for Ions and Electrons with Neutral Particles

In the case of a center collision between an ion and a neutral particle of the same kind, they exchange their total energies. If we average the energy exchange rate with respect to collision parameter between ions and neutrals, it becomes approximately half of the value of the rate in the case of center collisions. During Δt, an ion experiences $v_i \Delta t / \lambda_i$ collisions with neutrals, so that the total ion energy per unit volume at $t + \Delta t$ is,

$$\frac{3}{2} n_i k T_i (t + \Delta t) = \frac{3}{2} n_i k T_i(t) - \frac{T_i - T_m}{2} \frac{3}{2} n_i k \frac{\overline{v_i}}{\lambda_i} \Delta t \tag{2.15}$$

and for neutral particles,

$$\frac{3}{2} n_o k T_m (t + \Delta t) = \frac{3}{2} n_o k T_m(t) + \frac{T_i - T_m}{2} \frac{3}{2} n_i k \frac{\overline{v_i}}{\lambda_i} \Delta t. \tag{2.16}$$

(2.5) L. Spitzer: Monthly Notices, Roy. Astron. Soc. (London) **100** 396 (1940)

By solving these equations with the boundary conditions that $T_i(0)=T_{i0}$ and $T_m(0)=T_{m0}$, we obtain,

$$T_i(t) = \frac{\alpha T_{io} + T_{mo}}{1+\alpha} + \frac{T_{io} - T_{mo}}{1+\alpha} e^{-\frac{\overline{V_i}}{2\lambda_i}(1+\alpha)t} \qquad (2.17)$$

$$T_m(t) = \frac{\alpha T_{io} + T_{mo}}{1+\alpha} - \frac{\alpha(T_{io} - T_{mo})}{1+\alpha} e^{-\frac{\overline{V_i}}{2\lambda_i}(1+\alpha)t}, \qquad (2.18)$$

where α is the degree of ionization. The time of equipartition for ions and neutrals of the same kind can then be expressed as,

$$t_{eq} = \frac{2\lambda_i}{\overline{V_i}(1+\alpha)} = \sqrt{\frac{\pi m_i}{2kT_i}} \frac{\lambda_i}{1+\alpha} = 1.38 \times 10^{-2} \sqrt{\frac{A}{T_i}} \frac{\lambda_i}{1+\alpha}. \qquad (2.19)$$

The last two terms of the above equation are valid only when ions have a Maxwellian velocity distribution.

From the classical theory the energy loss of an electron due to a collision with a neutral particle is (2.6),

$$\Delta E = \frac{8}{3} \frac{m_e}{m_n} \left(1 - \frac{T_n}{T_e}\right) \frac{3}{2} kT_e. \qquad (2.20)$$

Here, it is assumed that the kinetic energy of the particles is much smaller than the internal energy. By constructing the same kind of equations as Eqs. 2.15 and 2.16 for electron-neutral collisions we find that the time of equipartition for electrons and neutral particles is,

$$t_{eq} = \frac{3 m_n \lambda_e}{8 m_e \overline{V_e}(1+\alpha)} = 0.111 \frac{A \lambda_e}{(1+\alpha)\sqrt{T_e}}. \qquad (2.21)$$

2.2.4 Time Dependent Ambipolar Diffusion

For the ambipolar diffusion of ions and electrons in a plasma consisting predominantly of neutral particles, the following equations

---

(2.6) A.M. Cravath: Phys. Rev. $\underline{36}$ 248 (1930)

can be obtained from the Boltzmann equation,

$$\Gamma_i = -D_i \nabla n_i + n_i \mu_i E - \frac{1}{\nu_{mi}} \frac{\partial \Gamma_i}{\partial t} \qquad (2.22)$$

$$\Gamma_e = -D_e \nabla n_e - n_e \mu_e E - \frac{1}{\nu_{me}} \frac{\partial \Gamma_e}{\partial t} \qquad (2.23)$$

and

$$\Gamma_i = \Gamma_e \equiv \Gamma, \quad n_i = n_e \equiv n. \qquad (2.24)$$

By eliminating E, we obtain,

$$\Gamma = -D_a \nabla n - \frac{1}{\nu_a} \frac{\partial \Gamma}{\partial t}, \qquad (2.25)$$

where

$$D_a = \frac{D_i \mu_e + D_e \mu_i}{\mu_e + \mu_i} \simeq \frac{k(T_e + T_i)}{m_i \nu_{mi}} \qquad (2.26)$$

and

$$\nu_a = \frac{\nu_{me} \nu_{mi} (\mu_e + \mu_i)}{\nu_{mi} \mu_i + \nu_{me} \mu_e} \simeq \nu_{mi}. \qquad (2.27)$$

Here D_a is an ambipolar diffusion constant and ν_a is an ambipolar momentum transfer collision frequency.

Plasma diffusion in a cylinder of radius r_0 and length L, as a function of position and time is now considered. From the law of continuity,

$$\nabla \cdot \Gamma + \frac{\partial n}{\partial t} = 0 \qquad (2.28)$$

and Eq. 2.25 we obtain, in a cylindrical coordinate, with $\partial/\partial\theta = 0$

$$\nabla^2 n = \frac{1}{r} \frac{\partial n}{\partial r} + \frac{\partial^2 n}{\partial r^2} + \frac{\partial^2 n}{\partial z^2} = \frac{1}{D_a} \frac{\partial n}{\partial t} + \frac{1}{\nu_a D_a} \frac{\partial^2 n}{\partial t^2}. \qquad (2.29)$$

By putting $n = R(r)Z(z)T(t)$ and with the boundary conditions that $n=0$ at $z = \pm L/2$ and/or $r = r_0$, the above equation can be solved as,

$$n = n_0 J_0 \left(\frac{2.405}{r_0} r \right) \cos \left(\frac{\pi}{L} z \right) \left\{ (\alpha + \nu_a) e^{\alpha t} - (\beta + \nu_a) e^{\beta t} \right\}, \qquad (2.30)$$

where $J_0(x)$ is a Bessel function of 0th order of the first kind, 2.405 is the first zero of $J_0(x)$ and

$$\left. \begin{array}{c} \alpha \\ \beta \end{array} \right\} = \frac{-\nu_a \pm \sqrt{\nu_a^2 - 4\nu_a D_a \left\{ \left(\frac{2.405}{r_0} \right)^2 + \left(\frac{\pi}{L} \right)^2 \right\}}}{2}$$

If $\quad \nu_a \gg 4D_a\left\{\left(\frac{2.405}{r_0}\right)^2+\left(\frac{\pi}{L}\right)^2\right\}$, then the equation is reduced to,

$$n = n_0 J_0\left(\frac{2.405}{r_0}r\right)\cos\left(\frac{\pi}{L}z\right)e^{-\frac{t}{\tau_a}}, \qquad (2.32)$$

where $\quad \tau_a = \dfrac{1}{D_a\left\{\left(\frac{2.405}{r_0}\right)^2+\left(\frac{\pi}{L}\right)^2\right\}}$ $\qquad\qquad$ (2.33)

is the life time of the plasma.

2.2.5 Thermal Diffusion

If n_0 particles at r=0, t=0 are in a temperature gradient field, the particle density at (r,t) becomes, in the spherical coordinate (2.7),

$$n(r,t) = \frac{n_0}{(4\pi Dt)^{3/2}}e^{-\frac{r^2}{4Dt}}. \qquad (2.34)$$

Generally the life time, τ_T, can be approximated by

$$\tau_T = \frac{L^2}{2fD}, \qquad (2.35)$$

where L is the characteristic length and f is the degree of freedom. The root mean square displacement of a particle from its original position at t is,

$$\sqrt{\overline{r^2}} = \sqrt{2fDt}, \qquad (2.36)$$

or, 85% of n_0 is confined within $r < \sqrt{2fDt}$.

(2.7) H. Raether: "Electron Avalanches and Breakdown in Gases"
Butterworth and Co., Ltd. (1964)

2.2.6 Electron-Ion Volume Recombination

The rate of change of electron density due to electron-ion recombination can be expressed as,

$$\frac{dn_e}{dt} = -\alpha_e n_e^2 \tag{2.37}$$

$$\frac{1}{n_e} = \alpha_e t + \frac{1}{n_{e0}} \,, \tag{2.38}$$

where α_e is the electron-ion recombination coefficient and n_{e0} is the density at time zero. By defining the life time of electrons, τ_r, as $n_e(\tau_r) = n_{e0}/2$, then,

$$\tau_r = \frac{1}{\alpha_e n_{e0}} \,. \tag{2.39}$$

In the case of argon, by using the value of $\alpha_e = 2 \times 10^{-16}$ m^3/sec measured by Kenty (2.8),

$$\tau_r = 0.5 \text{ ms} \qquad \text{at } n_{e0} = 10^{19} \text{ m}^{-3}$$

and $\qquad \tau_r = 0.5 \ \mu s \qquad$ at $n_{e0} = 10^{22}$ m^{-3}.

(2.8) C. Kenty: Phys. Rev. 32 624 (1928)
The value of $\alpha_e = 3 \times 10^{-13}$ m^3/sec obtained by M.A. Biondi and S.C. Brown (Phys. Rev. 76 1697 (1949)) seems to be too large.

2.3 ION CURRENT IN A COLLISIONLESS PLASMA

The appropriate theory to use for calculating ion saturation currents
for cylindrical probes in a collisionless plasma is shown in Table 2.1
for various ranges of parameters. $\beta (=E_i/ZkT_e)$ is a normalized ion energy
and χ_p $(=-eV_p/kT_e)$ is a normalized probe potential.

The probe voltage enters here because it affects the distribution of
the electrons. For $\chi_p \gg 1$ the electron distribution may be considered
Maxwellian. For χ_p less than about 1, the quasi-neutral solution holds
everywhere, and probe theory is particularly simple. For $1 < \chi_p < 5$, the
deviation from a Maxwellian distribution due to the loss of electrons to
the probe must be taken into account. Although this poses no problem in
principle, it complicates the computations.

For $\beta \ll 1$, the dependence on ion energy is slight. For $\beta \gg 1$, the
probe current depends primarily on kT_i and is given by Langmuir's sheath
theory for a Maxwellian distribution. The transition case $\beta \simeq 1$ is not well
covered by any simple theory. The simple sheath theory fails because the
accelerating electric field outside the sheath is neglected, and the BR
theory fails because a monoenergetic distribution is no longer a good
approximation.

To avoid the confusion the following notations will be used throughout;

I: current (Amps)

J: current per unit length (A/m)

j: current density (A/m^2).

Ion Energy Distribution	β	$r_p \ll \lambda_D$	$r_p \simeq \lambda_D$		$r_p \gg \lambda_D$		
		all x_p	$x_p \gg 1$	$x_p < 1$	$x_p \gg 1$	$5 > x_p > 1$	$x_p < 1$
Zero Energy	0		LAM		LAM		
Mono Energetic	$\ll 1$	LO	BR	LO	LAM	LAM	LAM
	$\simeq 1$	LO	BR	LO	LAM	LAM	LAM
	$\gg 1$	LO	BR	LO	LS		LO
Maxwellian	$\ll 1$	LO	BR	LO	BR		
	$\simeq 1$	LO	BR		BR		
	$\gg 1$	LO	BR	LO	LS		LO

Table 2.1 The appropriate theory to use for calculation of ion saturation currents.

β and x_p are normalized ion energy and normalized probe potential, respectively. 'LS' stands for Langmuir sheath theory (2.11) (Sec. 2.3.1), 'LO' stands for Langmuir orbital motion theory (2.10) (Sec. 2.3.2), 'LAM' stands for Lam's theory (2.9) (Sec. 2.3.3) and 'BR' stands for Bernstein and Rabinowitzs's theory (2.12).

(2.9) S.H. Lam: Phys. Fluids 8 73 (1965)
(2.10) H.M. Motto-Smith and I. Langmuir: Phys. Rev. 23 727 (1924)
(2.11) I. Langmuir: Phys. Rev. 28 727 (1926)
(2.12) I.B. Bernstein and I. Rabinowits: Phys. Fluids 2 112 (1959)

2.3.1 Langmuir Sheath Theory

The ion current flowing into a cylindrical probe per unit length

is expressed as,

$$J = 2\pi r_s j_r,$$

(2.41)

where r_s is the sheath radius and j_r is the ion random current density

which takes the form shown in the section "List of Symbols". The radius

of the sheath can be found from the Child-Langmuir Law,

$$J = \frac{8\sqrt{2}}{9}\pi\varepsilon_0 \sqrt{\frac{e}{m_i}} \frac{|V_p|^{\frac{3}{2}}}{r_p \beta^2}\left(1 + \frac{2.66}{\sqrt{\eta_p}}\right),$$

(2.42)

where $\eta_p = -eV_p/kT_i$ (not T_e) and β is the solution of

$$3\beta\frac{d^2\beta}{d\gamma^2} + \left(\frac{d\beta}{d\gamma}\right)^2 + 4\beta\frac{d\beta}{d\gamma} + \beta^2 - 1 = 0,$$

(2.43)

with $\gamma = \ln(r_p/r_s)$ (<0). The value of β as a function of r_s/r_p was calculated

by Blodgett (2.13) and shown in the Table III of her paper. The $1+2.66/\sqrt{\eta_p}$

term arises from the fact that the ions have an initial energy given by the

Maxwellian distribution. When the sheath thickness, d, is thin compared

to the probe radius, Eq. 2.42 can be simplified to,

$$J = \frac{8\sqrt{2}\pi\varepsilon_0}{9}\sqrt{\frac{e}{m_i}} \frac{r_p |V_p|^{\frac{3}{2}}}{d^2}\left(1 + \frac{2.66}{\sqrt{\eta_p}}\right) = \frac{3.42\times10^{-7} r_p |V_p|^{\frac{3}{2}}}{\sqrt{A}\, d^2}\left(1 + \frac{2.66}{\sqrt{\eta_p}}\right)$$

(2.44)

and $\beta \simeq \gamma$. The potential distribution inside the sheath for the case is,

$$V(r) = -V_p\left(\frac{r}{d}\right)^{\frac{4}{3}},$$

(2.45)

and the intensity of the electric field at the probe surface can be

found to be larger by a factor of 4/3 than the averaged value of the

---

(2.13) K.B. Blodgett: Phys. Rev. 22 115 (1923)

intensity in the sheath (of V_p/d).

The ion sheath can be formed within a time corresponding to the ion plasma frequency, ω_p, given in the section "List of Symbols". In the case of an argon plasma, this time varies from 0.4 μs ($n_e=10^{10}$ m^{-3}) to 0.4 ns ($n_e=10^{22}$ m^{-3}).

2.3.2 Langmuir Orbital Motion Theory

The ion current flowing into a cylindrical probe per unit length is expressed as,

$$J = 2\pi r_p j_r F \tag{2.46}$$

where

$$F = \frac{r_s}{r_p} \text{erf} \sqrt{\Phi} + (1 - \text{erf} \sqrt{\chi_p + \Phi}) e^{\chi_p},$$

$$\Phi = \frac{r_p^2}{r_s^2 - r_p^2} \chi_p \tag{2.47}$$

$$\text{erf} \chi = \frac{2}{\sqrt{\pi}} \int_0^\chi e^{-t^2} dt.$$

In the limiting case of $r_s - r_p \ll r_p$, $F = r_s/r_p$ and we recover Eq. 2.41. In the practical applications involving small probes and positive ion saturation, we have $r_s \gg r_p$ and $|eV_p/kT_e| \gg 1$. With these conditions Eq. 2.46 becomes,

$$J = 2\pi r_p j_r \frac{r_s}{r_p} \text{erf} \sqrt{\Phi}. \tag{2.48}$$

The sheath size is determined by Eq. 2.42. By equating Eqs. 2.42 and 2.48 we obtain the ion saturation current reaching the probe as (2.14),

$$J = 2\pi r_p j_r \cdot 0.7 \Phi^{0.55} N_r^{-0.2}, \tag{2.49}$$

(2.14) G.J.Schulz and S.C. Brown: Phys. Rev. 98 1642 (1955)

where

$$N_r = \frac{e}{\varepsilon_0} m_i^{\frac{1}{2}} j_r r_p^2 (kT_i)^{-\frac{3}{2}}. \tag{2.50}$$

When the electron temperature is much higher than that of the ions, the drift current density, j_d, reaches the sheath edge, rather than the random current density, j_r. The drift current at the sheath can be taken into account by replacing j_r by j_d and correspondingly, N_r by N_d. With a fixed probe and discharge conditions we obtain,

$$J = 2\pi r_p j_d \cdot 0.7 \Phi^{0.55} N_d^{-0.2} \propto V_p^{0.55} n_e^{0.8}. \tag{2.51}$$

In the thick sheath limit and $\chi_p \gg 1$, Eq. 2.47 becomes,

$$F = \frac{2}{\sqrt{\pi}} \sqrt{\chi_p}, \tag{2.52}$$

and we have,

$$J = 2\sqrt{2} \, r_p n_e e^{\frac{3}{2}} m_i^{-\frac{1}{2}} V_p^{\frac{1}{2}} \propto V_p^{\frac{1}{2}} n_e. \tag{2.53}$$

The slope of J^2 vs V_p yields $8r_p^2 n_e^2 e^3/m_i$, hence the value of n_e.

2.3.3 Lam's theory

To obtain the ion saturation current when $r_p \gtrsim \lambda_D$, we have to consider the potential distribution around the probe. The given equations are:

Boltzmann eq. $\mathbf{v} \cdot \frac{\partial f}{\partial \mathbf{r}} + \frac{Ze\mathbf{E}}{m} \cdot \frac{\partial f}{\partial \mathbf{v}} = 0$

Poisson eq. $\nabla^2 V = -\frac{e}{\varepsilon_0}(Z n_i - n_e)$

Energy eq. $E_\perp = \frac{1}{2} m (\dot{r}^2 + r^2 \dot{\theta}^2) \tag{2.54}$

$E_\parallel = \frac{1}{2} m \dot{z}^2$

Angular momentum eq. $L = m r^2 \dot{\theta}$.

By assuming that the ion energy distribution is monoenergetic ($=E_i$),

Poisson equation reads, in a dimensionless form,

$$\frac{1}{\xi}\frac{d}{d\xi}\left(\xi\frac{d\chi}{d\xi}\right) = 1 - \frac{1}{\pi}\sin^{-1}\frac{\pi J_N}{\xi\sqrt{\beta+\chi}} \qquad \text{for } \xi \geq \xi_0$$

$$= \frac{1}{\pi}\sin^{-1}\frac{\pi J_N}{\xi\sqrt{\beta+\chi}} \qquad \text{for } \xi \leq \xi_0 \qquad (2.54)$$

ξ_0 is the normalized absorption radius and can be found from,

$$\beta+\chi(\xi_0)-\frac{\pi^2 J^2}{\xi_0^2}=0, \qquad \frac{d}{d\xi_0}\left(\beta+\chi(\xi_0)-\frac{\pi^2 J^2}{\xi_0^2}\right)=0. \qquad (2.55)$$

When the ion energy is so small that $|E_i/eV_p| \ll (r_p/\lambda_i)^2$, Poisson equation

is, $$\frac{d}{d\xi}\left(\xi\frac{d\chi}{d\xi}\right) - J\chi^{-\frac{1}{2}} + \xi e^{-\chi} = 0. \qquad (2.56)$$

Here dimensionless parameters are chosen as,

$\xi = r/\lambda_D$ (normalized radius)

$\chi = -eV/kT_e$ (normalized potential)

$\beta = E_i/ZkT_e$ (normalized ion energy)

$\quad = \pi T_i/4ZT_e$ ("   for Maxwellian distribution)

J_i (ion current per unit length)

$J_N = \dfrac{J_i}{6\pi\times10^3 kT_e}\sqrt{\dfrac{m_i}{2n_e Z\varepsilon_0}}$ (normalized ion current)

$J_B = 2\iota_B n_e e r_p\sqrt{2ZkT_e/m_i}$ (Bohm current)

ι_B (normalized Bohm current, a function of β

       only; $\iota_B=1$ when $T_i=0$ and 1.25 when $T_i=ZT_e$)

$\tau = J_i/J_B$ (ion current increment ratio due to finite

       sheath thickness).

These equations were solved by Chen (2.15) with $\beta=0-0.1$. The V_p-J

(2.15) F.F. Chen: J. Nucl. Energy C7 47 (1965)

characteristics and the shape of $V(r)$ for the cylindrical probes when $\beta = 0$ are shown in Figs. 10 and 6 of his paper, respectively. To determine the plasma density one uses the following formula,

$$\Lambda(\tau) = 3.89 \times 10^{-6} |V_P| \left(\frac{Z}{A J_i^2 r_p^2}\right)^{\frac{1}{3}}. \tag{2.57}$$

Having $\Lambda(\tau)$ from the experimental data, one finds τ from Fig. 2.2 (page 10) Knowing τ, we find n_e from J_B.

When r_p and/or n_e is so large that $\xi_p^2 J^2 \gg 9\chi^3$, $(J_i^2 r_p^2 \gg Z e V_p^3 / 2 m_i)$, $\tau \simeq 1$ and the ion saturation current becomes equal to the Bohm current $(J_i = J_B)$ which is independent of V_p. If, in addition, $T_i = T_e$, then

$$J_i = J_B = 3.54 \, r_p n_e e \sqrt{\frac{Z k T_e}{m_i}} \qquad \left(= 8.13 \times 10^{-18} r_p n_e \sqrt{T_e} \quad \text{for Ar}\right). \tag{2.58}$$

The ion saturation current calculated by Schulz and Brown (2.14) is,

$$J_d = 2\pi r_p n_e e \sqrt{\frac{Z k T_e}{\xi m_i}} = 3.81 \, r_p n_e e \sqrt{\frac{Z k T_e}{m_i}}, \tag{2.59}$$

which is only a factor of 1.08 larger than Eq. 2.58. When V_p is not too large, Eq. 2.59 can still be used as an order of magnitude check of the plasma density.

2.4 ION CURRENT IN A COLLISION-DOMINATED PLASMA

When the ionic mean free path becomes shorter than the probe radius, most of the electric field around the probe is confined within the distance of an ionic mean free path from the probe surface. Accordingly the current is essentially limited by the ambipolar diffusion of charges. The ion current can be expressed approximately as,

$$j = e D_a \nabla n_e \simeq e D_a \frac{n_e}{\delta} , \qquad (2.60)$$

where δ is a characteristic length such as a probe radius. This formula can be modified using $D_a = k\mu_i(T_e + T_i)/e$, $\mu_i = e/m_i\nu_i = e\lambda_i/m_i\bar{v}$ and $\bar{v}$ (average speed) $= (8kT_i/\pi m_i)^{\frac{1}{2}}$,

$$j = \frac{1}{4} n_e e \bar{v} \frac{\lambda_i}{\delta} . \qquad (2.61)$$

This expression shows that $n_e \bar{v}/4$ ions enter the sheath, suffer many collisions and finally a proportion λ_i/δ reach the probe surface. This λ_i/δ term can also be expressed, according to Schulz and Brown (2.14) as,

$$\frac{\lambda_i}{\delta} = \frac{3}{2\nu_i t_i} = \frac{3\lambda_i}{2d} , \qquad (2.62)$$

where ν_i is the collision frequency for positive ions, and t_i is the time spent by an unscattered ion in the sheath of thickness d.

The rigorous continuum theory shows that the ion saturation current density is (2.16),

$$J = 1.7 \pi n_e e \frac{T_e}{T_i} \sqrt{\frac{kT_i}{2\pi m_i}} \frac{\lambda_i}{\ln \frac{L}{r_s}} .$$

$$= 2.13 \times 10^{-18} \frac{T_e}{T_i} \frac{n_e \sqrt{T_i} \lambda_i}{\log \frac{L}{r_s}} \qquad (A/m^2) \quad \text{for argon}, \qquad (2.63)$$

(2.16) V.M. Zakharova, Y.M. Kagan, K.S. Mustafin and V.I. Perel: Sov. Phys. Tech. Phys. <u>5</u> 411 (1960)
C.H. Su and R.E. Kiel: J. Appl. Phys. <u>37</u> 4907 (1966)
D.E. Weissman, W.E. Scharfman and H. Guthart: Phys. Fluids <u>10</u> 464 (1967)

where L is the probe length and r_s the sheath radius expressed as (2.17)

$$\frac{r_s}{r_p} = 1 + C_a\left(\left(\frac{T_e}{T_e+T_i}\right)^{\frac{1}{2}} \frac{\lambda_D}{r_p} \chi_p\right)^{0.77} , \qquad (2.64)$$

if $|\chi_p| = |eV_p/kT_e| \gg 1$. C_a is a constant that varies slightly with L/r_p and is equal to 0.56 for $L/r_p = 300$ and is 0.63 for $L/r_p = 100$. The calculated results of r_s/r_p as a function of V for a range of electron densities are shown in Fig. 2.3 when $T_i = T_e = 10^4$ K, $r_p = 0.05$ mm and L=4 cm. The sheath size contains a logarithmic term, so that for cylindrical probes the effect of variation in r_s to the probe current is relatively small.

2.5 ION CURRENT IN A COLLISIONLESS PLASMA FLOW

Electrostatic probes, when used in a plasma flow, show different characteristics from those in a stationary plasma. The electron temperature deduced from the electron retarding region, where the electron current is much larger than the ion current, should be correct as long as $r_p \lesssim \lambda_e$, because of the relative insensitivity of electron collection to the magnitude of the ion-neutral and neutral-neutral mean free paths. Also T_e can be determined uniquely with a probe of any geometry and directional alignment with respect to the flow. This was experimentally verified by Dunn (2.18) and Sonin (2.19).

(2.17) W.E. Scharfman: "Operation of Electrostatic Flush Probes in This Plasma Layers" Stanford Research Institute Project 7712 (Oct. 1969)
(2.18) M.G. Dunn & J.A. Lordi: AIAA Journal 8 1077 (1970)
(2.19) A.A. Sonin: AIAA Journal 4 1588 (1966)

FIG. 2.3   The ratio of the sheath radius to the probe radius as
a function of probe voltage and electron density in a continuum plasma.
$T_i=T_e=10^4$ °K, $r_p=0.05$ mm and L=40 mm.
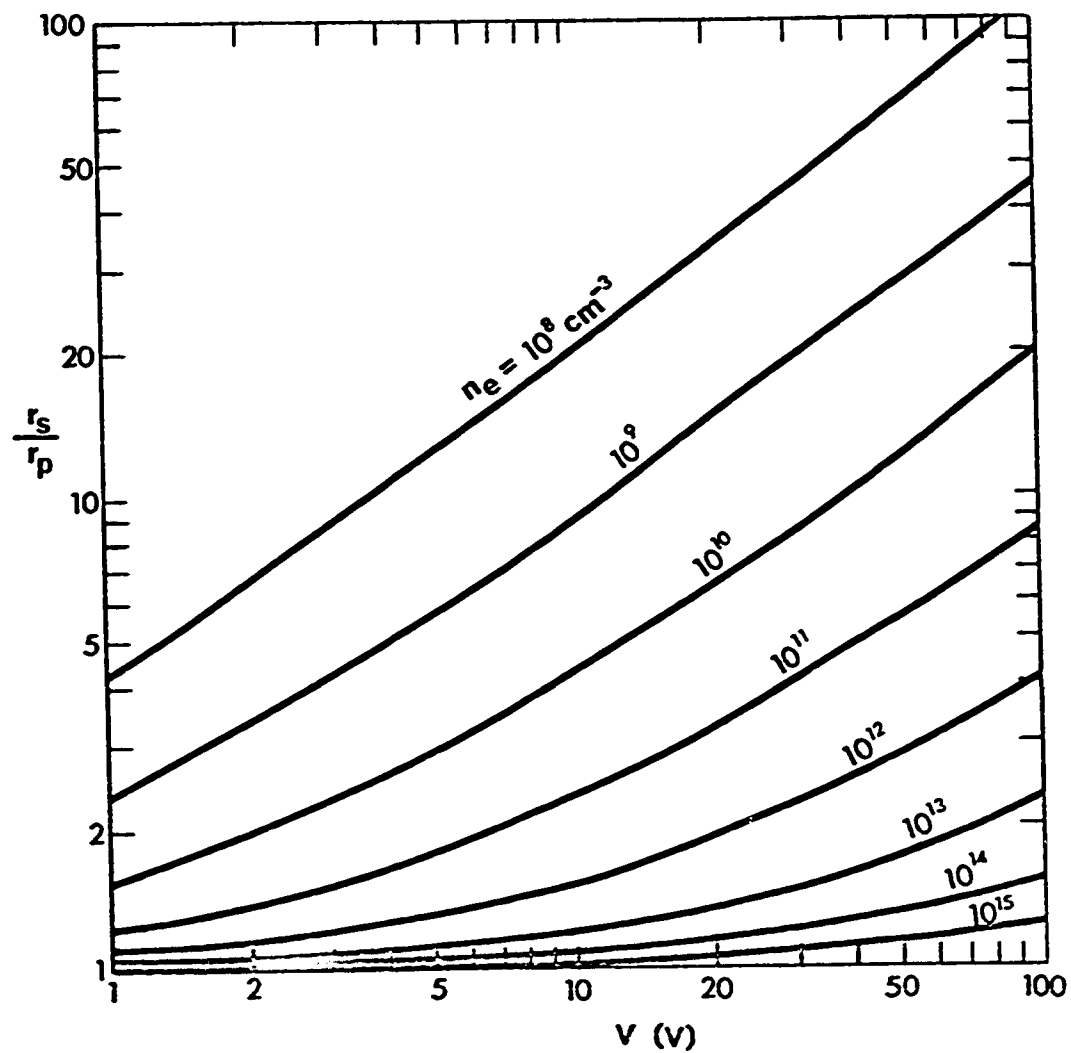
In the case of determining the ion density the situation is more complicated. In the region of the free-molecular ($r_p < \lambda_{i-n}$) to the transition ($r_p \simeq \lambda_{i-i}$) region, or more exactly, as long as $r_p \lesssim 2.5\lambda_{n-n}$, the ion current into the probe ($I_{||}$) aligned with the flow direction has the same value as in the case of a stationary plasma. With the larger probes ion collection is inhibited by the relatively small values of λ_{i-n} and λ_{i-i} (2.18), while with the probes of $r_p/\lambda_i < 3$, ion current is larger than expected (2.20).

For probes whose axis makes an angle of θ with respect to the flow, the ion current, $I_\perp$, is a function of r_p/λ_i and $u \sin\theta/v_s$, where u and v_s are the flow velocity and the ion acoustic speed ($=\sqrt{(\gamma_e kT_e + \gamma_i kT_i)/m_i}$). When the ionic mean free path is much larger than the probe radius, $I_\perp/I_{||}$ has been determined by Kanal (2.21) to be given by the expression, for cylindrical probes,

$$\Pi \equiv \frac{I_\perp}{I_{||}} = \frac{2}{\sqrt{\pi}} e^{-C^2} \sum_{n=0}^{\infty} \frac{C^n}{n!} \left[e^{V_p} V_p^{-\frac{n}{2}} \Gamma\left(\left(n+\tfrac{3}{2}\right), V_p(1+\gamma^2)\right) J_n\left(2C V_p^{\frac{1}{2}}\right) + \frac{r_s}{r_p} \frac{C^n}{n!} G\left(n+\tfrac{3}{2}, \gamma^2 V_p\right) \right] \tag{2.65}$$

$$C = \frac{u_z \sin\theta}{\sqrt{2kT_i/m_i}} = \sqrt{\frac{\gamma}{2}} M \sin\theta, \qquad \gamma^2 = \frac{r_p^2}{r_s^2 - r_p^2},$$

$$\Gamma(n,x) = \int_x^\infty e^{-t} t^{n-1} dt, \qquad\qquad G(n,x) = \int_0^x e^{-t} t^{n-1} dt. \tag{2.66}$$

If we assume negligible sheath thickness, this equation reduces to,

$$\Pi = \frac{I_\perp}{I_{||}} = \frac{2}{\sqrt{\pi}} e^{-C^2} \sum_{n=0}^{\infty} \left(\frac{C^n}{n!}\right)^2 \Gamma\left(n+\tfrac{3}{2}\right). \tag{2.67}$$

In an approximate theory $I_\perp/I_{||}$ can be found as follows:

$$I = \tfrac{1}{2} n_e ev.2\pi r_s L$$

$$I = n_e eu \sin\theta.2 r_s L$$

(2.20) S. Lederman, M.H. Bloom and H.F. Widhope: AIAA Journal 6 2133 (1968)
       W.E. Scharfman & W.C. Taylor: AIAA Journal 8 1067 (1970)
(2.21) M. Kanal: J. Appl. Phys. 35 1697 (1964)

$$\therefore \frac{I_\perp}{I_\parallel} = \frac{2}{\sqrt{\pi}} \frac{u \sin\theta}{\sqrt{2kT_i/m_i}} = \frac{2}{\sqrt{\pi}}C. \qquad (2.68)$$

This equation approximates Eq. 2.67 well if C is larger than 2. $(I_\perp/I_\parallel = 1$ at C=0.)

2.6 ION CURRENT IN A COLLISION-DOMINATED PLASMA FLOW

When an electrical Reynolds number defined by

$$R_E = \frac{uL}{D_a} = \frac{uL}{\mu_i(kT_e/e)} \qquad (2.69)$$

(L is the length typical of probe dimensions $=2r_p$ for cylindrical probe, u is the undisturbed plasma velocity relative to the probe and D_a is the ambipolar diffusion constant) exceeds unity, the probe current characteristics begin to be influenced by the flow effects of the plasma. In addition when the flow is supersonic, a shock will be formed around the probe (see Fig.5.4) and the probe current becomes dependent upon the superposed ionization and recombination processes. In such a case the chemical and dynamical effects on the probe current can be considered separately if the shock effects are not very large. In this section we are mainly concerned with the ion collection effect under the assumptions of frozen chemistry, frictional heating in the boundary layer and recombination effects. Stagnation shock effects including new ionization will be treated in Sec. 5.2.

2.6.1 Thin Sheath

A mathematical treatment for thin sheath case was done by Lam (2.22) under the assumptions that

$$\alpha = \frac{\lambda_D}{L} \ll 1, \quad \chi = \frac{eV}{kT_e} \gg 1, \quad e\lambda_i E \ll kT_e$$

and

$$R_E \alpha^2 \chi^2 \ll 1. \tag{2.70}$$

(The last condition implies that the sheath remains thin at moderate values of probe bias.) It was found that the electrical perturbations to the plasma can be divided into three physically distinct and mathematically uncoupled regions, namely the outer region, the ambipolar diffusion region and the sheath region. The probe current can be approximated as a current diffusing into the electric boundary layer (of thickness δ) formed around the probe, i.e.,

$$J_\perp = 2\pi r_p e D_a \nabla n \simeq 2\pi r_p e D_a \frac{n_e}{\delta} = \sqrt{2}\, \pi n_e \sqrt{e \mu_i r_p u k T_e}, \tag{2.71}$$

where δ is expressed as,

$$\delta = \frac{2 r_p}{\sqrt{R_E}} = \sqrt{\frac{2 r_p D_a}{u}} = \sqrt{\frac{2 r_p \mu_i k T_e}{e u}}. \tag{2.72}$$

2.6.2 Moderate Sheath

The case of $\alpha \ll 1, \chi \gg 1, R_E \alpha^2 \ll 1$ and $R_E \alpha^2 \chi^2 \gg 1$ was treated by Clements and Smy (2.23). The diffusion current in this case is negligible and also the sheath thickness, d, becomes dependent on the angle θ between the radii

---

(2.22) S.H. Lam: AIAA Journal **2** 256 (1964)
(2.23) R.M. Clements & P.R. Smy: J. Appl. Phys. **41** 3745 (1970)

to the point under consideration and the upstream edge of the cylinder (see Fig. 5.4). d can be expressed as,

$$d(\theta) = \left(\frac{9V^2 \mu_i \varepsilon_0 r_p}{4 n_e e u}\right)^{\frac{1}{4}} \frac{\left(\frac{1}{3}\cos^3\theta - \cos\theta + \frac{2}{3}\right)^{\frac{1}{4}}}{\sin\theta} \quad . \tag{2.73}$$

The ion current to the probe is,

$$J_i = 2 n_e e u (2 d \sin\theta)_{\theta \to \pi} = 4 (3\mu_i \varepsilon_0 r_p)^{\frac{1}{4}} (n_e e u)^{\frac{3}{4}} V_p^{\frac{1}{2}}. \tag{2.74}$$

2.6.3 Thick Sheath

When $\alpha \ll 1$, $\chi \gg 1$ and $R_E \alpha^2 \gg 1$, the sheath becomes much thicker than the probe radius. The current to the probe is,

$$J_\perp = 2 r_s n_e e u, \tag{2.75}$$

and so by eliminating r_s with the space charge equation the ion current becomes (2.24),

$$J_\perp = \frac{(2\pi \mu_i \varepsilon_0)^{\frac{1}{3}} (n_e e u V_p)^{\frac{2}{3}}}{\left(\ln \frac{J_\perp}{2 n_e e u r_p}\right)^{\frac{2}{3}}} \quad . \tag{2.76}$$

2.6.4 Ion Current to the Parallel Mounted Probe

When the probe surface is parallel to the flow direction, the expression for the ion current should be somewhat changed. Let us consider the thin sheath case. The problem can be reduced to that of finding the ion current into a flat plate probe of width $2\pi r_p$ and length L placed in a plasma flow with a flow direction parallel to the probe surface. The current into the sheath can be divided into two components;

(2.24) R.M. Clements & P.R. Smy: J. Appl. Phys. 40 4553 (1969)

ambipolar diffusion current (I_d) and convection current (I_c). For $R_E \alpha^2 \chi^2 \ll 1$, the diffusion current dominates the situation while for $R_E \alpha^2 \chi^2 \gg 1$ the convection component dominates the current.

The diffusion current can be expressed in the form of Eq. 2.61 as,

$$I_d = 2\pi r_p L \frac{n_e e \overline{V}}{4} \frac{\lambda_i}{\delta} = L n_e \sqrt{2\pi r_p u e k T \mu_i}. \qquad (2.77)$$

Here the quantity δ is taken as the thickness of the electrical boundary layer, because the supply of ions is large enough there;

$$\delta = \frac{2\pi r_p}{\sqrt{R_E}} = \sqrt{\frac{2\pi r_p \mu_i k T_e}{e u}} = \sqrt{\frac{\pi^2 \overline{V} \lambda_i r_p}{4u}} \qquad (2.78)$$

The sheath thickness, d, can be determined from Poisson's equation for a continuum plasma, i.e., by solving $dE/dy = j/\varepsilon_0 \mu_i E$,

$$j = \frac{9}{8} \varepsilon_0 \mu_i \frac{V_p^2}{d^3}. \qquad (2.79)$$

Therefore the convection current can be found to be,

$$I_c = 2\pi r_p d n_e e u. \qquad (2.80)$$

The rigorous solution (2.25) indicates that the convection current is $\sqrt{2}$ times larger than the above approximate result, thus,

$$I_c = 2\pi r_p \left(\frac{9}{2} \varepsilon_0 \mu_i L\right)^{\frac{1}{4}} (n_e e u)^{\frac{3}{4}} V_p^{\frac{1}{2}}. \qquad (2.81)$$

The actual current to the probe becomes,

$$I = I_d + I_c. \quad (2.26) \qquad (2.82)$$

(2.25) R.M. Clements & P.R. Smy: Private Communication (1970)
(2.26) By measuring the current into the planar probe which was aligned parallel to the plasma flow as a function of the applied voltage and also by measuring n_e and u by the methods described in Sec. 3.2, this equation was tested and proved to be correct for the plasma density range of 10^{10}-10^{16} cm^{-3}.

2.7 FLOATING DOUBLE PROBE THEORY IN A GENERALIZED CASE

2.7.1 Potential Difference Across the Sheath

When an electrode is immersed in a plasma, a sheath is formed around it. When the potential across the sheath and the size of the sheath reach certain critical values, an electrical breakdown in the sheath occurs which is the subject of this thesis. Two electrodes of approximately the same geometry were used for this purpose. These were connected to each other by a variable voltage source, which was completely electrically isolated from any other systems, e.g., shock driver capacitor bank system, oscilloscope system. For this reason the electrodes could be regarded as floating double probes first proposed by Johnson and Malter (2.27) (thus we refer to out electrodes as probes hereafter), except that in our case the distance between the two probes was sometimes very large.

Let us find the probe current and the potentials of the two probes with respect to the plasma. Put S, V_p, j_i and j_e as the sheath area, probe potential, ion and electron saturation current densities, and T_i, T_e and V_f as the ion and electron temperatures and plasma potential outside the sheath, respectively. Suffixes 1 and 2 refer to the first (negative) and the second (positive) probes. $V_c = V_{f1} - V_{f2}$ is the spatial potential difference of the plasma at both sheaths and $V_d = V_{p2} - V_{p1}$ (> 0) is the applied voltage across the probes. The potential difference across each probe sheath is described by $V = V_f - V_p$. For simplicity we put $\phi = e/kT_e$, $\varphi = e/kT_i$ and $\Sigma I_i = S_1 j_{i1} + S_2 j_{i2}$. Usually $V_d > |V_c|$ as V_c is the order of 5 volts.

(2.27)   E.O. Johnson and L. Malter: Phys. Rev. 80 58 (1950)

Four different cases have to be considered depending on the amount of electron saturation current to the positive probe, $S_2 j_{e2}$.

(1) $S_2 j_{e2} \geq \Sigma I_i - S_1 j_{e1} \exp(-\phi_1(V_d - V_c)) \simeq \Sigma I_i$:   The potential diagram near the probes is shown in Fig. 2.4-A. We have the following basic equations:

$$V_1 + V_c = V_2 + V_d \tag{2.83}$$

$$I_p = S_1 j_{i1} - S_1 j_{e1} e^{-\phi_1 V_1} \tag{2.84}$$

$$-I_p = S_2 j_{i2} - S_2 j_{e2} e^{-\phi_2 V_2}. \tag{2.85}$$

From these equations we obtain,

$$\frac{S_1 j_{e1}}{S_1 j_{i1} - I_p} = \left(\frac{S_2 j_{e2}}{S_2 j_{i2} + I_p}\right)^{\frac{\phi_1}{\phi_2}} e^{\phi_1(V_d - V_c)}. \tag{2.86}$$

This gives us the relation between I_p and V_p. When V_d is large enough to satisfy $\exp(\phi_1(V_d - V_c)) \gg j_{i2} j_{e1}/j_{i1} j_{e2}$ and $\exp(\phi_1(V_d - V_c)) \gg S_1 j_{e1}/S_2 j_{e2}$, I_p saturates and becomes independent of V_d explicitly (I_p is dependent on S_1 which may be dependent on V_d), i.e.,

$$I_p = S_1 j_{i1} \tag{2.87}$$

$$V_1 = V_d - V_c + \frac{1}{\phi_1} \ln \frac{S_2 j_{e2}}{\Sigma I_i} \tag{2.88}$$

$$V_2 = \frac{1}{\phi_1} \ln \frac{S_2 j_{e2}}{\Sigma I_i}. \tag{2.89}$$

(2) $S_1 j_{i1} < S_2 j_{e2} < \Sigma I_i - S_1 j_{e1} \exp(-\phi_1(V_d - V_c)) \simeq \Sigma I_i$:   The potential diagram in this case is whosn in Fig. 2.4-B and the basic equations are,

$$V_2 = V_1 - V_d + V_c \quad (< 0) \tag{2.90}$$

$$I_p = S_1 j_{i1} - S_1 j_{e1} e^{-\phi_1 V_1} \tag{2.91}$$

$$-I_p = S_2 j_{i2} e^{-\phi_2 V_2} - S_2 j_{e2}, \tag{2.92}$$

which lead to,

$$\frac{S_1 j_{e1}}{S_1 j_{i1} - I_p} = \left(\frac{S_2 j_{e2} - I_p}{S_2 j_{i2}}\right)^{\frac{\phi_1}{\phi_2}} e^{\phi_1(V_d - V_c)}. \tag{2.93}$$

This gives the relation between I_p and V_d. When V_d is large enough to

satisfy

$$e^{\phi_1(V_d - V_c)} \gg \frac{4 S_1 S_2 j_{i2} j_{e1}}{(S_1 j_{i1} - S_2 j_{e2})^2} \quad , \tag{2.94}$$

I_p reaches the saturation region and then

$$I_p = S_1 j_{i1} \tag{2.95}$$

$$V_1 = V_d - V_c - \frac{1}{\varphi_2} \ln \frac{S_2 j_{i2}}{S_2 j_{e2} - S_1 j_{i1}} \tag{2.96}$$

$$V_2 = -\frac{1}{\varphi_2} \ln \frac{S_2 j_{i2}}{S_2 j_{e2} - S_1 j_{i1}} \quad . \tag{2.97}$$

(3) $S_2 j_{e2} = S_1 j_{i1}$: Equation 2.93 gives the relation of I_p vs V_d. When V_d is sufficiently large as shown in Eq. 2.94, then,

$$I_p = S_1 j_{i1} \tag{2.98}$$

$$V_1 = \frac{\varphi_2}{\phi_1 + \varphi_2}(V_d - V_c) + \frac{1}{\phi_1 + \varphi_2} \ln \frac{S_1 j_{e1}}{S_2 j_{i2}} \tag{2.99}$$

$$V_2 = -\frac{\varphi_2}{\phi_1 + \varphi_2}(V_d - V_c) + \frac{1}{\phi_1 + \varphi_2} \ln \frac{S_1 j_{e1}}{S_2 j_{i2}} \quad . \tag{2.100}$$

(4) $S_2 j_{e2} < S_1 j_{i1}$: Equation 2.93 gives the relation of I_p vs V_d. When V_d is sufficiently large as shown in Eq. 2.94, then,

$$I_p = S_2 j_{e2} \tag{2.101}$$

$$V_1 = \frac{1}{\phi_1} \ln \frac{S_1 j_{e1}}{S_1 j_{i1} - S_2 j_{e2}} \tag{2.102}$$

$$V_2 = -V_d + V_c + \frac{1}{\phi_1} \ln \frac{S_1 j_{e1}}{S_1 j_{i1} - S_2 j_{e2}} \quad . \tag{2.103}$$

In addition, if $S_2 j_{e2} \ll S_1 j_{i1}$, V_1 can be simplified as,

$$V_1 \simeq \frac{1}{\phi_1} \ln \frac{j_{e1}}{j_{i1}} \quad . \tag{2.104}$$

The variation of V_1 and $-V_2$ for all the cases is shown in Fig. 2.5 as a function of $S_2 j_{e2}$. When V_d becomes large, the differencebetween

FIG. 2.4   Potential diagram near floating double probes. The

dashed and solid lines indicate the plasma potential (V_f) and probe

potential (V_p).

FIG. 2.4-A
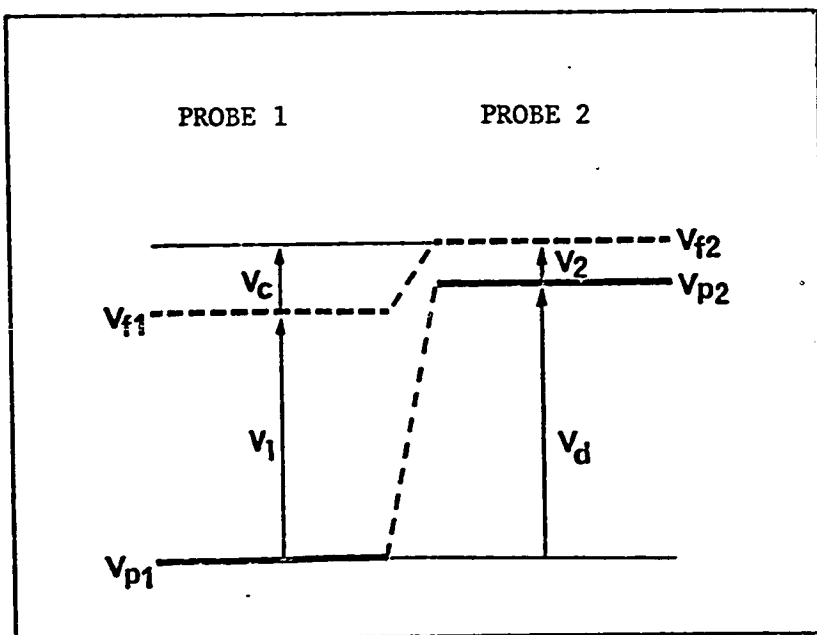
FIG. 2.4-B
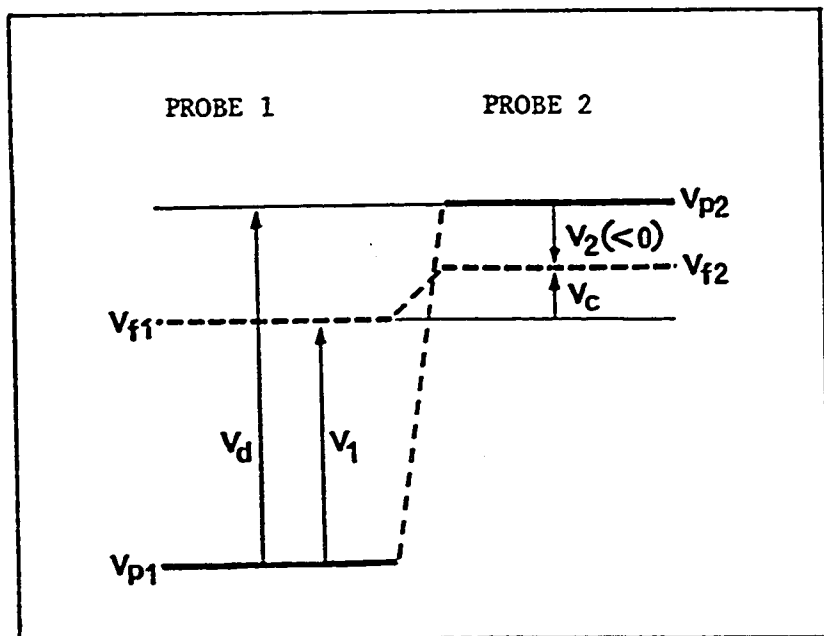
FIG. 2.5   Variation of potential difference across the sheaths of floating double probes, V_1 and $-V_2$, as a function of electron saturation current to the positive probe, $S_2 Je2$.

$I = S_2 je2$ when V_d large

$I = S_1 j_{i1}$ when V_d large

$V = V_d - V_c + \frac{1}{\phi_1} \ln \frac{S_2 je2}{\sum I_i}$

$V = -\frac{1}{\phi_1} \ln \frac{S_2 je2}{\sum I_i}$

$V = V_d - V_c - \frac{1}{\phi_1} \ln \frac{je1}{j_{i1}}$

$V = \frac{1}{\phi_1} \ln \frac{je1}{j_{i1}}$

$S_2 je2 = \sum I_i - S_1 je1 e^{-\phi_1 (V_d - V_c)}$

$S_2 je2 = S_1 j_{i1} - S_1 je1 e^{-\frac{\phi_1}{2}(V_d - V_c)}$

$\sum I_i$

$S_1 j_{i1}$

$-V_2$

V_1

$-V_2$

V_1

$S_2 Je2$

I   II   III   IV

$V_d - V_c$

$\frac{\phi_2}{\phi_1 + \phi_2}(V_d - V_c)$

0

V
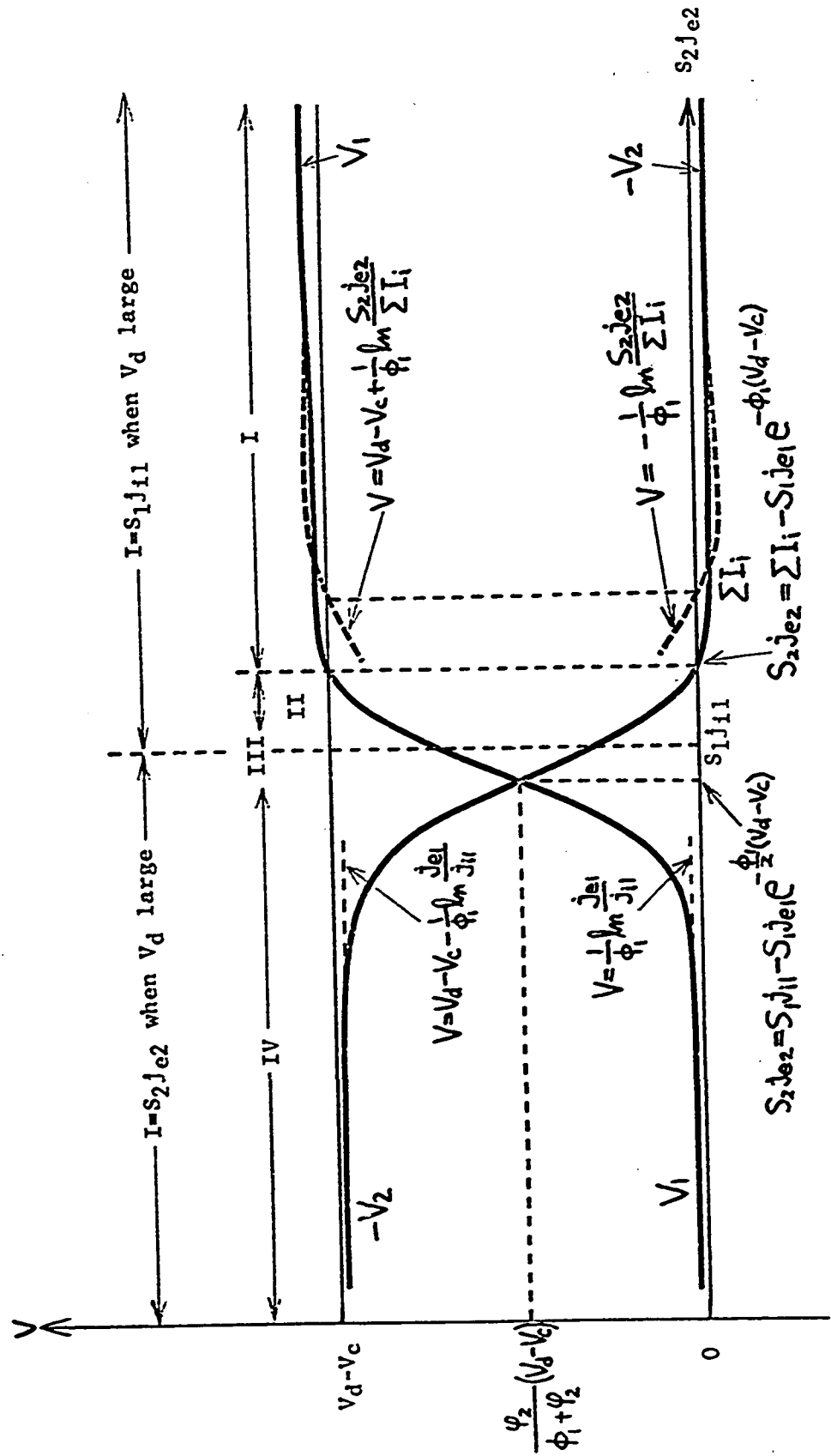
ΣI_i and $S_1 j_{i1} - S_1 j_{el} \exp(-\phi_1(V_d - V_c)/2)$ becomes extremely small and so V_1 can be approximated by,

$$V_1 = \frac{1}{\phi_1} \ln \frac{j_{el}}{j_{i1}} \tag{2.105}$$

$$V_1 = V_d - V_c + \frac{1}{\phi_1} \ln \frac{j_{el}}{j_{i1}} . \tag{2.106}$$

The calculations carried out above apply only to the case where the collisional effects of ions and electrons with neutral particles can be neglected in the sheath. However, even though the ions (only ions) are collision dominated in the sheath, Eq. 2.106 can be proved to be still valid.

2.7.2 Analysis of Axially Positioned Double Probe Current

One of the interesting applications of the double probe is to put two probes at different axial positions in the shock tube, z_1 and z_2 with distance between probes d. Two kinds of plasmas (precursor and shock heated plasma (6.5-)) are created in the tube and so ion and electron saturation current densities at each probe look like Fig. 2.6. According to the theory in the previous section, the probe current is equal to the ion or electron current at the negative probe whichever is smaller (when V_d is sufficiently large) and so the probe current can be observed as shown by the thicker lines in Fig. 2.6. Line A refers to P_1 negative, and line B refers to P_2 negative.

This type of double probe can measure a very low plasma density (such as precursor plasma) without using a large, plasma disturbing probe (10^7 cm^{-3} can be measured without difficulty). The other application of this probe is to measure plasma velocity very accurately.

FIG. 2.6   The axially positioned probe current. Ion and electron saturation currents at probes 1 (suffix 1) and 2 (suffix 2) change as shown by the thin lines, and the measured probe current changes as shown by the thicker lines. Curve A is when Probe 1 is negative and curve B is when probe 2 is negative.
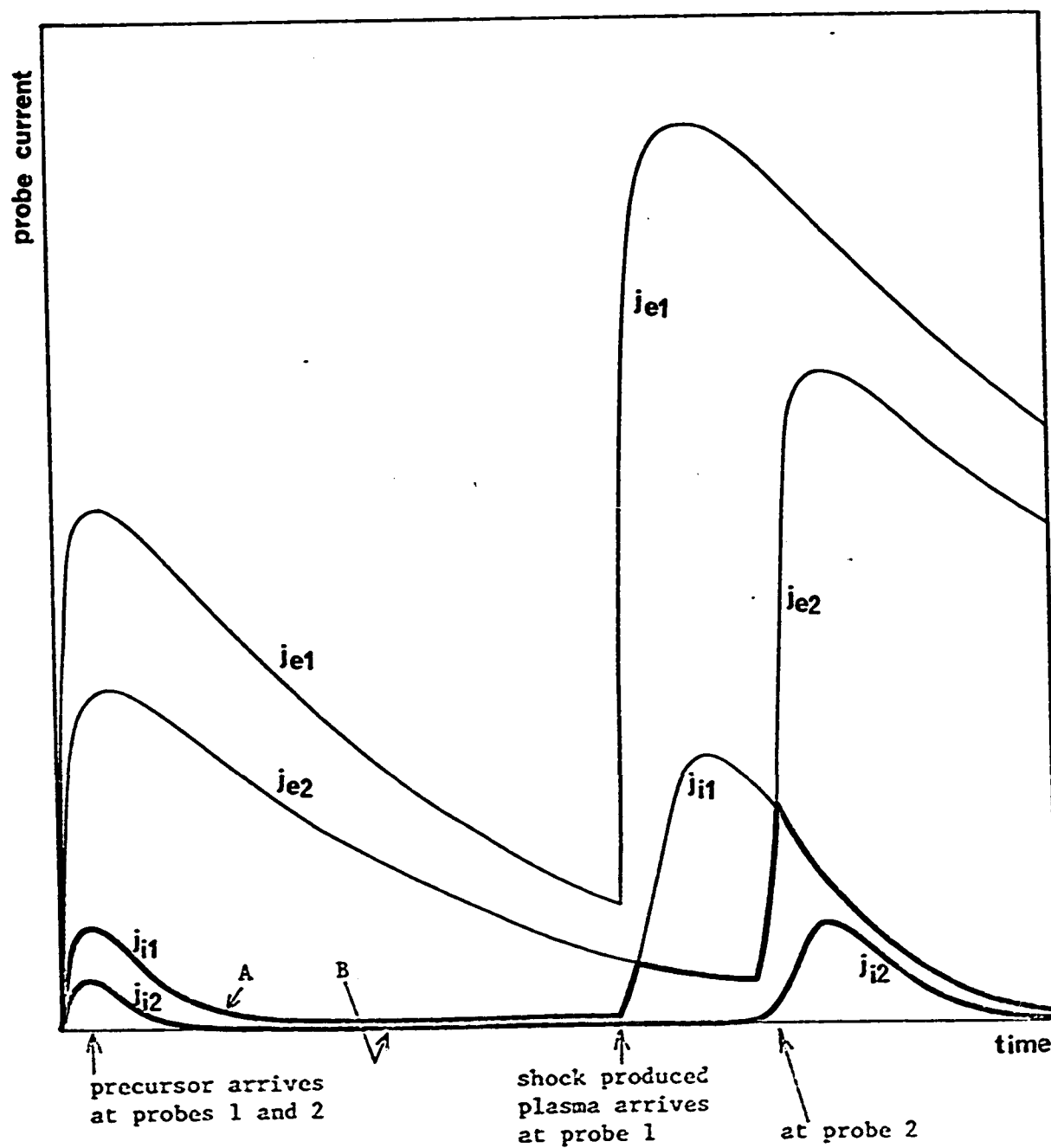
CHAPTER III   EXPERIMENTAL APPARATUS AND DIAGNOSTIC TECHNIQUES

3.1   EXPERIMENTAL APPARATUS

3.1.1   Shock Driver and Shock Tube

The shock was created by an electro-magnetic driver which propels the ionized gas by the jxB force and the thermal expansion of the arc heated gas. The driver used in this experiment consisted of the discharge chamber shown in Fig. 3.1. The stainless steel center electrode was a button type and had a diameter of 1" and a curvature of 3/4". According to Fitch and McCormick (3.1) the volumetricloss of electrodes in high current discharge switches is smallest for stainless steel, with copper the second. They also found that copper showed least profile distortion and least surface roughening. For these reasons together with the fact that they are put in a high vacuum, the electrode materials were selected as in the figure.

This type of driver was studied by Pert (3.2). He found that the pinched gas column in the center operates as a conventional metallic central conductor for the coaxial gun during the first 1.5 μs, after which the plasma slug was not accelerated by the current, since the discharge became unstable and the head of the pinched column could be seen to break away from the outgoing plasma slug.

The shock tube was made of 8 foot long (changeable), 2" inner diameter Pyrex glass tubes. At the far downstream end the vacuum pumps were connected through an expansion chamber.

(3.1)   R.A. Fitch & N.R. McCormick: Proc. I.E.E. 106A 117 (1959)
(3.2)   G.J. Pert: Canadian J. Phys. 46 2055 (1968)
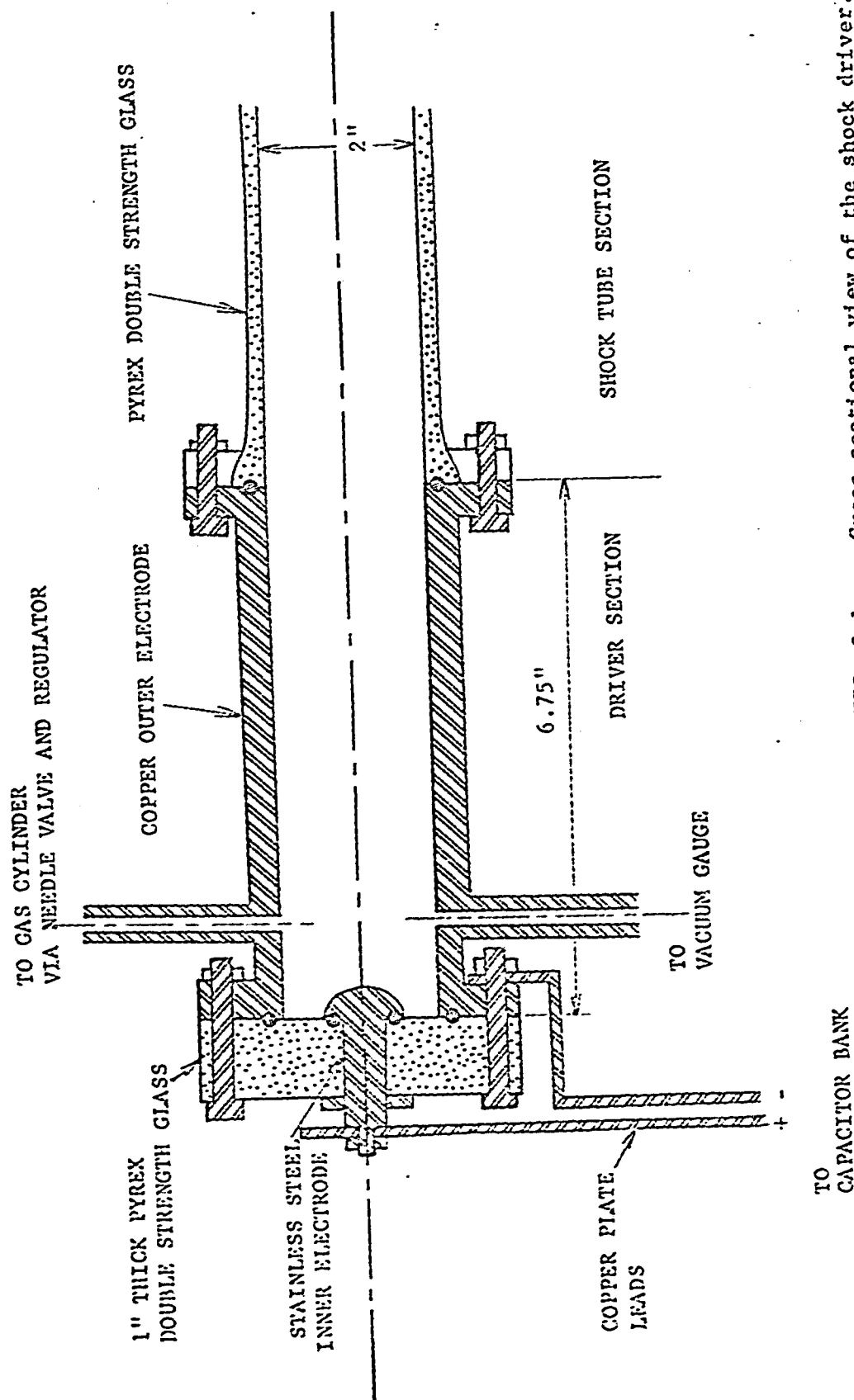
FIG. 3.1   Cross sectional view of the shock driver.
(All sizes are reduced to ½.)

3.1.2 Gas Input and the Vacuum System

The gas used throughout the experiments was argon and was obtained from Canadian Liquid Air, who give the following impurity content (%):

Ar	N_2	O_2	H_2	H_2O
99.995	0.0033	0.0005	0.0002	0.0001

The vacuum system consisted of a backing pump, Zeolite sorption trap, buffer, mercury vapor diffusion pump (Edwards High Vacuum Ltd. Model EM2), water cooled baffle (CB02), liquid nitrogen cooled vapor trap (NTM2) and butterfly valve (QSB2), with a gross pumping speed of 25 liters/sec.

The following vacuum gauges were employed; a hot cathode ionization gauge (10^{-9}-10^{-3} mmHg), Pirani gauges (one 0.0001-0.1 mmHg and two 0.01-10 mmHg for shock tube and backing system), Vacustat mercury gauges (0.001-1 mmHg and 0.01-10 mmHg) and McLeod gauge for the calibration of all these gauges.

A base pressure of 2×10^{-6} mmHg was obtained with this system. Just before taking the measurements the pump was isolated and argon gas was admitted through the needle valve to bring the system to the desired pressure. After each firing the entire shock tube was cleaned to 2×10^{-6} mmHg.

3.1.3 Power Supply

Figure 3.2 shows the block diagram of the apparatus used in this thesis. The circuit parameters of the assembled bank discharge circuit
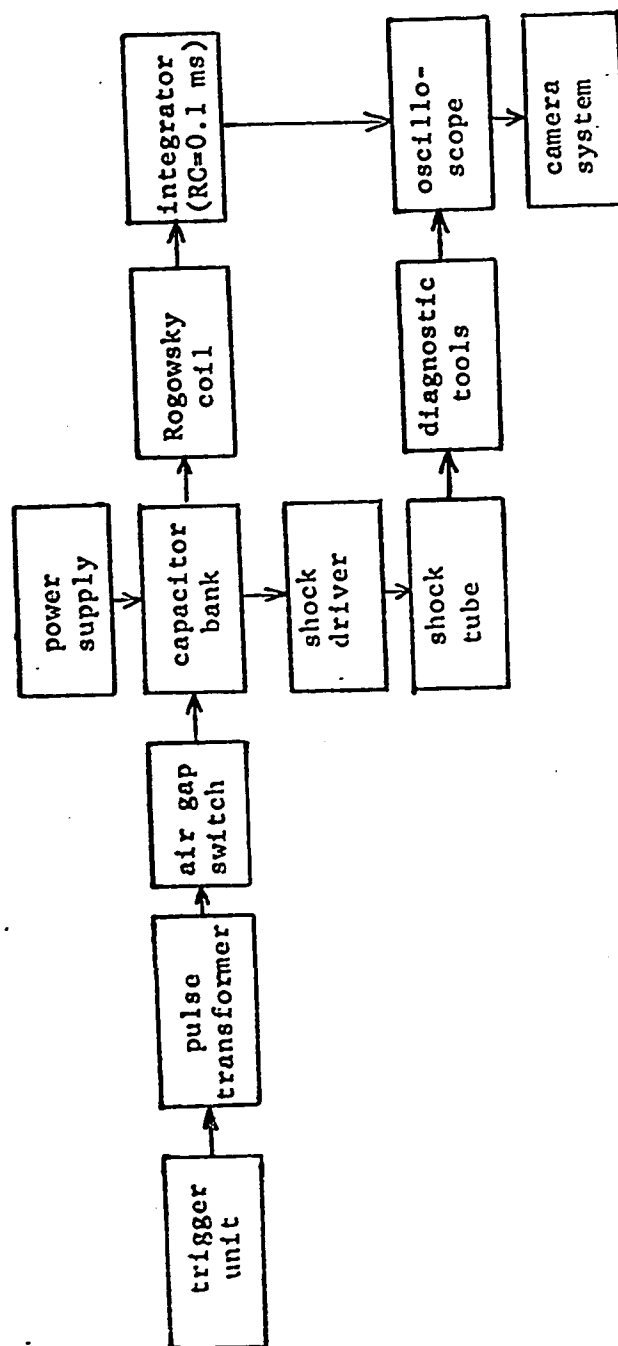
FIG. 3.2   Block diagram of the power supply and diagnostic system

were:

Bank capacitance	240 μF
Discharge circuit inductance	0.13 μH
Discharge circuit resistance	10.4 mΩ
Maximum bank operating voltage	5 KV
Maximum bank energy	3 KJ
Ringing frequency	25 KHz.

3.2 DIAGNOSTIC TECHNIQUES

3.2.1 Pressure Probe

The Piezo electric pressure probe was flush mounted to the shock tube wall for the measurements of shock heated gas pressure. The probe used was type LD-25 (Atlantic Research Co.) with a sensitivity of 0.15 V/psi (=0.717 mmHg/V) and the rise time of 1 μs. The sensitivity was calibrated by using another shock tube (3.3).

(3.3) The shock tube used for the calibration was an electromagnetically driven shock tube with diaphragm separating the driver and the test sections. This type of shock tube was introduced by P.R. Smy: Nature 193 969 (1962), Rev. Sci. Instr. 36 1334 (1965) and studied extensively by M.G.R. Phillips: Ph.D. Thesis, Univ. of British Columbia, Canada (1969) with the conclusion that this type of shock tube behaves in a manner similar to cold gas-driver diaphragm shock tubes, in which the Rankine-Hugoniot relations are valid.

3.2.2 Plasma Density Measurements by Electrostatic Probes

For the measurements of plasma density the floating double probe method (2.27) provides the most powerful tool in our experimental conditions and plasma density region. The theory for this probe is mentioned in Sec. 2.7, especially in Eq. 2.86. Since we are not interested in measuring the electron temperature (see Sec. 3.2.4), the probe was used only under ion saturation conditions. The probe current in this region has been treated in Secs. 2.3-2.6.

The probes used were mostly hair pin type tungsten probes which can be heated and cleaned before each run (see Sec.5.3.7). These probes had a diameter of 0.1 mm and a length of 4 cm. Many other types of probes of the same kind were made, e.g., thicker probes, shorter probes and probes which could be placed parallel with the plasma flow direction.

For the measurements of electrical breakdown phenomena the same type of probes were used, except that they had much longer tungsten wires and their holders had long sleeves. By doing this the contaminated part (about 1 mm long which cannot be heated enough) of the tungsten wire adjacent to the probe holder was well removed from the plasma and did not affect the measurement of the breakdown voltage. Figure 3.3 shows the general view of the electrode system.

The probe/electrode power supply consisted of D.C. batteries paralleled with fast capacitors mostly of capacitance equal to $4\mu F$. (A capacitor of up to $240\mu F$ was tested and it was found that as long as the capacitance was large enough, there was no change in the measured probe/electrode currents. However, when the capacitance was too large, the electrode was destroyed at each breakdown due to the intense heat of

FIG. 3.3   Cross sectional view of hair pin type electrode (real size).

Plasma flows perpendicular to the paper surface.
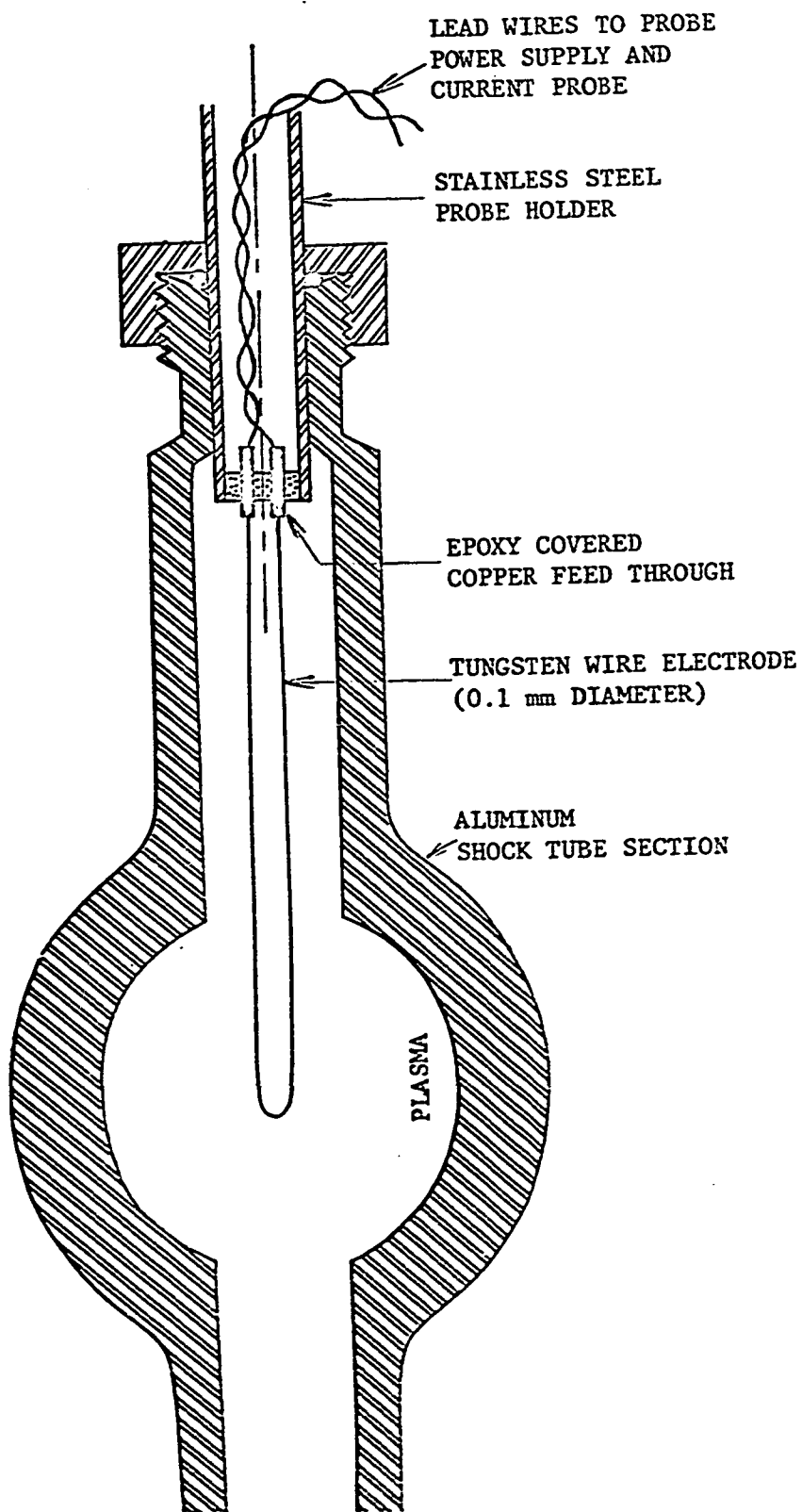
the arc spots.) The output impedance of the power supply was 0.2Ω.

The probe/electrode currents were measured by an A.C. current probe (Sec. 3.2.8).

3.2.3 Plasma Density Measurements by Microwave Cavity

The resonant cavity method of measuring plasma density is a very sensitive technique because it utilizes the high value of Q of the cavity. This technique is useful at densities up to about 10^{11} cm^{-3}, before the plasma frequency becomes so high that the necessary cavity dimensions become restrictively small.

When a low loss dielectric of permittivity ϵ is inserted in a microwave cavity, the resonant frequency shifts. From the perturbation theory the shift of the resonant frequency, Δf_d, from the resonant frequency, f_0, is expressed as (3.4),

$$\frac{\Delta f_d}{f_0} = \frac{1}{2} \frac{\int (1-\frac{\epsilon}{\epsilon_0}) E^2 d\tau}{\int E^2 d\tau} \, , \qquad (3.1)$$

where ϵ_0 is the permittivity of the vacuum and $\int d\tau$ is the volume of the cavity. If ϵ does not depend on position, the numerator of the right hand side of Eq. 3.1 can be rewritten as, $(1-\epsilon/\epsilon_0)\int E^2 d\tau'$, where $\int d\tau'$ is the volume of the dielectric in the cavity. The permittivity of the plasma is expressed as, with the notations that

$$\Upsilon = \frac{\nu_m}{\omega} \quad \text{and} \quad \eta = \frac{\omega_p^2}{\omega^2} = \frac{ne^2}{\epsilon_0 m \omega^2} \, , \qquad (3.2)$$

$$\epsilon = \epsilon_0 + \frac{\sigma}{j\omega} = \epsilon_0 + \frac{ne^2}{j\omega m} \frac{\nu_m - j\omega}{\omega^2 + \nu_m^2} = \epsilon_0 \left(1 - \eta \frac{1+j\Upsilon}{1+\Upsilon^2}\right) \simeq \epsilon_0 (1-\eta) \, , \quad (3.3)$$

(3.4) S.J. Buchsbaum & S.C. Brown: Phys. Rev. 106 196 (1957)
       S.C. Brown: Proc. 2nd Int'l Conf. Peaceful Use of Atomic Energy
       32 394 (1958)

since, the plasma under measurement is usually of low density, low collision plasma frequency and therefore $\nu_m \ll \omega$. If a plasma of the same shape as the dielectric is replaced in the cavity, then the resonant frequency shift, Δf, is expressed as,

$$\frac{\Delta f}{f_0} = \frac{\eta}{2} \frac{\int E^2 d\tau'}{\int E^2 d\tau} . \qquad (3.4)$$

Here, in order to use the perturbation theory, ω_p^2 must be much smaller than ω^2.

Having considered the actual plasma geometry (2" diameter, infinite length), interfering modes, cavity size, etc., a cylindrical cavity of radius R=4" and length 4.25" surrounding the shock tube (of radius a) was built (3.5). Further, the TM_{020} mode was found to be adequate for the measurements. For this mode the electric field and resonant frequency are,

$$E_z = AJ_0(kz), \quad E_x = E = 0 \qquad (3.5)$$

and $$f_0 = \frac{ck}{2\pi} = 2.59 \text{ GHz} \quad (S\text{-band}), \qquad (3.6)$$

where c is the speed of light, $k = S_{02}/R$ and $S_{02} = 5.520$ is the second zero of $J_0(x)$. Integrals of Eq. 3.4 then become,

$$\frac{\int E^2 d\tau'}{\int E^2 d\tau} = \frac{a^2}{R^2} \frac{J_0^2(ka) + J_1^2(ka)}{J_1^2(kR)} \approx 0.337 . \qquad (3.7)$$

Since an actual resonant cavity has two end holes for the shock tube to pass through, Eq. 3.7 is not exact. To minimize the consequent error two improvements were made. One of them was to attach conducting sleeves which tightly surrounded the plasma container on the outside of both holes on the cavity. These conducting sleeves were designed to be circular waveguides whose cut off frequency was beyond the resonant frequency of

(3.5) E.L. Ginzton: "Microwave Measurements" McGraw-Hill Co. pp357 (1957)

the cavity so that no radiation could escape and hence the cavity appeared to act as if it had solid end plates (3.6). These sleeves should be a few attenuation distances long. The 2.375" diameter 4" long sleeves were attached on both sides of the cavity. The sleeves had a minimum cut off frequency of 2.93 GHz. The resonant frequency of this assembled cavity was 2407.5 MHz.

The second improvement was to calibrate the cavity by using a 2" diameter and sufficiently long dielectric rod instead of plasma and so eliminate the integrals of Eq. 3.4. The following equations were used for determining the plasma density,

$$\Delta f = \frac{1}{1-\frac{\epsilon}{\epsilon_0}} \Delta f_d \tag{3.8}$$

or

$$n = \frac{m\epsilon_0\left(1-\frac{\epsilon}{\epsilon_0}\right)\omega_0^2}{e^2}\frac{\Delta f}{\Delta f_d} = 0.0124\left(1-\frac{\epsilon}{\epsilon_0}\right)f_0^2\frac{\Delta f}{\Delta f_d}. \tag{3.9}$$

To know the precise value of ϵ/ϵ_0, the same dielectric was coaxially mounted into a cavity with solid end plates and the shift of resonant frequency was measured. From the shift, ϵ/ϵ_0 was calculated by using Eqs. 3.1 and 3.7.

3.2.4 Electron Temperature Measurements by Single Probe Method

A floating double probe collects only a very small amount of electrons of the highest energies. In our plasma where there possibly are small amounts of high energy electrons (e.g., run away electrons, photoionized electrons) in addition to the large amount of Maxwellian

---

(3.6) R.M. Clements: Private Communication (1969)

electrons, the double probe technique is liable to produce erroneous measurements of bulk electron temperature.

The original single probe method proposed by Langmuir and Mott -Smith (3.7) collects electrons of the whole energy range, so that this method measures the T_e of the majority group. However, the single probe technique has disadvantages, some of which are now discussed:

(1) Sometimes it is difficult to have a proper reference electrode. In our shock tube, the plasmoid becomes electrically separated from the driver electrodes and so the driver electrodes do not provide a reference potential.

(2) If one uses a large enough probe as a reference, then the geometries of the reference and the electron collecting probes are very different and one has to be cautious about whether they are in a collision free or collision dominated category.

(3) If the larger probe is collision dominated (as is usual), the current to the probe is mostly determined by ambipolar diffusion; i.e., the probe potential extends over a distance which is approximately equal to the probe size. Frequently the smaller probe cannot be put outside this ambipolar diffusion region. In this ambipolar field the ion and electron densities are still equal and electrons have a Maxwellian distribution, although their density and potential are somewhat decreased.

(4) If the larger probe is in a collision dominated region, the current to the probe cannot increase infinitely as the probe area is increased. This can be proved easily. From Eq. 2.60,

$$I = S e D_a \frac{ne}{\delta},$$

(3.10)

where δ is the characteristic size and is approximately proportional to S, the probe area. Therefore I becomes independent of S and has a finite

(3.7) I. Langmuir & H.M. Mott -Smith: Gen. Elec. Rev. 27 449, 538, 616, 762, 810 (1924)

maximum value. In this case the ion collection by the larger probe is not enough and its potential decreases because of the surplus electron accumulation.

(5) The probe draws a heavy electron current from the plasma which results in a plasma perturbation.

(6) To avoid the large electron currents, the electron collecting probe must be very small. This causes the probe geometry to be far different from the ideal planar, cylindrical or spherical probe geometry.

One of the ways to avoid some of these disadvantages (1, 3 and 4) is to use a third probe (dummy probe) in addition to the electron collecting probe and reference probe. The current into the electron collecting probe (of area S_1) is expressed as,

$$I = S_1 j_e e^{-\frac{e}{kT_e}(V_f - V_d + \Delta V)} = S_1 j_e e^{-\frac{eV_f}{kT_e}} e^{\frac{e(V_d - \Delta V)}{kT_e}} , \qquad (3.11)$$

where V_f is the floating potential expressed by the equation in Sec. "List of Symbols", V_d is the potential of the electron collecting probe with respect to the reference probe and ΔV is the potential float of the reference probe. This ΔV can readily be measured by applying a voltage across the dummy and the reference probes. The voltage at which the current into the dummy probe is zero is equal to ΔV. The slope of log I vs $V_d - \Delta V$ when $V_f > V_d - \Delta V > 0$ yields the electron temperature.

In our temperature measurement experiment, the reference probe was made of copper and had an area of 230 cm^2. Two types of electron collecting probes were made of cylindrical tungsten wire and had dimensions of either 0.1 mm diameter and 5 mm long or 1 mm diameter and 5 mm long. The dummy probe was 1 mm diameter and 5 cm long copper wire.

3.2.5 Two Coil r.f. Determination of Plasma Conductivity

This section describes a new method of measuring the electrical conductivity of a plasma by utilizing the dependence of the mutual inductance of two coils upon the conductivity of the medium lying between them (3.8). In addition to its simplicity, this method has several advantages over previous single coil measurements (3.9). These are;

(1) high speed response (20 nsec),

(2) it gives a measure of the average conductivity in the plasma rather than of that very close to the coil,

(3) it can be used over a continuous and wide range of frequencies with the result that a very wide range of conductivity can be measured (to 10^6 mhos/m).

Electrostatic effects can be eliminated by the use of a third coil which avoids any necessity for electrostatic screening.

Consider a cylindrical plasma (of radius a) with surrounding field and search coils (of radius b) placed concentric with the plasma axis with a separation of z_0. The conductivity of the plasma is considered to be constant throughout, i.e.,

$$\sigma = (\text{constant}) \quad \text{when } 0 \leq r \leq a$$

$$\text{and} \quad \sigma = 0 \quad \text{when } r > a, \tag{3.12}$$

where r is the radial variable of a cylindrical coordinate system whose origin is at the center of the field coil. Let ω be the angular frequency of the magnetic field. By solving Maxwell equations the ratio of the signals induced by the search coil with and without plasma (V and V_0) is found to be (for the case of a=2.54 cm, b=3.00 cm),

$$\frac{V}{V_0} = \frac{0.195(\alpha^2-j\lambda^2)^{\frac{1}{2}}J_0[(\alpha^2-j\lambda^2)^{\frac{1}{2}}a] + 39.8 J_1[(\alpha^2-j\lambda^2)^{\frac{1}{2}}a]}{(\alpha^2-j\lambda^2)^{\frac{1}{2}}J_0[(\alpha^2-j\lambda^2)^{\frac{1}{2}}a] - 8.96 J_1[(\alpha^2-j\lambda^2)^{\frac{1}{2}}a]} \quad (3.13)$$

where $\lambda^2 = \omega\mu\sigma$, J_0 and J_1 are the Bessel functions of 0th and 1st order of the first kind, respectively. Here the magnetic field was approximated to change exponentially along the axis of the cylinder with the decay constant of α. (This is a good approximation if $z_0 > b/5$.) The variation of $|V/V_0|$ as a function of σf was solved numerically and the results shown in Fig. 2 of reference 3.8.

Measurements have been performed upon electrolytes of known conductivity and plasmas (whose conductivity was measured by Lin's method (3.10)) with conductivities from 10 to 10^4 mhos/m at frequencies from 0.1 to 50 MHz, and in every case agreement with theory was excellent.

3.2.6 Conductivity Measurements by Lin's Method

For conductivity measurements of a moving plasma, the method proposed by Lin et. al. (3.10) provides a useful tool. This method uses two coils whose axes are aligned with that of the shock tube. The downstream coil (field coil) provides an axially symmetric D.C. magnetic field, while the search coil slightly ahead of the field coil picks up the electromagnetic disturbance produced by the passage of the plasma slug through the magnetic field.

(3.8) S. Mikoshiba & P.R. Smy: Rev. Sci. Instr. 40 1187 (1969)
(3.9) R.A. Olson & E.C. Lary: Rev. Sci. Instr. 33 1350 (1962)
       E.J. Stubbe: Proc. IEEE 56 1483 (1968)
       P. Savic & G.T. Boult: J. Sci. Instr. 39 258 (1962)
       H.E. Koritz & J.C. Keck: Rev. Sci. Instr. 35 201 (1964)
       K.B. Persson: J. Appl. Phys. 32 2631 (1961)
       M. Ciampi & N. Talini: J. Appl. Phys. 38 3771 (1967)
       H. Tanaca & M. Hagi: Jap. J. Appl. Phys. 6 335, 338 (1964)
       K.V. Donskoi & I.A. Prokof'ev: Sov. Phys. Tech. Phys. 7 805 (1963)
       D.D. Hollister: AIAA Journal 2 1568 (1964)
(3.10) S.C. Lin, E.L. Resler & A. Kantrowitz: J. Appl. Phys. 26 95 (1955)

The D.C. magnetic field induced by the field coil is proportional to the current, I, through the coil. When a plasma enters the field with a velocity u, a current is induced in the plasma by its diamagnetic property. This current has only an azimuthal component, j_θ, and is proportional to $\sigma u I$, where the electrical conductivity of the plasma is considered to be constant throughout the radial direction (eq. 3.12). The total magnetic flux, Φ, due to j_θ is,

$$\Phi \propto j_\theta \propto \sigma u I, \tag{3.14}$$

therefore the voltage induced in the search coil, V, is proportional to $d\Phi/dt$, or

$$\int V dt \propto \sigma u I. \tag{3.15}$$

The proportionality constant can be eliminated by calibrating the system with a metal rod of known conductivity and velocity. Finally we obtain the equation for plasma conductivity,

$$\sigma = \frac{u_c I_c \int V dt}{u I \int V_c dt} \sigma_c , \tag{3.16}$$

where subscript c denotes the values obtained with the calibrating metal rod.

In our system the calibration was carried out by an aluminum rod of 2" diameter and 6" long, with the results that $u_c = 5.76$ m/s, $\sigma_c = 2.26 \times 10^7$ mhos/m, $I_c = 145$ A and $\int V_c dt = 1.6 \times 10^{-5}$ V.sec. The search coil signal was integrated by RC-integrator with a time constant of 120 μs. Equation 3.16 can now be rewritten as,

$$\sigma = 0.944 \times 10^9 \, V_{CRO}/u , \tag{3.17}$$

where V_{CRO} is the voltage measured by the oscilloscope. The plasma velocity was measured simultaneously by a photodiode technique.

3.2.7 Plasma Luminosity Measurements

To measure the radiant energy from the plasma, a photodiode (Hewlett-Packard Associates, Type 4205) was placed adjacent to the Pyrex shock tube perpendicular to the tube axis. The sensitivity of the photodiode was 0.75 electrons/photon at 7700 Å, the directional sensitivity was confined to within 30° (this means that the axial resolution was 3 cm) and the wavelength response was 0.4-1.1 microns.

The pictures of the shock heated gas were taken with an image converter framing camera (TRW Instruments, Model 1D) with a plug-in unit (Model 26B).

3.2.8 Oscilloscope Assemblies

The following oscilloscope assemblies were used. The numbers in the bracket show the upper 3 db down frequency in Hz. The lower frequency limit was D.C., unless otherwise listed.

Oscilloscopes: Tektronix type 555 (33M), 454 (150M), 549 (30M), 321A (23M)

Plug-in units: 1A1 (50M), CA (24M), 1A5 (50M), D (2M), G (20M), O (23M)

Probes: P6006 (33M), P6012 (33M), P6047 (150M), P6015 (50M, 40KV),

                 P6019 (120Hz-60M, A.C. current probe with passive termination)

Camera: C-12 with Polaroid films.

CHAPTER IV   PLASMA PRODUCED BY ELECTROMAGNETICALLY DRIVEN SHOCK TUBE

4.1   PROPERTIES OF THE GAS BEHIND THE SHOCK

4.1.1   Incident Shock

The relations between the properties of the gas behind the shock for a one-dimensional flow of gas are presented, taking into account the effects of ionization. In a reference frame moving with the shock front, whose velocity is U, the equation of conservation of mass is,

$$\rho_1 U = \rho_2 (U - u_2),$$
(4.1)

where the flow quantities upstream of the interaction region are designated by suffix "1", downstream quantities by suffix "2". The equation for the rate of momentum flow takes the form of,

$$P_1 + \rho_1 U^2 = P_2 + \rho_2 (U - u_2)^2.$$
(4.2)

The equation for constant energy flow takes the form of adiabatic flow,

$$H_1 + \frac{1}{2} U^2 = H_2 + \frac{1}{2} (U - u_2)^2,$$
(4.3)

where H is the specific enthalpy of unit mass of the gas, expressed as,

$$H = \frac{1+\alpha}{\gamma - 1} \frac{kT}{m} + \alpha \frac{eV_i}{m} + \frac{P}{\rho}.$$
(4.4)

Here we have neglected the excitation of electronic states of the ions and the neutral particles. The first term of Eq.4.4 represents the translational energy of the gas particles; the quantity $1+\alpha$ indicates the increase in the number of particles per unit mass by ionization. The second term indicates the energy of ionization per unit mass. Together these two terms stand for the internal energy so that the addition of the third term results in an expression for the enthalpy. With the equation of state,

$$\frac{p}{\rho} = (1+\alpha)\frac{kT}{m} ,$$
(4.5)

the expression for the specific enthalpy may be simplified to,

$$H = \frac{\gamma}{\gamma-1}\frac{p}{\rho} + \frac{\alpha e V_i}{m} .$$
(4.6)

It is customary to introduce the Mach number of the shock,

$$M_1 = \frac{U}{c_1} ,$$
(4.7)

where c_1 is the sound speed in the undisturbed gas,

$$c_1 = \sqrt{\gamma\frac{p_i}{\rho_i}} .$$
(4.8)

From Eqs. 4.1, 4.2, 4.3, 4.6, 4.7 and 4.8, we obtain,

$$\eta \equiv \frac{\rho_2}{\rho_1} = \frac{(\gamma+1)M_1^2}{1+\gamma M_1^2 - \sqrt{(M_1^2-1)^2 + \frac{2\alpha(\gamma^2-1)eV_i}{mc_i^2}M_1^2}} ,$$
(4.9)

$$y \equiv \frac{p_2}{p_1} = 1 + (1-\frac{1}{\eta})\gamma M_1^2 ,$$
(4.10)

$$\frac{T_2}{T_1} = \frac{\eta + (\eta-1)\gamma M_1^2}{(1+\alpha)\eta^2}$$
(4.11)

and
$$M \equiv \frac{u_2}{c_1} = (1-\frac{1}{\eta})M_1 .$$
(4.12)

Here, for convenience, we have normalized u_2 by c_1 and put equal to M.
M must be distinguished from M_1.

By assuming thermal equilibrium, the expression for the degree of
ionization was derived by Saha (4.1) using the method of statistical
mechanics,

$$\alpha^2 = \frac{1}{\frac{g_0}{g_e g_i}\frac{ph^3}{(2\pi m)^{3/2}(kT)^{5/2}}e^{\frac{eV_i}{kT}} + 1} ,$$
(4.13)

where g_0, g_e and g_i are statistical weights of neutral, ion and electron
and are, respectively, 1, 2 and 6 for argon. Especially for argon, with
p expressed in mmHg,

(4.1)   Saha: A Treatise on Modern Physics 1 Allahabad and Calcutta (1934)

$$\alpha^2 = \cfrac{1}{340\,\rho T^{-\frac{5}{2}}\,e^{\frac{1.82\times10^5}{T}} + 1} .$$

(4.14)

Provided that U is given, ρ_2, p_2, T_2, u_2 and α can be determined. This calculation was done with $T_1=300$ K, $M_1=0\text{-}50$, $p_1=0.1\text{-}100$ mmHg, and the results presented in Figs. 4.1~4.5. For $M_1>50$ Ar^{++} becomes significant and at $M_1=87$ approximately 90% of argon is Ar^{++}. When M_1 becomes much larger, Ar^{+++} becomes dominant, while Ar^{+} and Ar^{++} decreases(4.2).

Especially when T_2 is so small that the ionization is negligible, Eqs. 4.9-4.12 can be simplified as,

$$\eta = \frac{\rho_2}{\rho_1} = \frac{(\gamma+1)M_1^2}{(\gamma-1)M_1^2+2} \qquad \left(= \frac{4M_1^2}{M_1^2+3} \quad \text{for Ar}\right) \quad (4.15)$$

$$y = \frac{p_2}{p_1} = \frac{2\gamma M_1^2-(\gamma-1)}{\gamma+1} \qquad \left(= \frac{5M_1^2-1}{4} \quad \text{for Ar}\right) \quad (4.16)$$

$$\frac{T_2}{T_1} = \frac{(2\gamma M_1^2-(\gamma-1))((\gamma-1)M_1^2+2)}{(\gamma+1)^2 M_1^2} \qquad \left(= \frac{(5M_1^2-1)(M_1^2+3)}{16M_1^2} \quad \text{for Ar}\right) \quad (4.17)$$

$$\frac{u_2}{c_1} = \frac{2(M_1^2-1)}{(\gamma+1)M_1} \qquad \left(= \frac{3(M_1^2-1)}{4M_1} \quad \text{for Ar}\right) \quad (4.18)$$

$$M_2 = \frac{U-u_2}{c_2} = \sqrt{\frac{(\gamma-1)M_1^2+2}{2\gamma M_1^2-(\gamma-1)}} \qquad \left(= \sqrt{\frac{1+\frac{3}{M_1^2}}{5-\frac{1}{M_1^2}}} \quad \text{for Ar}\right) \quad (4.19)$$

$$\frac{u_2}{c_2} = \frac{2(M_1^2-1)}{\sqrt{((\gamma-1)M_1^2+2)(2\gamma M_1^2-(\gamma-1))}} \qquad \left(= \frac{3(1-\frac{1}{M_1^2})}{\sqrt{5(1+\frac{3}{M_1^2})(1-\frac{1}{5M_1^2})}} \quad \text{for Ar}\right) \quad (4.20)$$

$$\frac{U}{c_2} = \frac{(\gamma+1)M_1^2}{\sqrt{((\gamma-1)M_1^2+2)(2\gamma M_1^2-(\gamma-1))}} \qquad \left(= \frac{4}{\sqrt{5(1+\frac{3}{M_1^2})(1-\frac{1}{5M_1^2})}} \quad \text{for Ar}\right) . \quad (4.21)$$

For the actual gas γ changes its value when T_2 is raised to certain degree by dissociation of the molecules and by quantum effects (Sec. 2.2.1).

(4.2) W.A. Menard & T.E. Horton: NASA JPL Tech. Rept. 32-1408 (1969)
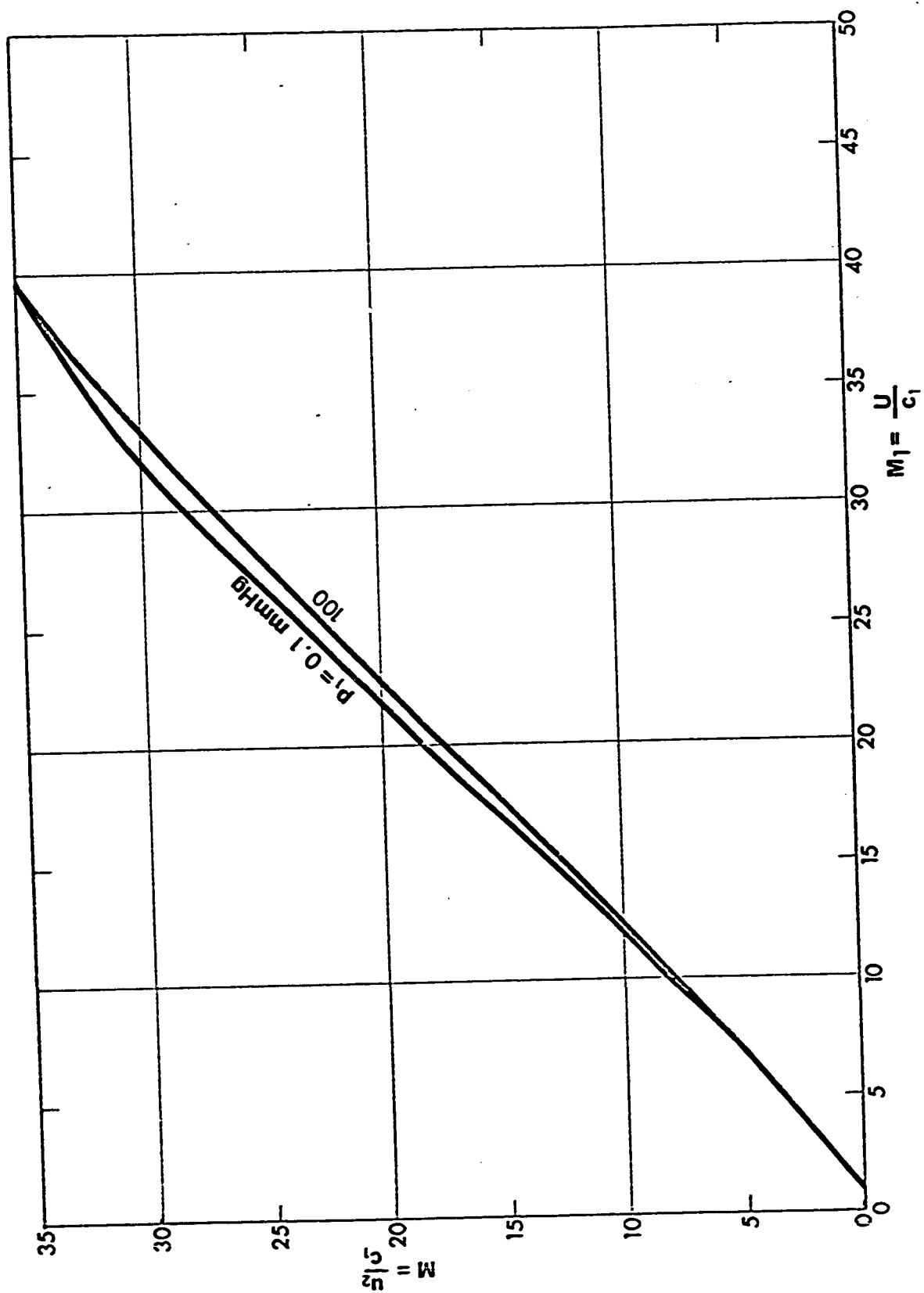
FIG. 4.1   M vs M₁ for incident argon shock.
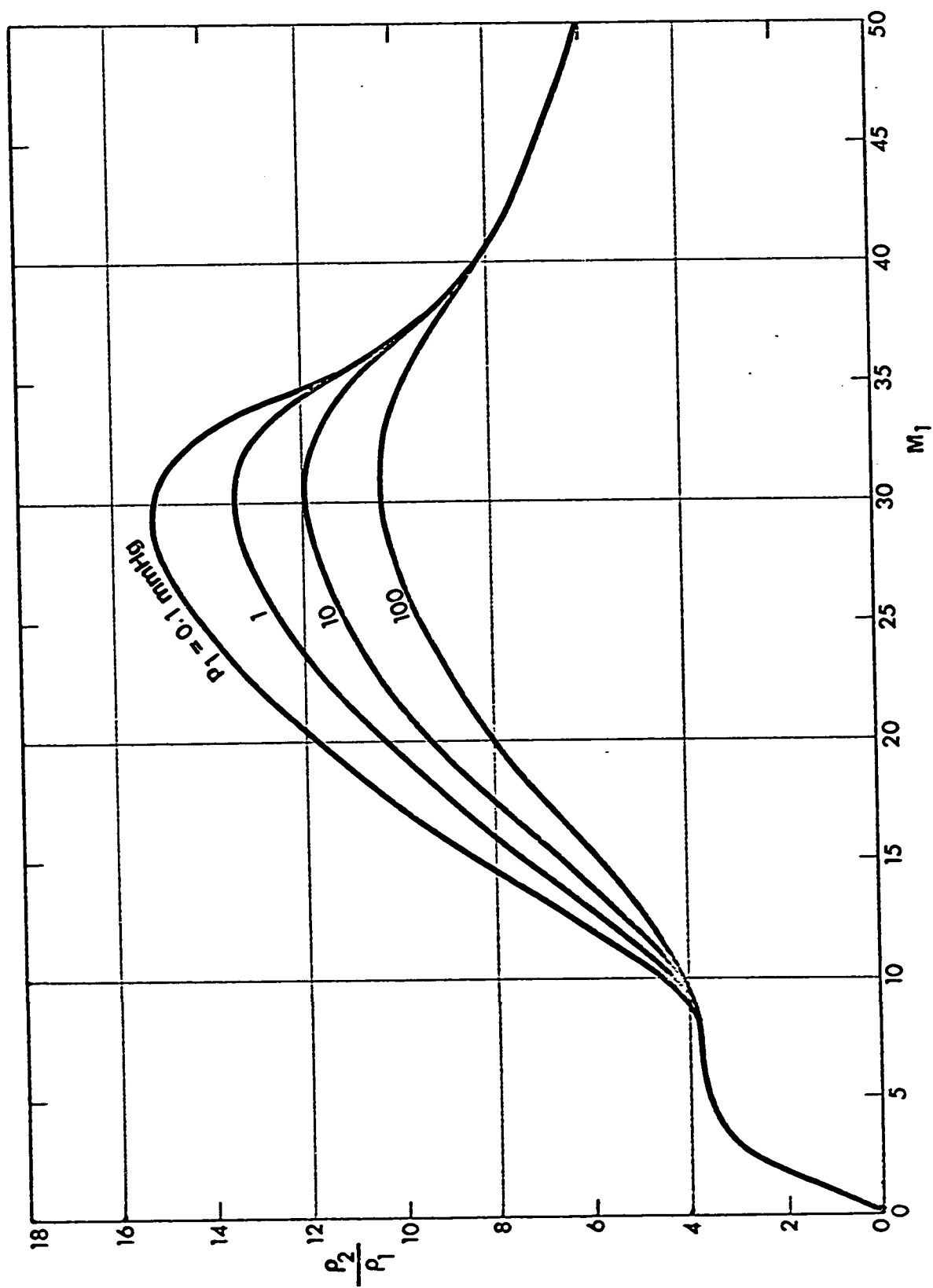
FIG. 4.2 ρ_2/ρ_1 vs M_1 for incident argon shock.
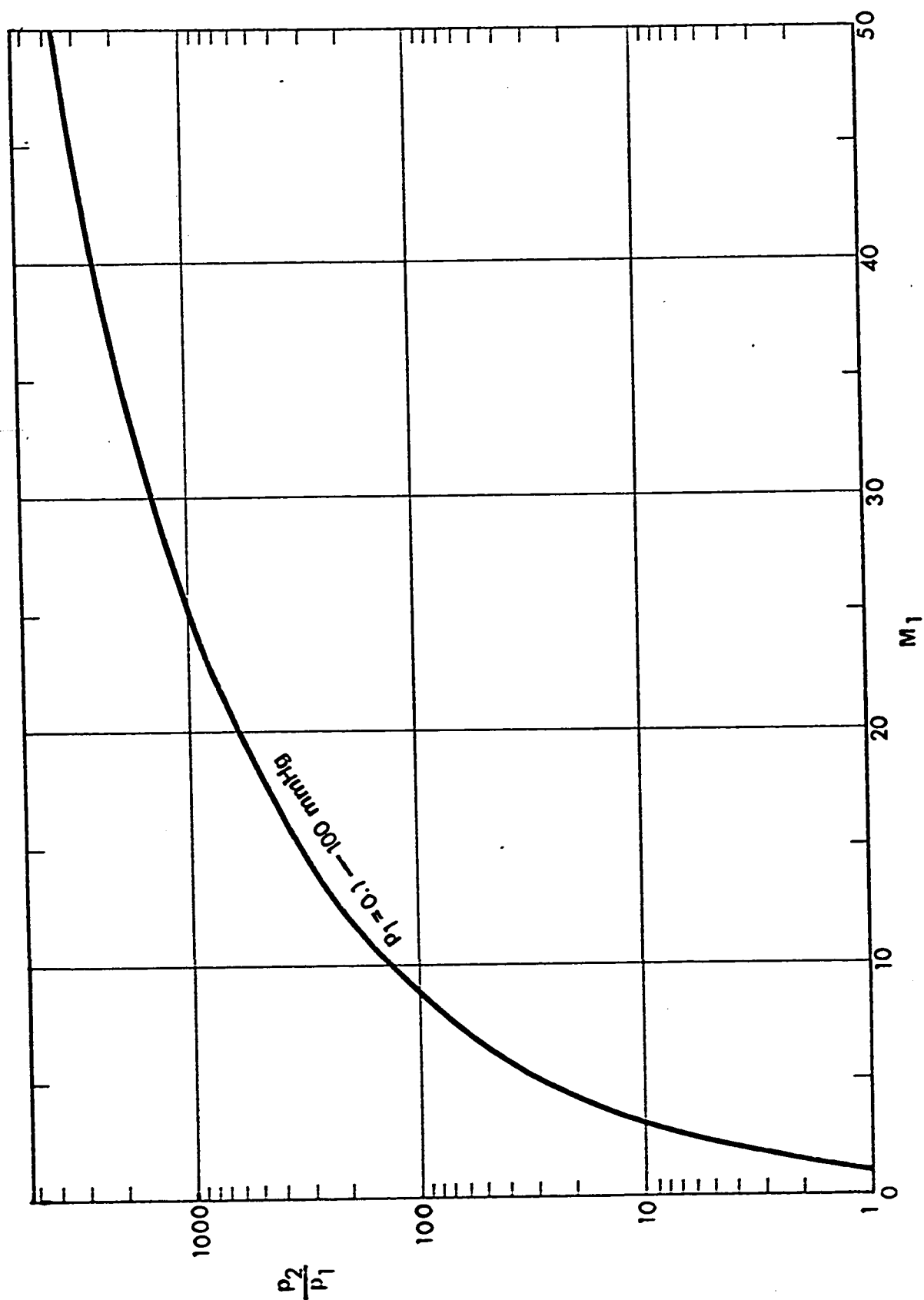
FIG. 4.3 P_2/P_1 vs M_1 for incident shock.
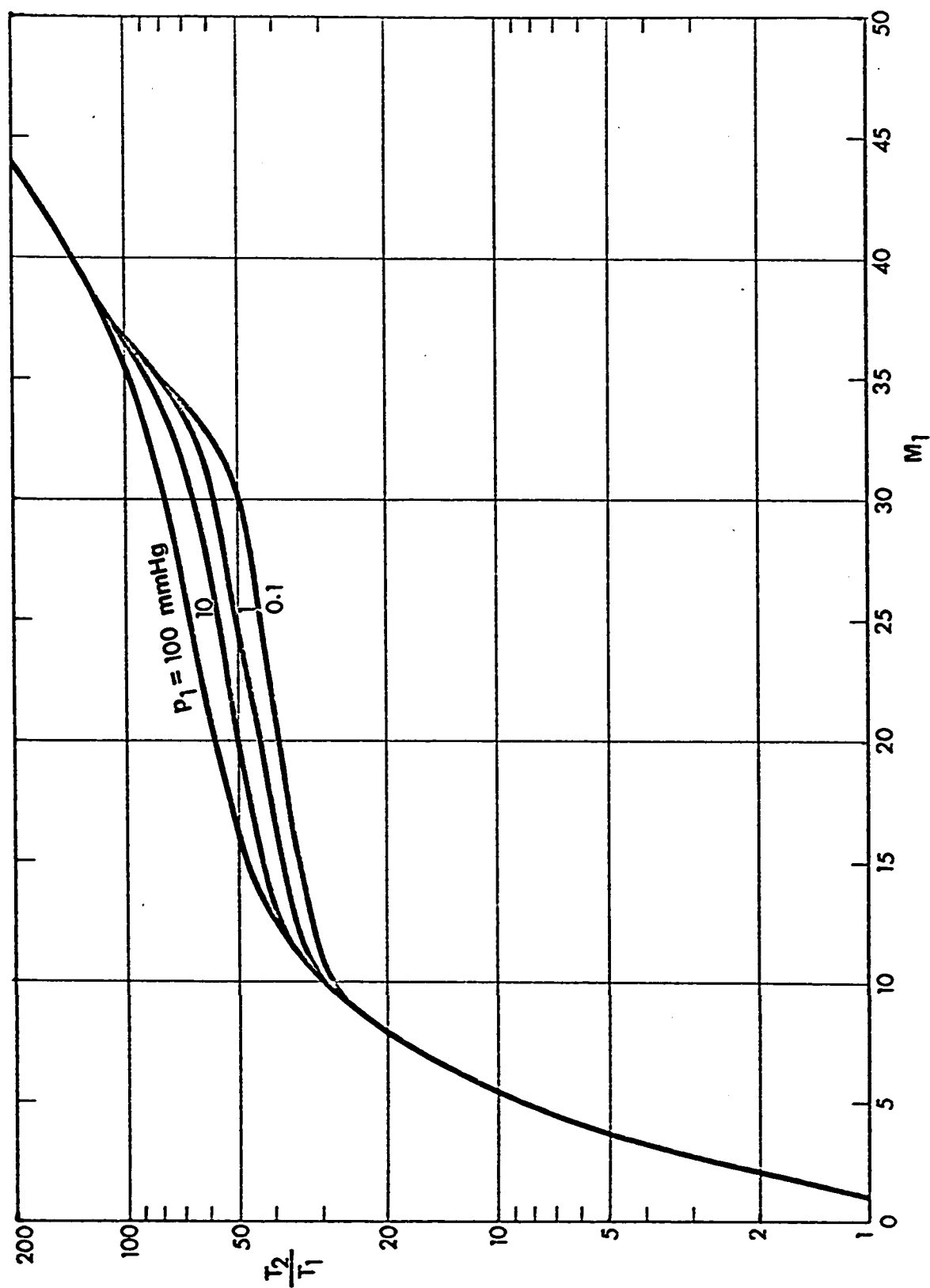
FIG. 4.4 T_2/T_1 vs M_1 for incident argon shock.
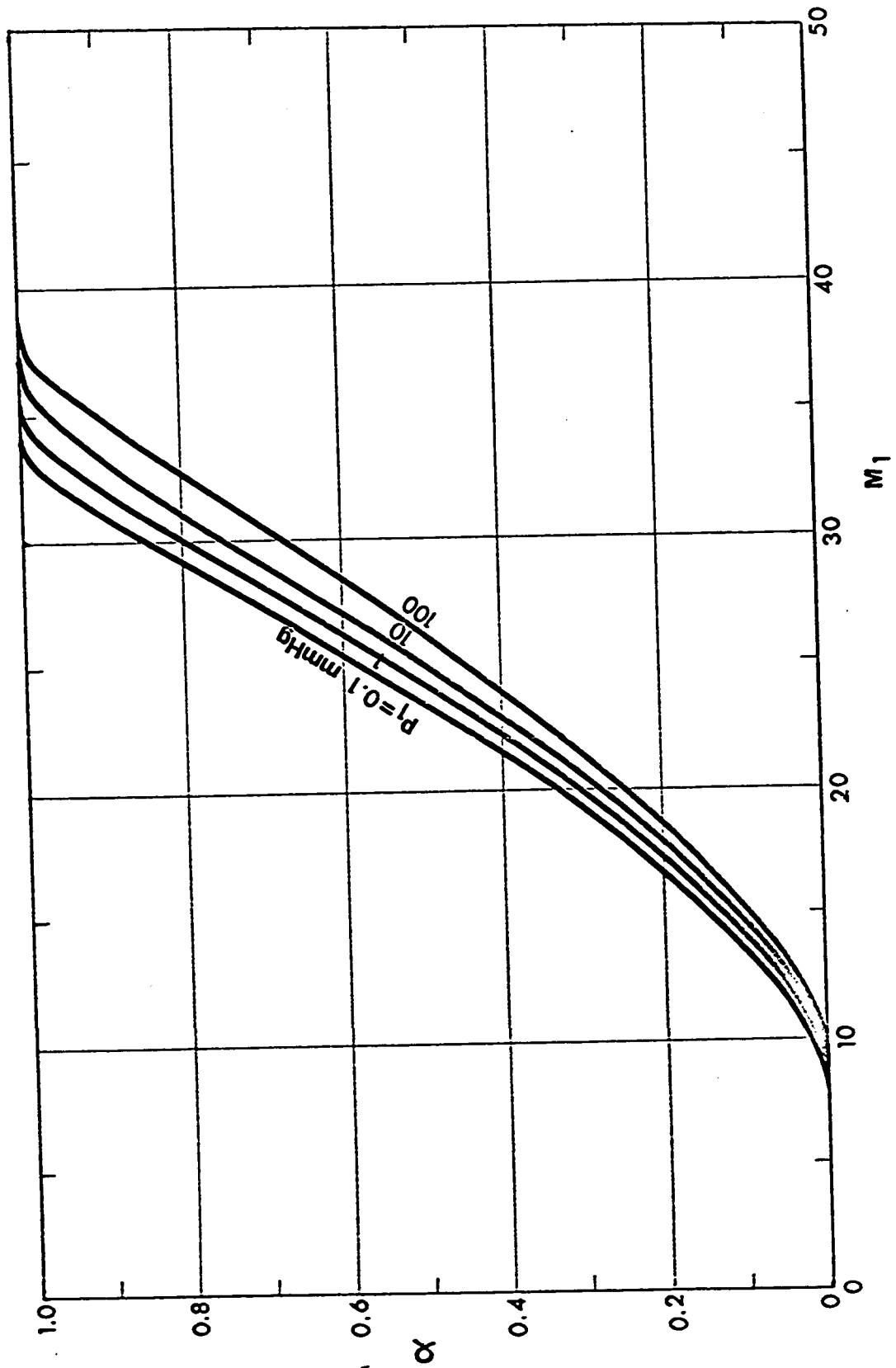
FIG. 4.5 α vs M_1 for incident argon shock.

Roughly speaking, dissociation becomes important at 0.3 eV, dissociation

is about complete and ionization sets in at 1 eV and at 2.5 eV, ionization

is of the order of 50%. The general expression for specific heat at

constant volume can be written as (4.3),

$$C_V = \frac{fk}{2m} + \sum_{\nu} \frac{k\left(\frac{h\nu}{kT}\right)^2 e^{\frac{h\nu}{kT}}}{m\left(e^{\frac{h\nu}{kT}} - 1\right)^2} \quad . \tag{4.22}$$

4.1.2 Reflected Shock

When a primary or incident shock wave reaches the end of a shock tube

it will be reflected back into the gas which has already been heated by

the passage of the incident shock (4.4). This results in a further

increase in the temperature, pressure and density of the gas. To derive

the equations for the quantities in the reflected shock it is more

convenient to do so in terms of the conditions in the incident shock.

From the equations derived, these properties may then be related to the

initial conditions by way of the Mach number.

With a reference frame moving with the reflected shock front whose

speed is U_R, the Rankine-Hugoniot relations can be expressed in the same

form as Eqs. 4.1-4.6, except that the subscripts 1 and 2 of ρ, p, T and

H are changed into 2 and 3, respectively, and that U and M_1 changed into

u_2' and M_R, respectively. In this case M_R has the form of,

$$M_R = \frac{u_2'}{c_2} = \frac{U_R + u_2}{c_2} \quad . \tag{4.23}$$

The parameters behind the reflected shock wave can be seen in Eqs. 4.9-

4.12 and 4.15-4.21, with the same changes in the subscripts. Equations

---

(4.3) J.K. Wright: "Shock Tubes" John Willy & Sons Inc. N.Y. pp24 (1961)
(4.4) A.G. Gaydon & I.R. Hurle: "The Shock Tube in High Temperature
       Chemical Physics" Reinhold Publishing Co. N.Y. (1963)

4.15-4.21 are applicable when there is no further ionization in the reflected shock. From Eqs. 4.18 and its equivalent form in the reflected shock region, we obtain,

$$u_2 = \frac{2(M_1^2-1)}{(\gamma+1)M_1} c_1 = \frac{2(M_R^2-1)}{(\gamma+1)M_R} c_2 \qquad (4.24)$$

$$\text{or} \qquad M_R = \sqrt{\frac{2\gamma M_1^2-(\gamma-1)}{(\gamma-1)M_1^2+2}} \cdot \qquad (4.25)$$

From this equation it can be seen that even with $M_1=\infty$, $M_R=(2\gamma/\gamma-1)^{\frac{1}{2}}$ ($=\sqrt{5}$ for argon). Therefore the further increase in the density and temperature in the reflected shock is not very large and Eqs. 4.15-4.21 can be used as a good approximation for the properties of the reflected shock. Also if $M_1 \geq 7$ in argon shock, then we can approximate that,

$$M_R=\sqrt{5}, \quad \rho_3/\rho_2=2.5, \quad p_3/p_2=6, \quad T_3/T_2=2.4, \quad u_2/c_2=3$$

$$\text{and} \quad U_R/U=0.5. \qquad (4.26)$$

4.1.3 Generation of Shock Heated Gas by a Shock Tube

For some shock tube conditions a contact surface is never established and the ambient and driver gases are thoroughly mixed. Several explanations of this behavior have been put forward; Rayleigh-Taylor instability of the contact surface (4.5), inertial instabilities (4.6), and turbulent mixing across the contact discontinuity (4.7). According to Pert (4.8) the flow is dominated by turbulence and the shock heated gas is thoroughly mixed

(4.5)   J.P. Barach & R.E. Vermillion: Phys. Fluids 8 1976 (1965)
        G.I. Taylor: Proc. Roy. Soc. A201 192 (1950)
(4.6)   G.D. Cormack: Z. Naturforsch 19a 934 (1964)
(4.7)   J.P. Barach & T.W. Mayers; Phys. Fluids 11 89 (1968)
(4.8)   G.J. Pert: J. Appl. Phys. 39 5932 (1968), J. Phys. D, Appl. Phys. 3 203 (1970)

behind the shock front at low initial gas pressure (<0.5 mm) and high

shock speed (>4 cm/μs), so that no separated shock layer is found. The

gas behind the front is predominantly due to the collected driven gas (for

the axial distance much longer than the length of the driver) and accordingly

the state of the gas is approximately given by the shock relations, if the

turbulent energy is not too large. However, at high initial gas pressure

(>1 mm) and low flow speed (<2 cm/μs) a shock structure is formed with a

well developed boundary layer.

The condition for onset of turbulence in the flow can be described

in terms of a hydrodynamic Reynold's number,

$$Re = \frac{\rho u d}{\eta} , \tag{4.27}$$

where η is the viscosity (values for argon are given in Fig. 4.6) and d is

the diameter of the expansion tube; i.e., with Re smaller than 9000, the

shock heated gas is separated from the driver gas (4.8).

4.1.4 Flow Duration in the Shock Tube

The length L of the slug of the shock processed gas contained between

the shock front and the contact surface satisfies the relation $\rho_2 L = \rho_1 z$,

where z is the axial distance from the driver to the specified point, so

that the ideal flow duration, τ, is given by

$$\tau = \frac{L}{u_2} = \frac{z}{c_1 M_1 (\eta - 1)} . \tag{4.28}$$

It is well known, however, that the actual flow durations are

shorter than the ideal values; a factor of ½ has been used as a rule of

thumb which is useful at higher pressures (>5 mmHg). At low values of p_1,

FIG. 4.6   Frictional viscosity for argon as a function

of temperature at 1 atm (4.9).
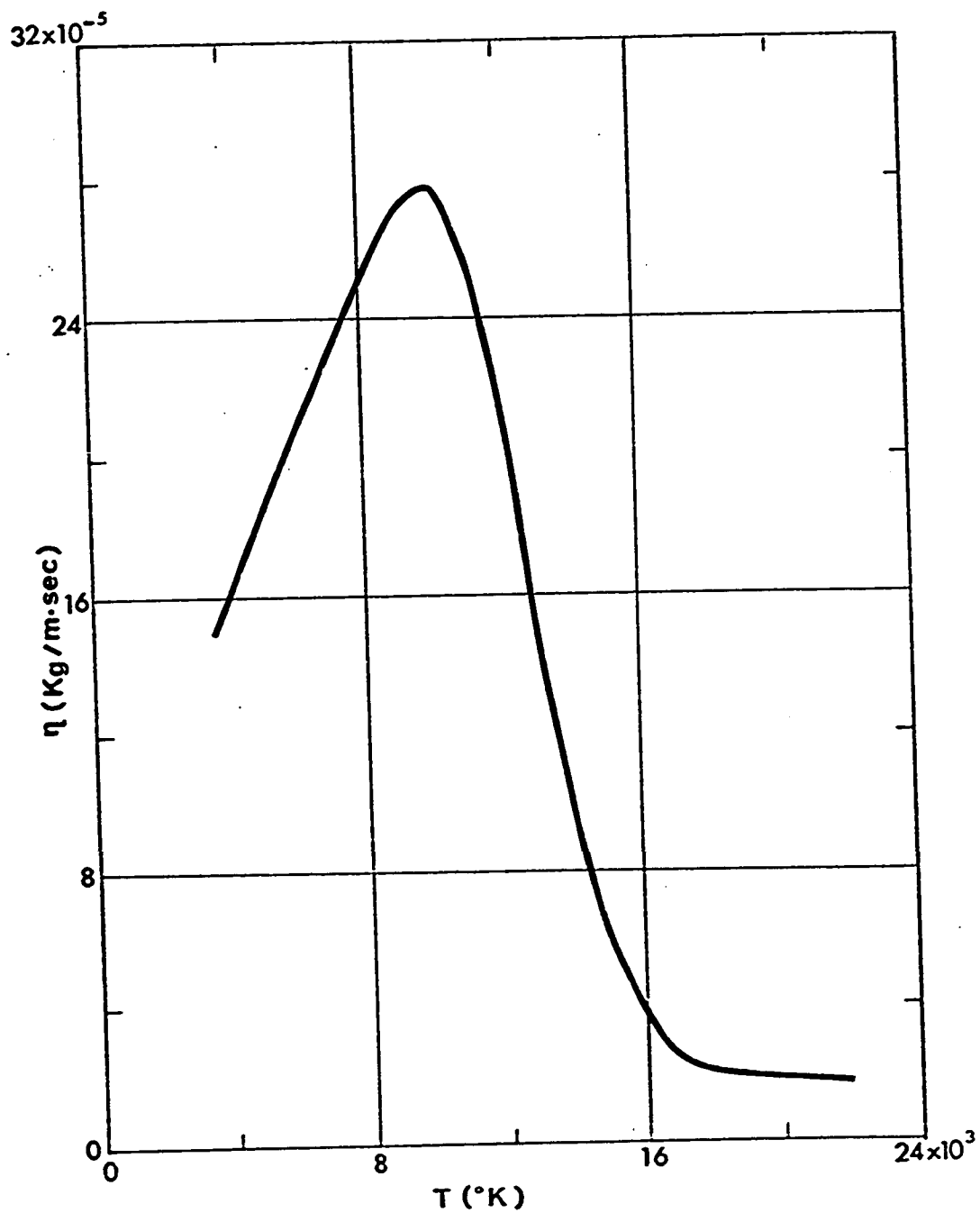
the factor can be much less than ½. The severe effect at low pressures
was first noted by Duff (4.10), who found that, at given p_1, there is a
limiting value of τ, i.e., τ cannot be increased infinitely with increasing
z. He gave a qualitative explanation of the loss, noting that the low
speed gas in the boundary layer near the wall "leaks" past the contact
surface. The theoretical values of τ as well as the experimental values
are shown in the report of Roshko (4.11). These measured values fall below
the theoretical real-gas curve. The discrepancy increases with increasing
Mach number and decreasing initial pressure.

4.2 THEORETICAL DERIVATION OF THE PLASMA VELOCITY

The model used for the electromagnetically driven shock in this
theory is the "finite energy snow plough with leakage" model. Let us
consider the energy balance equation so that ionization effects and
frictional energy losses to the shock tube wall can easily be taken into
account. The shock driver emits a driving gas slug (plasmoid) of the mass
defined by mn_1L per unit area of the shock tube cross section. L is
determined experimentally from the product of the plasma length at the
driver mouth and the ratio of the particle densities of the shock heated
gas and the unheated gas ($=n_2/n_1$) at the same position. (It was experimentally
found that L is very weakly dependent on the driver energy and ambient gas
pressure, which makes this theory simple and useful. See Sec. 4.3.7) This

(4.9) R.S. Devoto: Phys. Fluids $\underline{10}$ 354 (1967)
(4.10) R.E. Duff: Phys. Fluids $\underline{2}$ 207 (1959)
(4.11) A. Roshko: Phys. Fluids $\underline{3}$ 835 (1960)

plasmoid works as a piston and compresses the undisturbed gas ahead. By doing so the driving gas feeds its internal and kinetic energies into the compressed gas. The shock heated gas is not well separated from the driving gas by the contact surface, but tends to diffuse into it as mentioned in Sec. 4.1.4.

In the case of the pressure driven shock tube, the actual length of the shock heated gas is reduced by a factor k (=0.1-0.5, depending on the initial pressure and Mach number) from the theoretical value. For our electromagnetically driven shock tube where the mixing is more severe this factor k is smaller and can be regarded as a ratio of the number of particles which moves with the driving gas slug to the total number of particles which are affected by the shock (snow plough rate); i.e., only kn_1z particles out of n_1z particles start moving with the driving gas slug, and the others lose their energies by frictional force between the shock tube wall and by diffusion to the wall. The mass of the driving gas per unit area at z can, therefore, be expressed as $mn_1(L+kz)$.

By equating the energy loss of driving plus shock heated gas and the energy gain of undisturbed gas during the period the shock proceeds a distance Δz, we obtain,

$$\Delta(m_i n_1 (L+kz)(\tfrac{1}{2}u_2^2+H_2)) = -m_i n_1 \Delta z(\tfrac{1}{2}u_2^2+H_2), \tag{4.29}$$

where H is the internal energy expressed by Eq. 4.6 with the assumption of $H_2 \gg H_1$. This equation can be rearranged to,

$$\frac{L+kz}{1+k}\frac{2}{u_2^2+2H_2}\left(u_2\frac{du_2}{dM_1}+\frac{dH_2}{dM_1}\right)\frac{dM_1}{dz}+1=0. \tag{4.30}$$

By eliminating u_2 and H_2 by using Eqs. 4.6, 4.9, 4.10 and 4.12, we obtain,

$$\frac{L+kz}{1+k}\frac{J(M_1)}{G(M_1)}\frac{dM_1}{dz}+1=0, \tag{4.31}$$

where
$$J(M_1)=(\gamma-1)(\eta-1)M_1\left(M_1\frac{d\eta}{dM_1}+\eta^2-\eta\right)+2\gamma M_1\eta(\eta-1)+\left(2\gamma M_1^2-\gamma\eta M_1^2-\eta\right)\frac{d\eta}{dM_1}$$
$$+\frac{(\gamma-1)\eta^3 e V_i}{c_1^2\,m_i}\frac{d\alpha}{dM_1}\,, \qquad (4.32)$$

and
$$G(M_1)=\frac{\gamma-1}{2}\eta(\eta-1)M_1^2+\eta\left(\eta+\gamma\eta M_1^2-\gamma M_1^2\right)+\frac{(\gamma-1)\eta^3\alpha e V_i}{c_1^2\,m_i}\,, \qquad (4.33)$$

By normalizing z as $Z=(1+k)z/L$, equation 4.31 is reduced to,

$$\frac{dZ}{dM_1}+\left(1+\frac{k}{1+k}Z\right)\frac{J(M_1)}{G(M_1)}=0. \qquad (4.34)$$

The first term of $J(M_1)$ arises from the change in kinetic energy, the second and third terms from the change in internal energy, and the fourth term from the energy increase by ionization. In $G(M_1)$ the first term is kinetic energy and the other terms are internal energies.

Equation 4.34 was solved numerically with the boundary conditions $M_1=M_{10}$ and $u_2=u_{20}$ at $t=0$, with $k=0.1-1$. Figure 4.7 shows how each term in Eqs. 4.32 and 4.33 affects the plasma velocity. $L=0.4$ m and $k=0.1$ were used here.

Curve A: $d\alpha/dM_1\neq0$ follows the Saha equation

Curve B: $d\alpha/dM_1=0$ de-ionization energy goes into the shock tube wall

Curve C: $dH_2/dM_1=0$ internal energy change is neglected

Curve D: $H_2=0$ internal energy is neglected.

The initial pressure dependence was found to be very small for $p_1=0.1-100$ mmHg. Especially for the case of Curve D, Eq. 4.34 can be solved as,

$$u_2=\frac{u_0}{\sqrt{Z+1}}=\frac{u_0}{\sqrt{\frac{1+k}{L}z+1}}\,. \qquad (4.35)$$

In deriving Eq. 4.31 it was assumed that the pressure, density and temperature of the driving gas slug are the same as those of the shock heated gas whose parameters are described by the shock relations. The

FIG. 4.7   The effect of various terms in Eqs. 4.32 and 4.33 on the plasma velocity decay.
$k=0.1$, $L=0.4$ m, $P_1=0.1$-10 mmHg and $M_{10}=50$.

A; $\dfrac{d\alpha}{dM_1} \neq 0$

B; $\dfrac{d\alpha}{dM_1} = 0$

C; $\dfrac{dH_2}{dM_1} = 0$

D; $H_2 = 0$

U_2 (cm/μs)

z (cm)
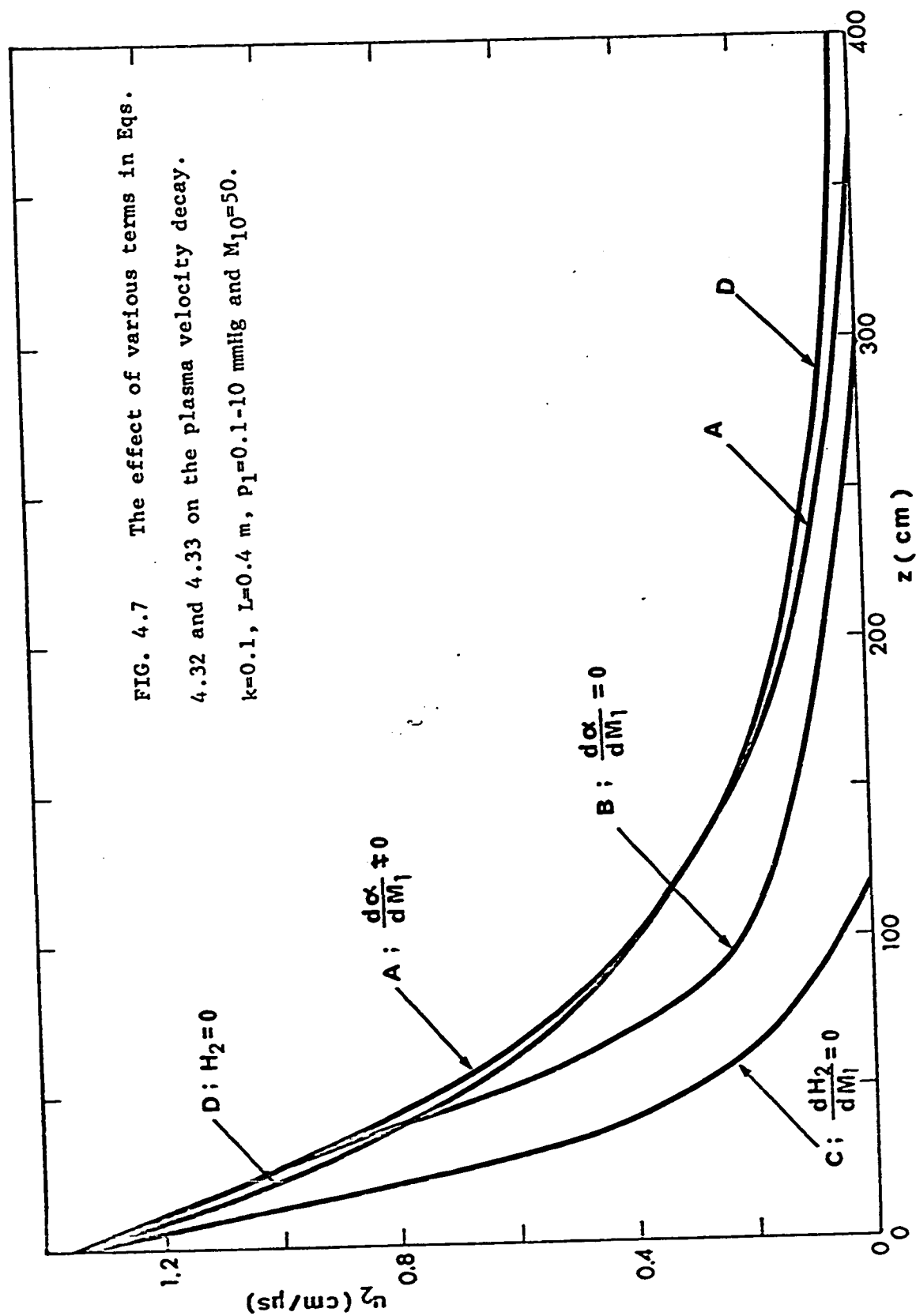
validity of this assumption was verified experimentally by Pert (4.8).

However, when the plasma density is low, the loss of the charged particles by ambipolar diffusion to the wall becomes larger than the loss by volume recombination, in which case most of the energy released by de-ionization is fed into the wall, not into the oncoming neutral particles. Therefore in the expression of $J(M_1)$, we may set, for the low density plasma,

$$\frac{d\alpha}{dM_1} = 0. \qquad (4.36)$$

The crossover takes place when the volume recombination time constant (τ_r) of Eq. 2.39 is equal to the ambipolar diffusion time constant (τ_a) of Eq. 2.33. For 1" radius shock tube with the pressure of 1 mmHg, the crossover density is $n_e = 2 \times 10^{12}$ cm^{-3}. If the neutral density becomes higher, then τ_a becomes longer, recombination dominates, the $u_2(z)$ curve approaches the curve A of Fig. 4.7 (broken lines of Fig. 4.9), and so the plasma velocity tends to have a lower decay rate. On the other hand if the plasma density becomes lower, then τ_r becomes longer, ambipolar diffusion becomes dominating and $u_2(z)$ curve approaches the curve B of Fig. 4.7 (solid lines of Fig. 4.9). It is worth noting that the curve A can be approximated well by the curve D of Eq. 4.35.

In Fig. 4.8 is shown the variation of $u_2(z)$ with respect to k when $d\alpha/dM_1 = 0$. Curves for $u_2(z)$ with various initial conditions, M_{10}, are shown in Fig. 4.9 when $d\alpha/dM_1$ is zero and non-zero.

In this theory the expansion wave emitted by the shock as it slows down was neglected. However, this effect becomes important when the shock Mach number is low and the difference between U and u_2 are appreciable that the shock deceleration is strong. Consequently, the theory introduced here might have an appreciable error at low shock speeds.

FIG. 4.8   The effect of k on the plasma velocity decay.

L=0.4 m, P_1=0.1-1.0 mmHg, M_{10}=50 and $d\alpha/dM_1$=0.

FIG. 4.9   The variation of the plasma velocity as a function of axial distance at various initial speeds. k=0.1, L=0.4 m and p_1=0.1-10 mmHg. The solid lines are for $d\alpha/dM_1$=0 and the dotted lines are for $d\alpha/dM_1 \neq 0$.
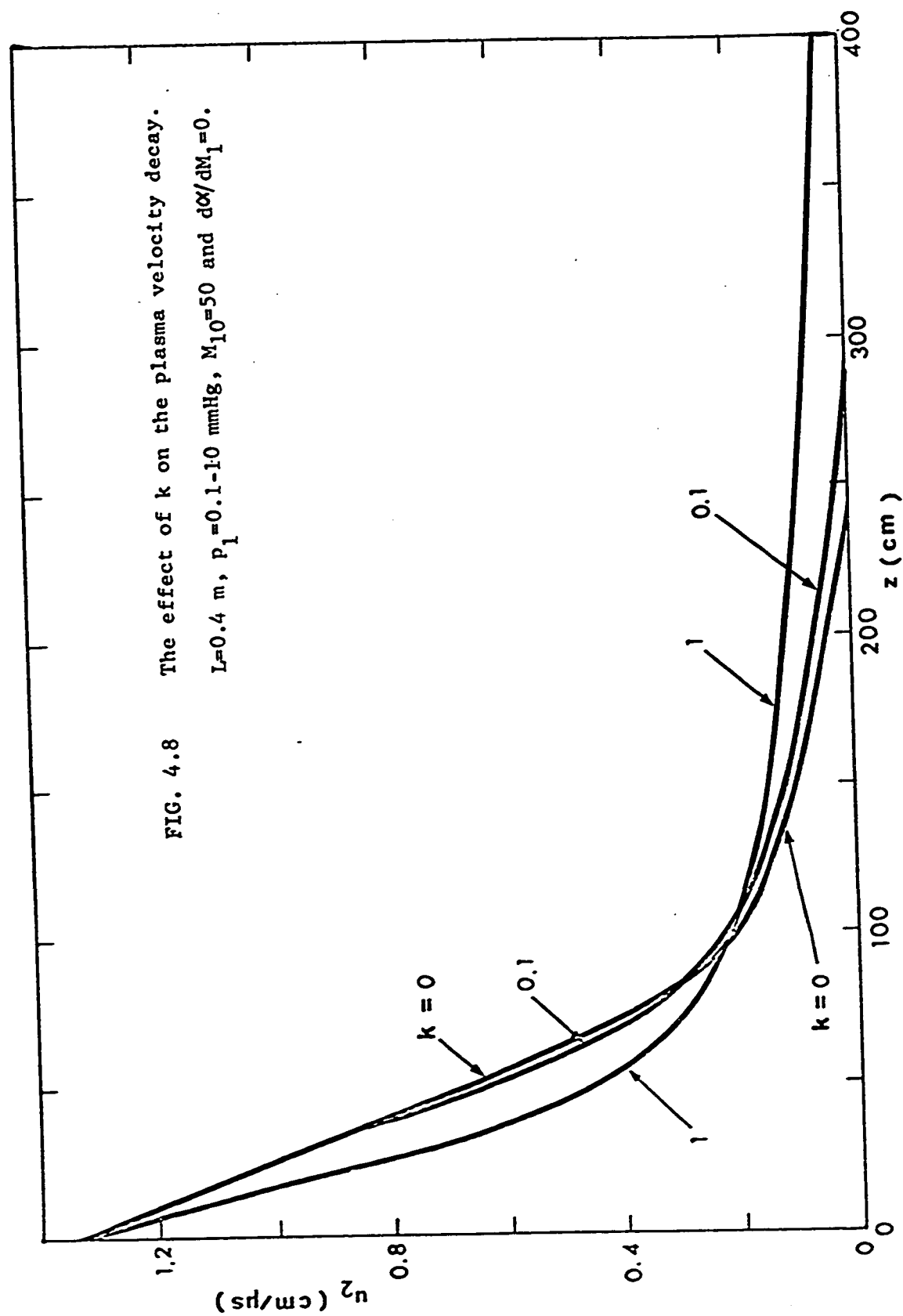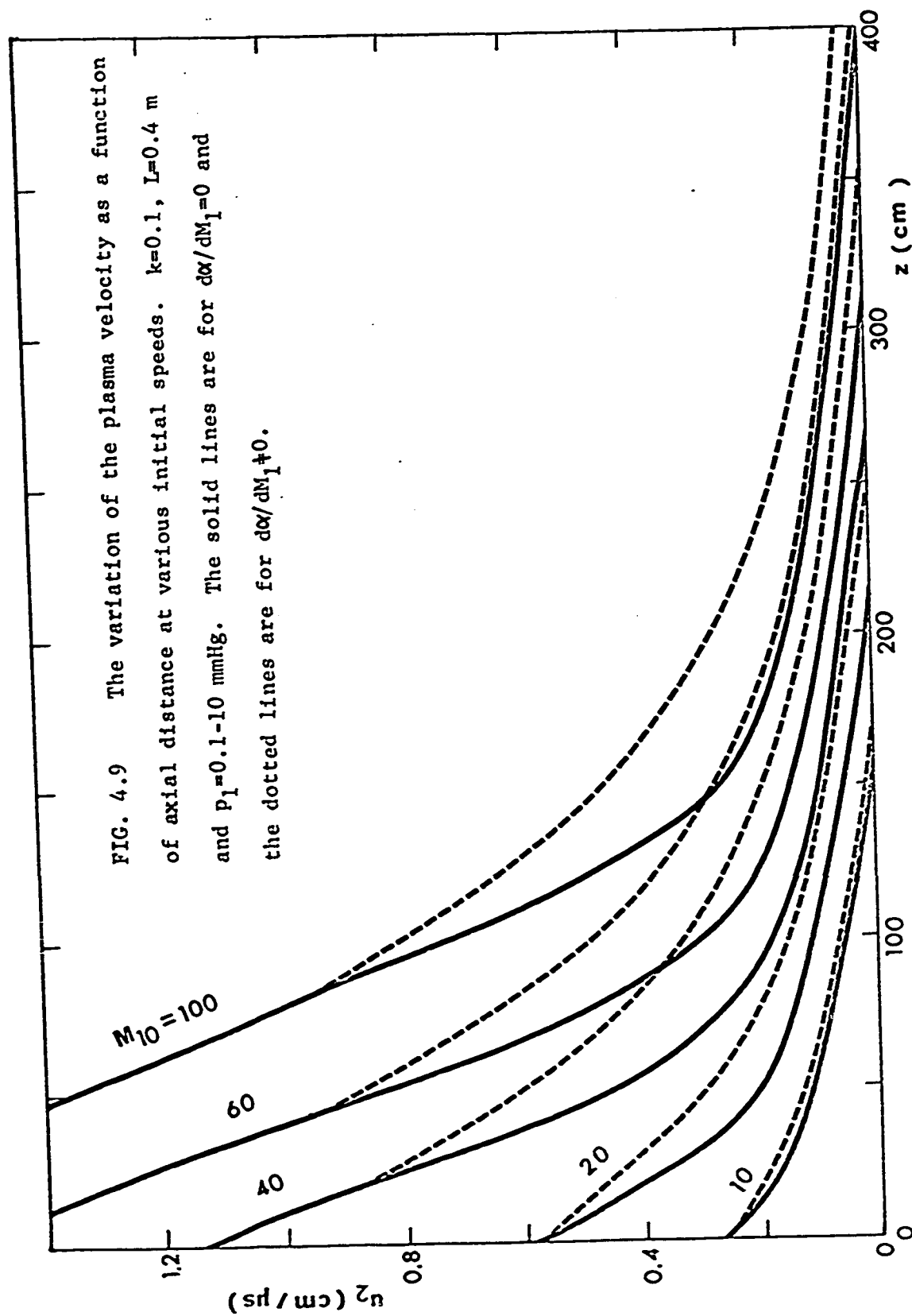
4.3 MEASUREMENTS IN THE SHOCK TUBE

4.3.1 Plasma Velocity Measurements

The velocity of the plasma was measured by both photodiode and r.f. conductivity probes with the time of flight method. The photodiode measures the time of arrival of the peak luminosity, i.e., the peak plasma density (4.12), and the conductivity probe measures the time of arrival of the peak plasma temperature (Eq. 2.9). The experimentally obtained plasma velocities by these two methods agree well as seen in Fig. 4.10.

Some of the experimental results are shown in Fig. 4.11 where theoretical curves are also shown. The agreement between them is very good except for low plasma velocities (M<5).

4.3.2 Flow Duration Measurements

Two methods of measuring the flow duration were employed; the two coil r.f. conductivity probes (Cases 1, 3, 4 and 5 in Table 4.1) and the combination of piezo electric pressure probe and electrostatic probe (Cases 2 and 6 in Table 4.1). The typical oscilloscope traces for the first method are shown in Fig. 4.12. In the second method the pressure

---

(4.12) The power density radiated by electrons which are accelerated by the interaction with ions (Bremsstrahlung) is,

$$W = \frac{Z^2 e^6 n_i n_e}{8\sqrt{6}\pi \epsilon_0^3 c^3 m_e h} \sqrt{\frac{8kT_e}{\pi m_e}} = 1.4 \times 10^{-40} Z^2 n_i n_e \sqrt{T_e} \quad (W/m^3), \quad (4.37)$$

which is approximately proportional to the square of the electron density.
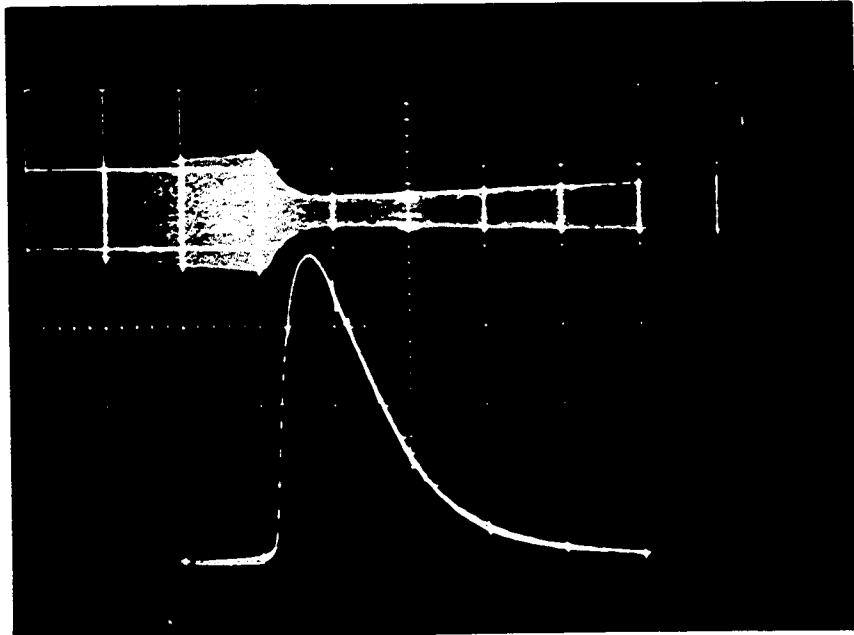
FIG. 4.10
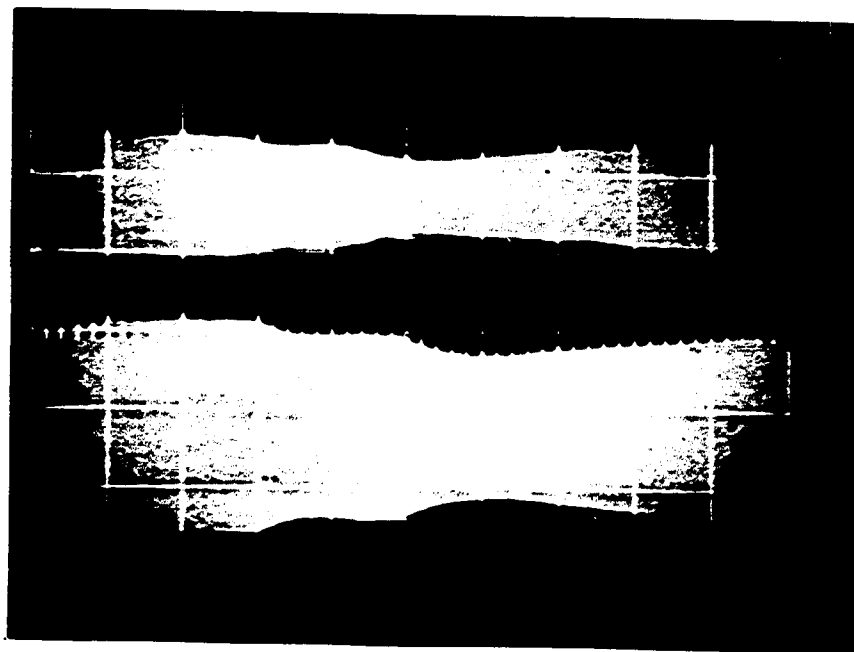
FIG. 4.12

FIG. 4.10   The plasma velocity measurements by two methods. The upper beam is the signal of r.f. conductivity probe (5 mV/vertical div.) and the lower beam is the photodiode signal (1 V/vertical div.) Time base is 50 μs/div. Both signals were taken at z=100 cm with p_1=0.15 mmHg in argon and V_c=2.5 KV.

FIG. 4.12   Typical oscilloscope traces of r.f. conductivity probe (case 3 of Table 4.1). Vertical and horizontal deflections are 0.05 V/div. and 200 μs/div. Time runs from left to right. The upper trace was taken at z=154 cm from the driver and the lower trace at z=146 cm. The pinch of the upper trace during 0-100 μs is due to the precursor ionization, the pinch during 600-800 μs to the shock heated gas and the pinch during 800-1600 μs to the driving plasmoid.

FIG. 4.11   The experimental and theoretical plasma velocity

as a function of axial distance.

experimental, $p_1 = 0.1$ mmHg

"   0.1 mmHg

"   1 mmHg

"   5 mmHg

theoretical, $k=0.1$, $L=0.4$ m and $d\alpha/dM_1 = 0$.
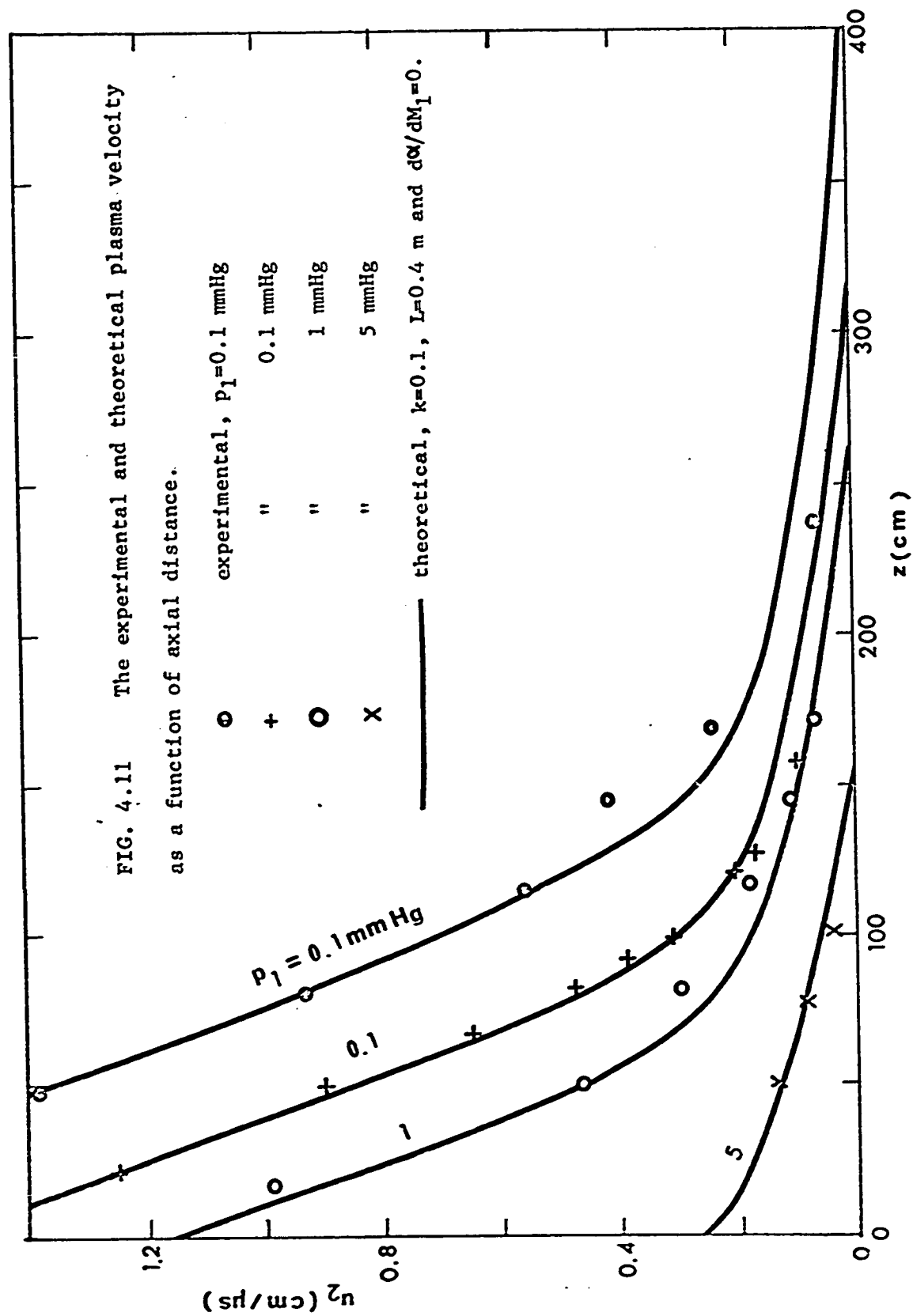
probe detects the arrival of the shock front, while the electrostatic probe detects the arrival of the driver gas.

Some of the results are summarized in Table 4.1 where the measured values are compared with theory. Considering the results of Duff (4.10) and Roshko (4.11) the agreement can be said to be reasonable.

4.3.3 Pressure Measurements

Measurements of the pressure of the shock heated gas give us information on the validity of the shock relations. The experimental values of p_2 obtained by the piezo electric pressure probe agree well with that of theory (p_2*) when Re<9000, as seen in Table 4.1. When Re becomes larger, the indicated values are greater than the experimental values. This is probably due to the leakage of the shock heated gas through contact surface along the boundary layer on the shock tube wall.

4.3.4 Plasma Density Measurements

In the first measurements with the floating double probes, one of the probes was aligned perpendicular to the plasma flow, while the other was parallel to the flow. Some of the results are listed in Table 4.2 and the typical V-I characteristics for these measurements are shown in Fig. 4.13 (which corresponds to Cases 1, 2 and 3 of Table 4.2). With a probe voltage, V_d, larger than 10 volts, the probe currents can be seen to be proportional to $V_d^{\frac{1}{2}}$, as expected by the collision dominated theories (Eq. 2.74).

case	Initial pressure P_1(mmHg)	bank voltage V_C(KV)	axial distance z(cm)	$M=\dfrac{u_2}{c_1}$	flow duration measured τ(μs)	flow duration calculated τ^*(μs)	pressure measured P_2(mmHg)	pressure calculated P_2^*(mmHg)	Reynold's number Re
1	0.1	4	80	50	0	10	180	300	57000
2	0.1	4	180	17.5	80	35	43	46	2500
3	0.5	2.5	150	3.43	250	650	—	—	2000
4	1	4	80	22	0	11	270	600	67000
5	1	4	150	5.6	150	314	—	—	5100
6	1	4	180	5.3	320	400	36	35	4900

TABLE 4.1   Some results on the flow duration and pressure measurements.

case	z (cm)	M	t_{arr} (μs)	$\frac{r_p}{\lambda_i}$	T_e^* (°K)	calculated $(I_\perp/I_\parallel)_1$	$(I_\perp/I_\parallel)_2$	measured $I_\perp/I_\parallel$	$J_\parallel$ (A/m)	n_e^* (m⁻³)	$n_e^{(1)}$ (m⁻³)	$n_e^{(2)}$ (m⁻³)	$n_e^{(3)}$ (m⁻³)
1	50	31.2	50	0.518	3.24×10^4	0.55	0.34	0.64	200	1.7×10^{22}	1.6×10^{22}	5.4×10^{21}	6.6×10^{22}
2	80	15.3	100	0.537	1.05×10^4	0.49	0.34	0.56	82	4.3×10^{21}	1.2×10^{22}	4.0×10^{21}	2.6×10^{22}
3	111	7.47	175	0.235	0.51×10^4	0.39	0.34	0.50	16	1.2×10^{17}	1.6×10^{21}	1.1×10^{21}	3.6×10^{21}
4	142	4.05	400	0.210	0.28×10^4	0.25	0.34	—	0.082	—	9.4×10^{18}	8.6×10^{18}	1.8×10^{18}

TABLE 4.2   Some results on the plasma density measurements.

T_e^* calculated from the conductivity/shock relations

$I_\parallel$ current into the parallel probe at $V_d = 20$ V

$I_\perp$ current into the perpendicular probe at $V_d = 20$ V

$(I_\perp/I_\parallel)_1$ ion current ratio calculated from Eq. 4.38

$(I_\perp/I_\parallel)_2$ ion current ratio calculated from Eq. 4.39

$(I_\perp/I_\parallel)_3$ ion current ratio calculated from Eq. 4.40

n_e^* electron density calculated from T_e^*

$n_e^{(1)}$ calculated from $I_\parallel$ and Eq. 2.57 (collisionless theory)

$n_e^{(2)}$ calculated from $I_\parallel$ and Eq. 2.63 (Collision dominant theory)

$n_e^{(3)}$ calculated from $I_\perp$ and Eq. 2.74 (electrical boundary layer theory)

case	p_1 (mmHg)	V_C (KV)	z (cm)	M	t_{arr} (μs)	$\frac{r_p}{\lambda_\perp}$	T_e^* (°K)	calc. $\left(\frac{I_\perp}{I_\parallel}\right)_3$	meas. $J_\perp$ (A/m)	n_e^* (m-3)	$n_e^{(1)}$ (m-3)	$n_e^{(2)}$ (m-3)	$n_e^{(3)}$ (m-3)
5	1	4.5	30	14.6	70	4.54	1.14×10^4	2.6	30	4.9×10^{21}	8.0×10^{19}	4.2×10^{21}	2.1×10^{21}
6	1	3.5	30	11.1	80	3.12	0.96×10^4	2.6	17.5	1.4×10^{21}	9.6×10^{19}	3.4×10^{21}	1.1×10^{21}
7	1	2.5	30	7.3	100	2.38	0.51×10^4	2.6	5.0	1.2×10^{19}	5.8×10^{19}	1.7×10^{21}	2.7×10^{20}
8	1	1.5	30	3.65	200	2.0	0.14×10^4	2.6	0.38	—	9.4×10^{18}	3.3×10^{20}	1.3×10^{19}
9	1	4.5	90	9.3	200	2.5	0.78×10^4	2.6	3.8	5.2×10^{20}	2.6×10^{19}	9.0×10^{20}	1.6×10^{20}
10	1	3.5	90	4.7	300	2.18	0.23×10^4	2.6	0.93	—	1.8×10^{19}	6.1×10^{20}	3.7×10^{19}
11	10	4.5	90	1	500	6.17	0.03×10^4	2.6	0.00075	—	2.7×10^{14}	8.7×10^{17}	2.4×10^{16}

TABLE 4.2 - cont'd   Some results on the plasma density measurements.

FIG. 4.13   Typical V-I characteristics of parallel/perpendicular floating

double probe. One of the probes was aligned parallel to the flow while the

other was perpendicular to the flow.
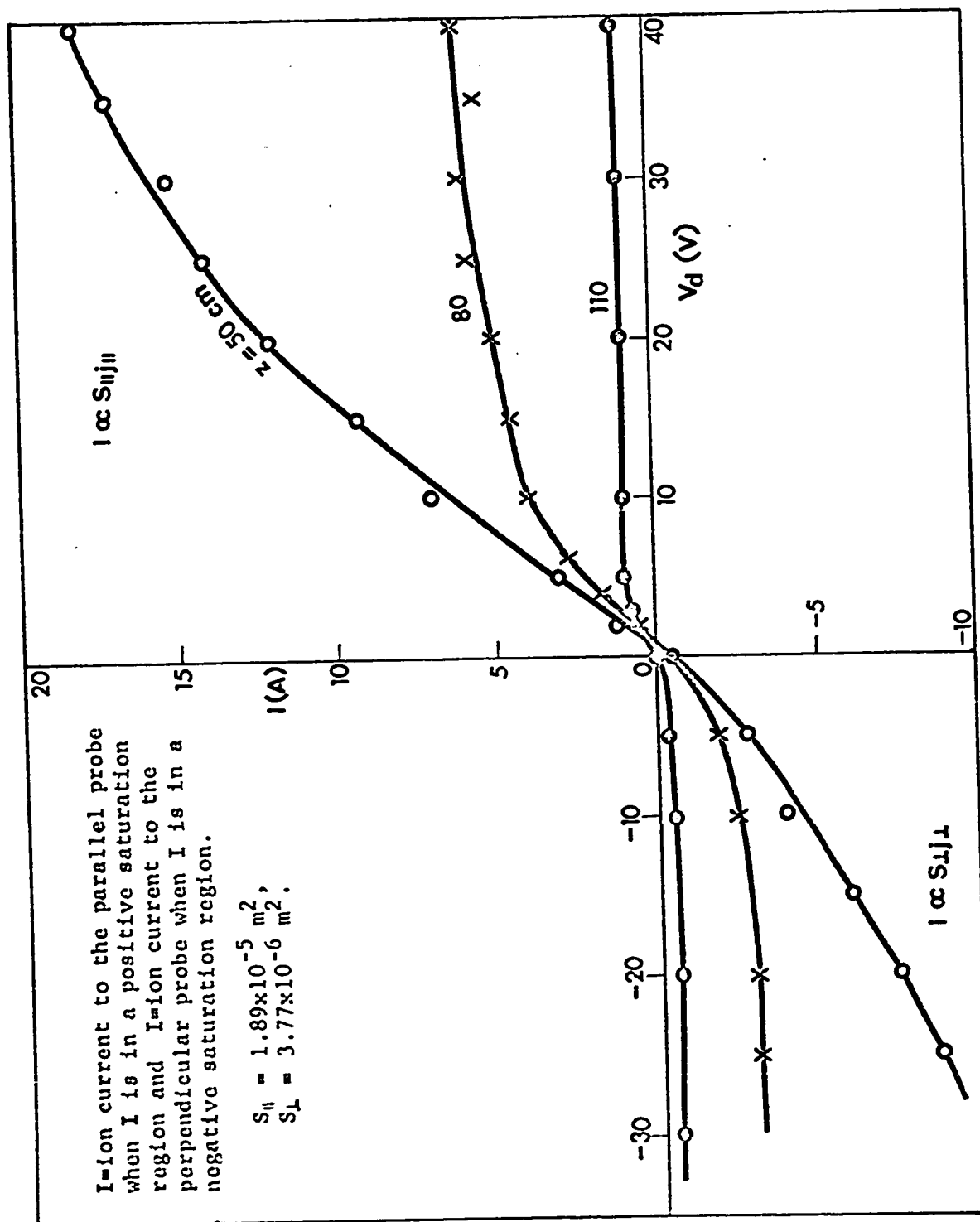
The ratio of $I_\perp/I_\parallel$ was calculated in three ways. Since the parallel probe also was a hair pin type, there still remained a small portion (length $L_{2\perp}$) which was perpendicular to the flow, besides the large portion (length $L_{2\parallel}$) of the parallel part. The nominal length of the probe was $L_{2\perp}+L_{2\parallel}$. The perpendicular probe (length $L_{1\perp}$) did not have any parallel component to the flow. The radii of both probes were the same. The three methods were:

(1) Collisionless case: From Eq. 2.68,

$$\left(\frac{I_\perp}{I_\parallel}\right)_1 = \frac{L_{1\perp}}{\frac{\sqrt{\pi}}{2C}L_{2\parallel}+L_{2\perp}},$$ (4.38)

where L_1=12 mm, L_2=56 mm, L_2 =4 mm and r_p=0.05 mm.

(2) Collision dominant, this sheath case ($R_E\alpha^2\chi^2 \ll 1$): From Eqs. 2.71 and 2.77,

$$\left(\frac{I_\perp}{I_\parallel}\right)_2 = \frac{L_{1\perp}}{\frac{1}{\sqrt{\pi}}L_{2\parallel}+L_{2\perp}} = 0.34.$$ (4.39)

(3) Collision dominant, moderate sheath case ($R_E\alpha^2\chi^2 \gg 1$): From Eqs. 2.74 and 2.81,

$$\left(\frac{I_\perp}{I_\parallel}\right)_3 = \frac{5.3 L_{1\perp}}{9.36 r_p^{3/4}L_{2\parallel}^{1/4}+5.3 L_{2\perp}} = 2.6$$ (4.40)

The aim of the second measurements was to check the electron density obtained by the double probe method. Cases 1-4 of Table 4.2 are for long ion mean free paths and cases 5-11 are for short mean free paths. Since, in all the cases the ratio r_p/λ_i were not sufficiently different from unity, electron densities were determined by using three different methods: (1) Lam's theory for collisionless plasma in which case n_e are denoted by $n_e^{(1)}$. (2) Collision dominated theory with Eqs. 2.63 and 2.64, with $n_e^{(2)}$. (3) Collision dominated sheath with electrical boundary layer theory of Eq. 2.74, with $n_e^{(3)}$.

For large λ_i, $n_e^{(1)}$ agrees with $n_e^{(2)}$ but not with $n_e^{(3)}$, since

$n_e^{(3)}$ does not take into account the current due to ambipolar diffusion. This makes the calculated density larger than the true value. However, for short λ_i, it is $n_e^{(1)}$ that does not coincide with other n_e's. Electron densities determined by the conductivity measurements, shock relations and Saha equations agree with $n_e^{(1)}$ for large λ_i or $n_e^{(3)}$ for small λ_i, as long as M is greater than 8. With M<8 the plasma density is too low for the Saha equation to hold, i.e., density loss by diffusion to the wall becomes greater than recombination loss. In addition, the temperature of the shock heated gas is too low for further ionization to occur. Therefore, for the determination of electron density, the shock relations are no longer valid and the driving gas alone determines the electron density.

Figure 4.14 shows the plot of the electron density against time measured from the initiation of the driver discharge (t_{arr}) for the cases 1-4 of Table 4.2.

The plasma density was measured by the microwave cavity method in order to check the electrostatic probe method. The cavity was set at 230 cm from the driver. With V_c=2.5 KV and p_1=0.1 mmHg, we obtained f=0.8 MHz and $\varepsilon/\varepsilon_0$=2.03, which yielded that n_e=6.3x10^9 cm^{-3}. For this plasma ν_m=8x10^8 sec^{-1}, ω_p=4.5x10^9 sec^{-1} and ω=1.5x10^{10} sec^{-1}, which satisfie the conditions that $\eta \ll 1$ and $\gamma \ll 1$ of Eq. 3.2. The measured point thus obtained is also plotted in Fig. 4.14.

FIG. 4.14   Plasma density decay with respect to time.

P₁=0.1 mmHg and V_C=2.5 KV.
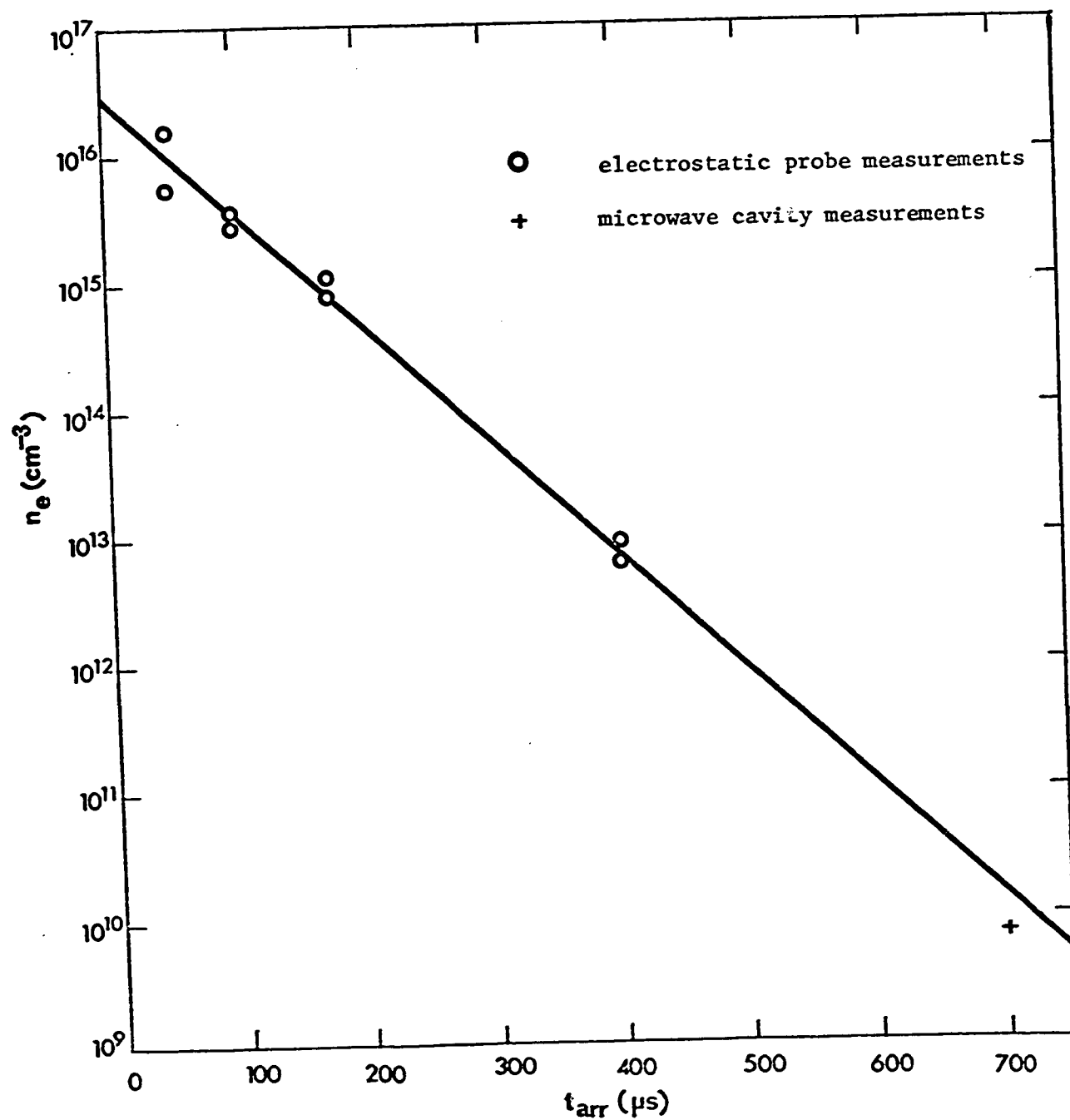
4.3.5 Electron Temperature Measurements

The electron temperature of the argon plasma with V_c=2.5 KV, P_1= 0.1 mmHg and z=80 cm from the driver was measured. The results for two kinds of electron collecting probes (Sec. 3.2.4) are shown in Fig. 4.15. The dotted lines were taken without a dummy probe and the solid lines were taken with a dummy probe. (ΔV was subtracted from the values of dotted lines to obtain the solid lines.) The slopes of the curves yield 2.0 eV for the 0.1 mm diameter probe and 2.1 eV for the 1 mm diameter probe. The electron density cannot be found because of the ambiguity of the probe area, since the probe surfaces were badly contaminated after a few shots. Note that the floating potential has a larger value (-20 volts) than the expected value by calculation with T_e=2 eV (9.5 volts), because at the floating potential the probes collect only the fast electrons as mentioned in Sec. 3.2.4.

The speed of the plasma at the probe position was 0.75 cm/μs (M=23.4) from the photodiode measurements. From the shock relations it is predicted that T_e=1.4 eV and n_2/n_1=10. This result is compared with the conductivity measurements in Table 4.3. The mean free path between electrons and neutrals becomes 4.4×10^{-3} m, which is much larger than the probe radius. The effect of the plasma flow can be neglected as mentioned in Sec. 2.5. The electron temperature deduced from the shock relations is 30% lower than that measured by electrostatic probes. This discrepancy is considered to arise from the following factors; (1) the shock relation is not exactly correct since the driving plasma slug still has a large effect on the temperature, (2) the probe current due to faster electrons is not negligible.

FIG. 4.15 Single probe electron temperature measurements with 0.1 and 1 mm diameter cylindrical probes. The dotted lines were taken without dummy probes and the solid lines with dummy probes. $z=65$ cm, $V_c=2.5$ KV, $p_1=0.1$ mmHg and $u_2=0.75$ cm/μs.
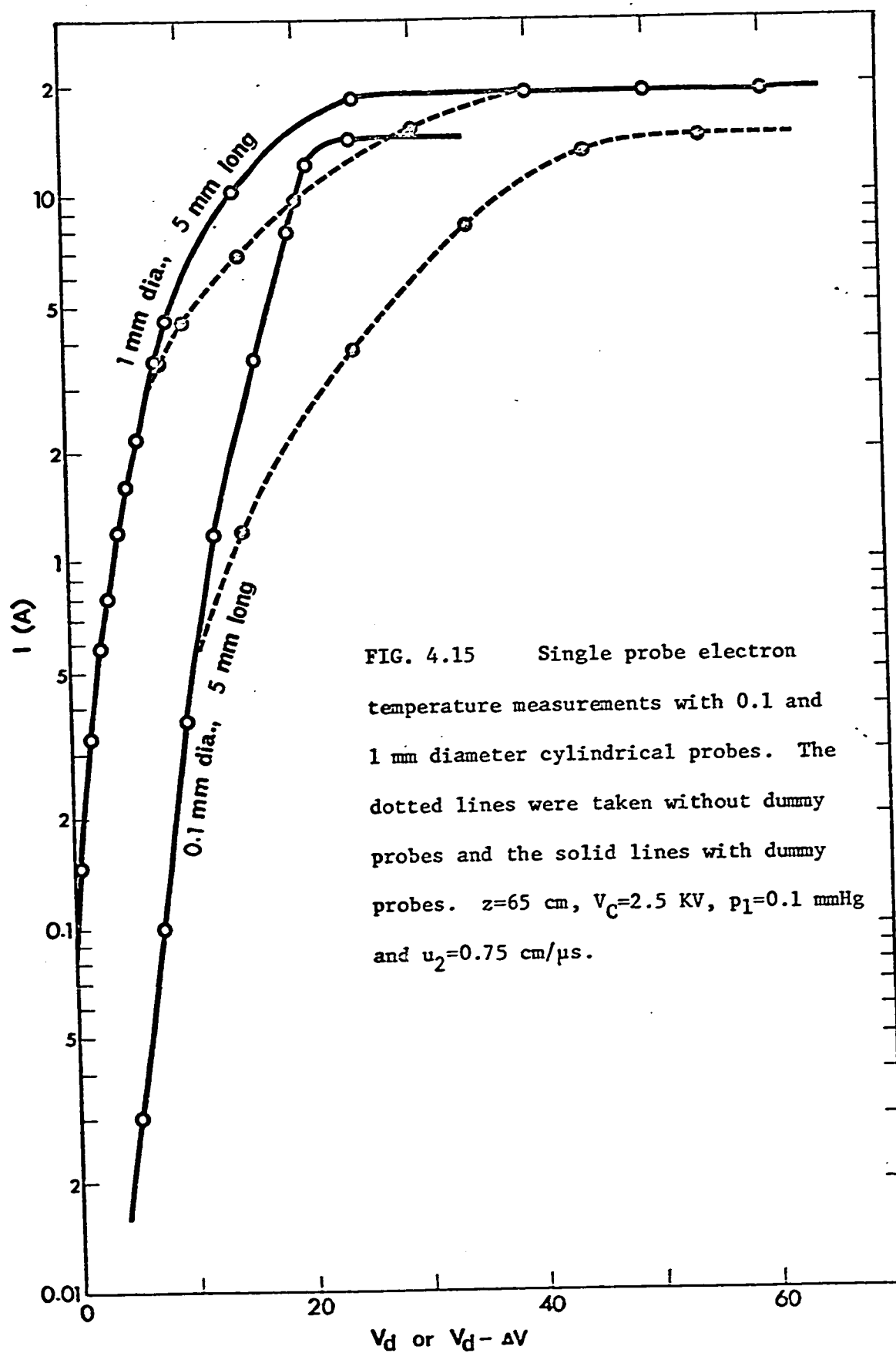
4.3.6 Conductivity Measurements

The plasma conductivity was measured by two methods mentioned previously (two coil method and Lin's method) and the results are listed in Table 4.3. The calculated values of conductivity as well as the plasma temperature from Mach number and Shock relations are also listed. From the table we can find that the conductivity and the temperature can be determined from the shock relations when M is greater than 8. With M less than 8, driver gas rather than the shock heated gas dominates the plasma conditions and so σ and hence T is higher than expected from the shock relations.

4.3.7 Plasma Luminosity Measurements

The pictures of the plasma were taken with the image converter framing camera to study the overall luminosity. Typical pictures are shown in Fig. 4.16 when the initial pressures were 0.1, 1 and 10 mmHg and the driver capacitor bank voltage was 3 KV. From the pictures the following can be deduced:

P_i (mmHg)	z (cm)	M	L_p (cm)	M_1	L_s (cm)	v_{sx} (cm/us)	Re	FIG. 4.16
0.1	30	19	3.4	23.7	5.5	0.2	4000	A
1	30	8.7	3.4	——	——	——	7400	B
10	13	3.4	3.4	——	——	——	20700	C

where L_p is the length of the driving plasma slug, L_s is the length of

case	p_1 (mmHg)	V_C (KV)	z (cm)	$M=u_2/c_1$	σ (mho/m) measured	σ^* (mho/m) shock rel.	T (°K) from σ	T^* (°K) shock rel.	T_e (°K) single probe
1	0.1	2.5	62	23.4	5200	4300	1.6×10^4	1.4×10^4	2.0×10^4
2	0.1	4.0	62	31	5600	5500	2.0×10^4	1.4×10^4	
3	0.1	2.5	92	12.5	2500	2700	1.1×10^4	0.96×10^4	
4	0.1	4.0	92	19.5	4500	4200	1.5×10^4	1.2×10^4	
5	1.0	2.5	92	2.96	500	0	0.58×10^4	0.09×10^4	
6	1.0	4.0	92	9.4	1700	2200	0.86×10^4	0.84×10^4	
7	0.1	4.0	184	9.5	1700	1800	0.86×10^4	0.81×10^4	

TABLE 4.3   Some results on the plasma conductivity and temperature measurements.
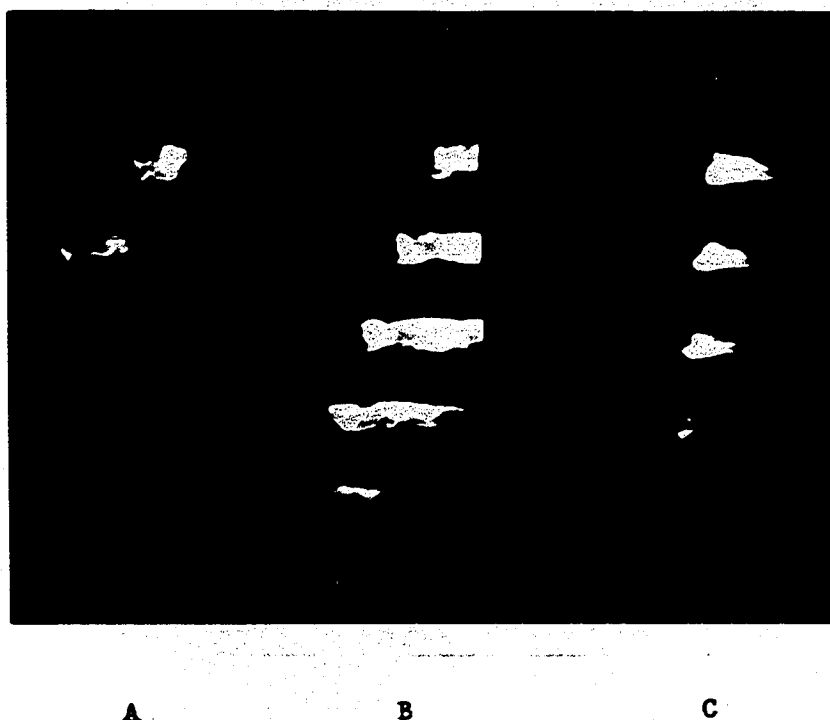
FIG. 4.16   Framing pictures of the plasma produced by the electro-

magnetically driven shock tube. Time increases from top to bottom.

Each picture has an exposure time of 20 ns and the times separating each

consecutive picture are, 10, 12 and 14 µs for A, B and C, respectively.

The plasma proceeds from right to left. The camera sees a length of

18.5 cm of the shock tube. Initial pressures for A, B and C are 0.1,

1 and 10 mmHg. Other experimental conditions are listed in the main

paper.

the shock produced plasma and v_{sx} is the expansion speed of the shock produced plasma. It was also evident that the expansion speed of the driving plasma slug was very small (i.e., L_p was constant), which implies that the snow plough rate, k, of Eq. 4.34 was very small (< 0.1). The shock heated plasma could only be observed at $p_1 = 0.1$ mmHg. The shape of the contact surface/shock front was not always planar.

The length of the driving plasma, L_p, can also be determined from the electrostatic probe signal (or photodiode signal). This was measured with $V_C = 2.5$-4 KV, $p_1 = 0.05$-1 mmHg and $z = 50$-250 cm from the driver. The results also indicated that L_p was independent of V_C, p_1 and z.

CHAPTER V   THEORETICAL CONSIDERATIONS ON THE BREAKDOWN PHENOMENA

5.1   EFFECT OF THE SHEATH SURROUNDING THE ELECTRODE

5.1.1   Floating Potential in the Collision Dominated Plasma

The potential difference across the cathode sheath, V_p, is,

$$V_p = V_d + V_f,$$ (5.1)

where V_d is the voltage applied across two floating electrodes and V_f is the floating potential of the surrounding plasma (Sec. 2.7). Here V_c was assumed to be zero. In an ion sheath around the cathode for our experiments electrons experience no collisions with neutrals at all while ions collide with neutrals. Therefore the floating potential can still be expressed by V_f of Sec. "List of Symbols", i.e.,

$$V_f = \frac{kT_e}{e} \ln \frac{j_e}{j_i},$$ (5.2)

where j_e is the electron random current density expressed by

$$j_e = n_e e \sqrt{\frac{kT_e}{2\pi m_e}}.$$ (5.3)

j_i is the ion saturation current density which can be expressed by Eqs. 2.58, 2.59, 2.63, 2.71, 2.74 or 2.76 depending on the plasma/electrode conditions.

V_f for four important cases will be calculated.

(1) Ions are collision free in the sheath: From Eqs. 5.3, 5.2 and 2.58,

$$V_f = \frac{kT_e}{e} \ln \frac{j_e}{j_i} = 5.3 \frac{kT_e}{e}.$$ (5.4)

(2) Ions are collision dominated in the sheath and the sheath is stationary: From Eqs. 5.2 and 2.63,

$$V_f = 10 \frac{kT_e}{e}. \qquad (5.5)$$

(3) Collision dominated, flowing plasma, $R_E \alpha^2 \chi^2 \ll 1$: From Eqs. 5.2 and 2.71,

$$V_f = 8.8 \frac{kT_e}{e}. \qquad (5.6)$$

(4) Collision dominated, flowing plasma, $R_E \alpha^2 \chi^2 \gg 1$: From Eqs. 5.2 and 2.74,

$$V_f = 6.7 \frac{kT_e}{e}. \qquad (5.7)$$

5.1.2 Ionization of Neutral Particles by Electron Impact

The values of the Townsend first ionization coefficient, α, defined by the relative increase in the electron density per unit length, $dn_e/n_e dr$, can be approximated as (5.1),

$$\frac{\alpha}{p} = A e^{-\frac{Bp}{E}}. \qquad (5.8)$$

The constants A and B can be determined experimentally. For argon, Meek and Craggs (5.2) have given,

$A = 13.6$ (cm^{-1} $mmHg^{-1}$), $\qquad$ $B = 235$ (V/cm·mmHg),

while von Engel (5.3) has given,

$A = 12$ (cm^{-1} $mmHg^{-1}$), $\qquad$ $B = 180$ (V/cm·mmHg),

both for $E/p = 100-600$ (V/cm·mmHg). α is given in cm^{-1}, p in mmHg and E in V/cm. At higher E/p, α is given by (5.4),

E/p (V/cm·mmHg)	500	750	1000	2000	3000
α/p ($cm^{-1}mmHg^{-1}$)	6.29	7.91	9.02	11.24	12.10

The first ionization coefficient is only meaningful when there are

enough elastic collisions between electrons and neutrals so that the

electron mobility can be defined; with the mean free path of electrons

comparable or smaller than the distance between the cathode and sheath

edge (anode), α cannot be defined. In such a case the collisional

phenomenon has to be treated microscopically.

Let us denote the electron energy by k. If, at x=x in a rectangular

coordinate, electrons have an energy distribution of $f(x,k)$, then the

number density of electrons created at $x=x \sim x+dx$ is,

$$dn_e = n_0(x)dx \int_0^\infty f(x,k)Q_i(k)dk,$$ (5.9)

where Q_i is an ionizing collision cross section (which is a function of

electron energy) and n_0 is the neutral particle density at x. Normalization

of $f(x,k)$ can be done by

$$\int_0^\infty f(x,k)dk = n_e(x).$$ (5.10)

The function $f(x,k)$ follows the change of

$$\frac{df}{dx} = \frac{\partial f}{\partial x} + \frac{\partial f}{\partial k}\frac{\partial k}{\partial x} = -n_0 f(x,k)(Q_e + Q_x + Q_i),$$ (5.11)

where Q_e and Q_x are elastic and exciting collision cross sections,

respectively.

For electrons which are emitted from the cathode and reach the

sheath edge without any appreciable collisions, the following assumptions

are valid:

(1) Emitted electrons have small enough energies in comparison with the

(5.1) T. Kihara: Revs. Mod. Phys. 24 45 (1952)
(5.2) J.M. Meek & J.D. Craggs: "Electrical Breakdown of Gases" Oxford, Clarendon Press, pp108 (1953)
(5.3) A. von Engel: "Ionized Gases" Oxford, Clarendon Press, pp 181 (1965) A. von Engel & M. Steenbeck: "Electrische Gasentladungen" Springer, Berlin (1934)
(5.4) T.L.R. Ayres: Phil. Mag. 45 353 (1923) D.Q. Posin: Phys. Rev. 50 650 (1936) M.A. Harrison: Phys. Rev. 105 366 (1957) A. von Engel: "Handbuch der Physik" Springer, Berlin 21 504 (1956)

characteristic voltage of the system so that f(0,k) can be considered to
be a δ-function; i.e., all the electrons are assumed to be emitted from
the cathode at zero initial velocity. (Actual energy distribution of
secondary electrons is shown in (5.21) where it can be seen that the
secondary electron energy at the cathode surface is much smaller than
the ionization potential of argon atoms.)

(2) Electrons experience only few collisions so that

$$\frac{df(x,k)}{dx} = 0.$$
(5.12)

Electrons gain energy from the electric field only, so that $k(x)=eV(x)$.
The velocity of the electrons is then expressed as $v_e(x)=(2eV(x)/m_e)^{\frac{1}{2}}$.
It follows from these assumptions that

$$dn_e = n_0 n_e Q_i(V)dx.$$
(5.13)

In a cylindrical coordinate system, $n_e(x)$ must be considered as a
number of electrons per unit length; i.e., by denoting the number of
electrons per unit length at r as $N_e(r)$,

$$dN_e = n_0 N_e Q_i(V)dr$$
(5.14)

or
$$N_e(r) = N_e(r_p) e^{\int_{r_p}^{r} n_0 Q_i(v) dr}.$$
(5.15)

n_0 is still the number density (in m^{-3}) of the neutral particles.

With the values of E/p and d (interelectrode distance) for the
normal breakdown experiments where α can well be defined,

$$\int_0^d n_0 Q_i dr > \int_0^d \alpha dr,$$
(5.16)

since, in such a case, there are many elastic collisions which reduce
the speed of electrons, i.e., $df(r,k)/dr \neq 0$, and $\int_0^d n_0 Q_i dr$ indicates a
larger value than the true value. However for our experimental conditions
when E/p is very large and d $(=r_s-r_p)$ is very small with the constant
ratio of Ed/p, electrons have to travel a large portion of d to obtain
energy sufficient to ionize the neutrals. Therefore,

$$\int_0^d n_0 Q_i \, dr < \int_0^d \alpha \, dr,$$

(5.17)

and $\int_0^d \alpha \, dr$ is larger than the true value. The crossover point when d=1 mm is approximately E/p=1000 V/cm·mmHg. The value of Q_i for argon as a function of electron energy is shown in Fig. 5.1 (5.5).

5.1.3 BREAKDOWN between Cylindrical Electrodes in Neutral Argon

Before proceeding to the study of electrical breakdown phenomena in a plasma, the breakdown voltage in a neutral gas between infinitely long cylindrical electrodes is investigated. By denoting the distance between the centers of electrodes as d and the radius of both electrodes as r_p, and by taking the x axis as the line connecting the centers of the electrodes and y perpendicular to x, with the origin in the center of one of the electrodes, the potential distribution at P(x,y) can be expressed as,

$$V(x,y) = \frac{V_d}{2} + \frac{V_d}{4 \ln \frac{\sqrt{d+2r_p}+\sqrt{d-2r_p}}{\sqrt{d+2r_p}-\sqrt{d-2r_p}}} \ln \frac{\left(x-\frac{d}{2}+\sqrt{(\frac{d}{2})^2-r_p^2}\right)^2+y^2}{\left(x-\frac{d}{2}-\sqrt{(\frac{d}{2})^2-r_p^2}\right)^2+y^2}$$

(5.18)

where V_d is the potential difference between electrodes. The radial component of the electric field at P has the form, $(r=(x^2+y^2)^{\frac{1}{2}})$,

$$E_r(x,y) = \frac{-V_d}{2 \ln \frac{\sqrt{d+2r_p}+\sqrt{d-2r_p}}{\sqrt{d+2r_p}-\sqrt{d-2r_p}}} \frac{2\sqrt{(\frac{d}{2})^2-r_p^2}}{\sqrt{\left[\left(x-\frac{d}{2}+\sqrt{(\frac{d}{2})^2-r_p^2}\right)^2+y^2\right]\left[\left(x-\frac{d}{2}-\sqrt{(\frac{d}{2})^2-r_p^2}\right)^2+y^2\right]}}$$

(5.19)

If d is sufficiently larger than r_p, x and y, then V and E_r at P can be approximated as,

$$V(r) \approx \frac{V_d}{2 \ln \frac{d}{r_p}} \ln \frac{r}{r_p}$$

(5.20)

_____

(5.5) S.C. Brown: "Basic Data of Plasma Physics" M.I.T. Press (1966)
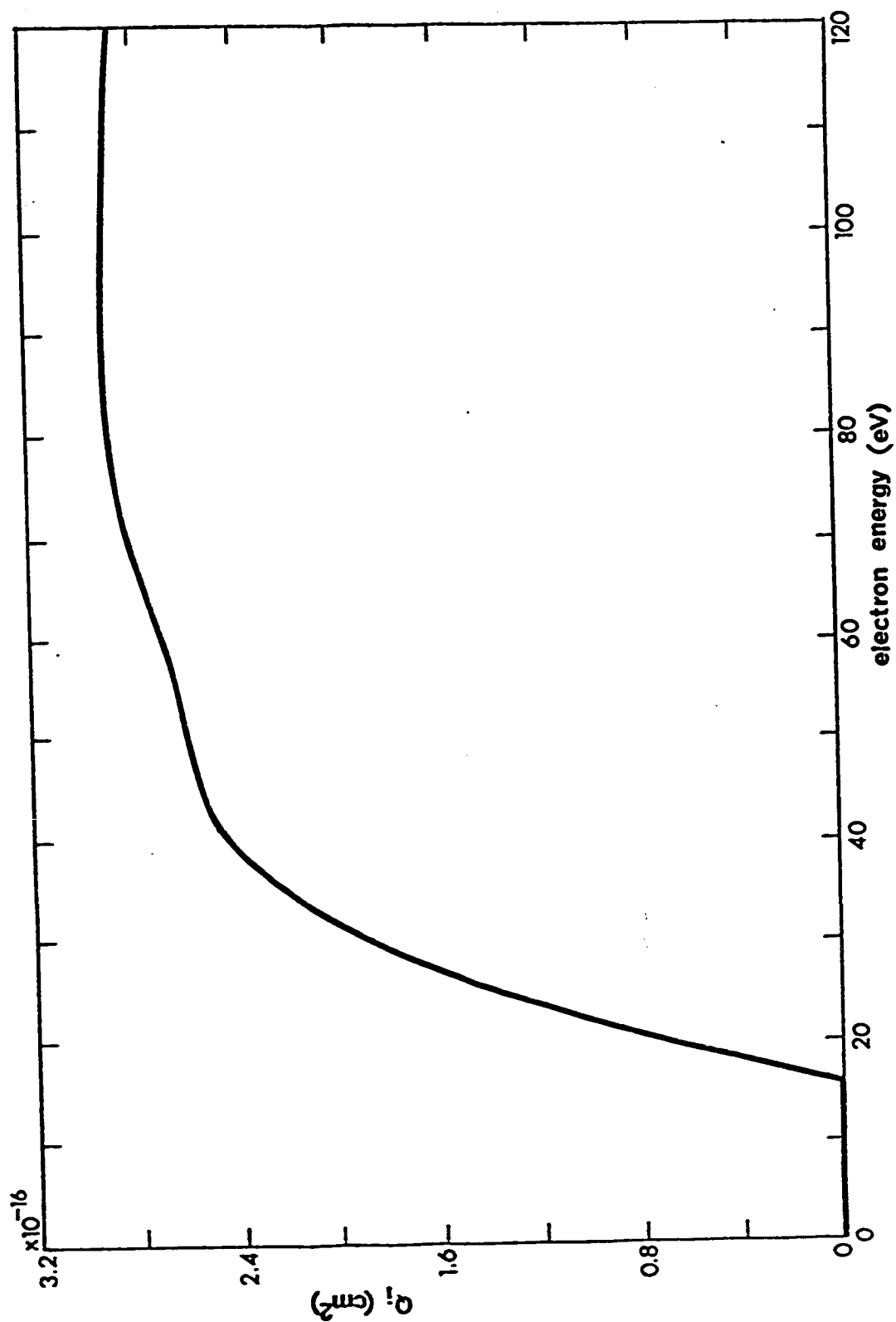
FIG. 5.1   Ionizing collision cross section of argon atoms for electrons

as a function of electron energy (5.5).

and

$$E_r(r) = -\frac{V_d}{2r \ln\frac{d}{r_p}} \cdot$$

(5.21)

The condition of breakdown between two electrodes can be expressed

as,

$$\gamma\left(e^{\int_{r_p}^{d-2r_p} \alpha dr} - 1\right) = 1$$

(5.22)

or

$$\int_{r_p}^{d} \alpha dr \approx \ln\left(1+\frac{1}{\gamma}\right) \equiv \Phi ,$$

(5.23)

where α and γ are the first Townsend ionization coefficient and the rate of secondary electron emission at the cathode per positive ion, respectively. Usually γ is a weak function of the incident ion energy, and so Φ is regarded as a constant. Since the electric field is strong only at small r, the breakdown phenomenon is dominated by the conditions near the cathode and $E(r)$ can be approximated by Eq. 5.21. By denoting the breakdown voltage by V_b, we obtain for the condition of breakdown, from Eqs. 5.8, 5.21 and 5.23,

$$\Phi = \frac{AV_b}{2B \ln\frac{d}{r_p}}\left(e^{-\frac{2Bpr_p \ln\frac{d}{r_p}}{V_b}} - e^{-\frac{2Bpd \ln\frac{d}{r_p}}{V_b}}\right)$$

(5.24)

From Eq. 5.24 the pressure p_m which gives the minimum breakdown voltage, V_m at particular values of d and r_p can be determined. By differentiating V_b with respect to p and putting $dV_b/dp=0$, we have,

$$V_m = \frac{2B\Phi}{A}\frac{\ln\frac{d}{r_p}}{e^{-\frac{\ln(d/r_p)}{(d/r_p)-1}} - e^{-\frac{(d/r_p)\ln(d/r_p)}{(d/r_p)-1}}}$$

(5.25)

and

$$\frac{V_m}{2p_m(d-r_p)} = B \quad (=\text{constant}).$$

(5.26)

By differentiating V_m again with respect to d/r_p, we obtain the absolute minimum breakdown voltage, V_{mm} for any combination of p, d and r_p. This

is given approximately as,

$$V_{mm} = \frac{2B\Phi}{A}e \qquad\qquad (e = 2.718\cdots) \qquad\qquad (5.27)$$

when $d \to r_p$ and $p \to \infty$.

Equation 5.24 can be simplified when p and d are not too small to,

$$\Phi = \frac{AV_b}{2B\ln\frac{d}{r_p}} e^{-\frac{2Bpr_p\ln\frac{d}{r_p}}{V_b}} . \qquad\qquad (5.28)$$

This equation shows that all the data can be reduced to one line if $V_b/\ln(d/r_p)$ is plotted against p. This line corresponds to the well known Paschen curve of V_b vs pd for parallel plate breakdown voltage.

5.1.4 Electric Field at the Electrode Surface in the Sheath

The intensity of the electric field at the electrode surface (E_p) when the electrode is working as an ion collector will be examined. When the electric Reynold's number, R_E (Eq. 2.69), is smaller than one, the sheath around the cylindrical electrode is axially symmetric and E_p can be found by solving,

$$J = 2\pi r n_i(r)ev_i(r) = -2\pi r n_i e\mu_i E(r) \qquad\qquad (5.29)$$

and

$$\nabla^2 V = -\frac{1}{r}\frac{d}{dr}(rE) = -\frac{n_i e}{\varepsilon_o} . \qquad\qquad (5.30)$$

J is the ion current per unit length entering the sheath. From these equations we have,

$$E_p = E_m \sqrt{\left(\frac{r_s}{r_p}\right)^2 - 1} \qquad\qquad (5.31)$$

and

$$V_p = r_s E_m \left[\ln\left(\frac{r_s}{r_p} + \sqrt{\left(\frac{r_s}{r_p}\right)^2 - 1}\right) - \sqrt{1 - \left(\frac{r_s}{r_p}\right)^2}\right] . \qquad\qquad (5.32)$$

where
$$E_m^2 = \frac{J}{2\pi\varepsilon_0\mu_i}.$$
(5.33)

E_p can be found from these two equations by eliminating r_s. In the thin sheath limit E_p can be simplified to,

$$E_p = \left(\frac{3JV_p}{2\pi\varepsilon_0\mu_i r_p}\right)^{\frac{1}{3}},$$
(5.34)

and in the thick sheath limit,

$$E_p = \frac{V_p}{r_p \ln\frac{r_s}{r_p}} \quad \text{and} \quad V_p = r_s E_m \ln\frac{r_s}{r_p}.$$
(5.35)

When the plasma flows perpendicular to the electrode surface with $R_E > 1$, the electric field in the sheath is deformed from a cylindrical to oval shape. However, as long as $\chi = eV_p/kT_e \gg 1$, the direction of the current in the sheath is radial and therefore E_p in Eqs. 5.31, 5.33 and 5.34 is still valid as far as it is considered to be an average value.

The current per unit area at the stagnation point is larger than the average current density by a factor of approximately $2\pi r_s/2r_s = \pi$, and so the E_p at the stagnation point, E_{pmax}, is,

$$\mathcal{E} \equiv \frac{E_{pmax}}{E_p} = \pi^{\frac{1}{3}} = 1.46$$
(5.36)

for the thin sheath limit and

$$\mathcal{E} \equiv \frac{E_{pmax}}{E_p} \approx \frac{1}{1 - \frac{0.57}{\ln\frac{r_s}{r_p}}}$$
(5.37)

for the thick sheath limit.

The exact value of E_{pmax} for the thin sheath and $R_E\alpha^2\chi^2 \gg 1$ can be obtained from Eq. 2.73 as,

$$d(\theta = 0) = \left(\frac{1}{4}\right)^{\frac{1}{2}}\left(\frac{qV^2\mu_i\varepsilon_0 r_p}{4 n_e e u}\right)^{\frac{1}{4}},$$
(5.38)

thus,

$$E_{pmax} = \frac{3V_p}{2d(\theta=0)} = \left(\frac{3^{\frac{5}{4}} V_p J}{4\mu_i \varepsilon_o r_p}\right)^{\frac{1}{3}}$$

(5.39)

or

$$\mathcal{E} = \frac{E_{pmax}}{E_p} = (2.07)^{\frac{1}{3}} = 1.27.$$

(5.40)

5.1.5 Influence of Ionizing Collisions on the Electric Field in the Sheath

When the neutral density in the sheath becomes high, or the potential of the cathode extends far from it, the collisional ionization of neutral particles by secondary electrons emitted from the cathode becomes large and the potential distribution in the sheath has to be modified.

Around the electrode immersed in a plasma flow there is an electric boundary layer in addition to the sheath and hydrodynamic boundary layer. Usually the thicknesses of these boundary layers have the same order of magnitude and are,

$2r_p/\sqrt{R_E}$ for the electric boundary layer, and

$2r_p/\sqrt{Re}$ for the hydrodynamic boundary layer.

Therefore the radial position of the electric boundary layer, r_a, is defined by,

$$r_a = r_p + \frac{2r_p}{\sqrt{R_E}} = r_p + \sqrt{\frac{2r_p kT_e \mu_i}{eu}}.$$

(5.41)

When the sheath is thicker than the electric boundary layer, there is no apparent change in the electric field due to the boundary layer. However, when the sheath becomes thinner than the boundary layer, the situation is different. Most of the electric field is confined

to the sheath region as in the case of the thick sheath although there is a weak field in the region between the sheath and the boundary layer. In this region the densities of ions and electrons are the same so that the particle movement is dominated by ambipolar diffusion; therefore let us call this region an ambipolar diffusion region. All the ionized ions in this region come back to the sheath and affect its potential distribution.

Here we consider the case when $r_a > r_s$. For $r_s < r_a$, all r_a should simply be replaced by r_s. If an ion current per unit length equal to J enters the electric boundary layer, then the number of ions per unit volume at radius r, $n_i^{(0)}$, is,

$$n_i^{(0)}(r) = \frac{J}{2\pi r e v_i(r)} \cdot \tag{5.42}$$

These ions eventually hit the electrode and emit $\gamma J / e$ electrons per second. These secondary electrons, while travelling radially towards the sheath, hit neutral atoms and ionize some of them. For our experimental conditions the thickness of the boundary layer is much smaller than the electron mean free path and the assumptions made in Sec. 5.1.2 are valid. The total number of ions per unit length per second created between $r=r$ and $r+dr$ can be written from Eq. 5.15 as,

$$dN_i = n_0 Q_i \frac{\gamma J}{e} e^{\int_{r_p}^{r} n_0 Q_i dr} dr. \tag{5.43}$$

These newly created ions begin to travel radially towards the cathode. The total number of these secondary ions per unit length per second passing through $r=r$ is $\int_r^{r_a} dN_i$, therefore the secondary ion density at r is,

$$n_i^{(1)}(r) = \frac{1}{2\pi r v_i} \int_r^{r_a} dN_i = \frac{\gamma J}{2\pi r e v_i} \int_r^{r_a} n_0 Q_i e^{\int_{r_p}^{r} n_0 Q_i dr} dr, \tag{5.44}$$

or, at the electrode surface,

$$n_i^{(1)}(r_p) = \frac{JG}{2\pi r_p e \, v_i(r_p)} \; , \tag{5.45}$$

where

$$G \equiv \gamma \int_{r_p}^{r_a} n_o Q_i \, e^{\int_{r_p}^{r} n_o Q_i \, dr} \, dr. \tag{5.46}$$

These ions again hit the electrode surface and emit $\gamma 2\pi r_p n_i^{(1)}(r_p) v_i(r_p)$ $=\gamma JG/e$ electrons per second, which happens to be G times the initially emitted electrons. These electrons ionize neutrals, and repeat the same procedure again. Finally the total amount of ions hitting the electrode is,

$$\frac{J}{e}(1 + G + G^2 + \cdots) = \frac{J}{e(1-G)} \; , \tag{5.47}$$

and the total ion density at r is,

$$n_i(r) = \frac{J}{2\pi r e \, v_i(1-G)} \left(1 - \gamma \int_{r_p}^{r} n_o Q_i \, e^{\int_{r_p}^{r} n_o Q_i \, dr} \, dr\right). \tag{5.48}$$

Before solving Poisson's equation we express the ion velocity in the sheath by $v_i(r) = |\mu_i E(r)| = -\mu_i E(r)$ (E$\leq$0). Then,

$$\nabla^2 V = -\frac{1}{r}\frac{d}{dE}(rE) = -\frac{n_i e}{\varepsilon_o} = \frac{E_m^2}{rE(1-G)}\left(1 - \gamma \int_{r_p}^{r} n_o Q_i \, e^{\int_{r_p}^{r} n_o Q_i \, dr} \, dr\right) \tag{5.49}$$

where

$$E_m^2 \equiv \frac{J}{2\pi \varepsilon_o \mu_i} \; . \tag{5.50}$$

The contribution of the electrons to the field is neglected because of their large mobility. By integrating from r=r (E=E, V=V) to r=r$_s$ (E=0, V=0) (5.6), we obtain,

$$E(r)^2 = \frac{2}{(1-G)r^2}\int_r^{r_s} r E_m^2 \, dr - \frac{2\gamma}{(1-G)r^2}\int_r^{r_s} r E_m^2 \left[\int_{r_p}^{r} n_o Q_i \, e^{\int_{r_p}^{r} n_o Q_i \, dr} \, dr\right] dr, \tag{5.51}$$

(5.6) This assumption of E=0 and V=0 at the sheath edge was shown to be reasonable when $eV_p/kT_e \gg 1$ by Schulz and Brown (2.14).

$$E_p = |E(r_p)| = \left[\frac{2}{(1-G)r_p^2}\int_{r_p}^{r_s}rE_m^2\,dr - \frac{2\gamma}{(1-G)r_p^2}\int_{r_p}^{r_s}rE_m^2\left\{\int_{r_p}^{r}n_oQ_i e^{\int_{r_p}^{r}n_oQ_i\,dr}\,dr\right\}dr\right]^{\frac{1}{2}} \qquad (5.52)$$

and

$$V_p = |V(r_p)| = -\int_{r_p}^{r_s}E(r)\,dr\ . \qquad (5.53)$$

Since the exact solution of these equations is difficult obtain, we study two limiting cases depending on the values of r_a and r_s.

(1) $r_s \gg r_a$: In this case the neutral density is approximately equal to n_2 (suffix 2 indicates the quantity in the incident shock). As V_p is large (much larger than V_i, the ionization potential of the gas) for the thick sheath case, Q_i can be considered to be constant throughout the sheath (Fig. 5.1) and

$$\int_{r_p}^{r}n_oQ_i\,dr = n_2Q_i(r-r_p)\ , \qquad (5.54)$$

where $Q_i = 2.8\times10^{-20}$ m^2. E_m also takes the constant value of E_{m2} $(\mu_i = \mu_{i2})$. Therefore

$$G = \gamma\left(e^{n_2Q_i(r_s-r_p)}-1\right) \qquad (5.55)$$

$$E_p = \frac{E_{m2}}{\sqrt{1-G}}\left[\frac{(1+\gamma)(r_s^2-r_p^2)}{r_p^2} + \frac{2\gamma(1-n_2Q_i r_s)}{(n_2Q_i r_p)^2}e^{n_2Q_i(r_s-r_p)} - \frac{2\gamma(1-n_2Q_i r_p)}{(n_2Q_i r_p)^2}\right]^{\frac{1}{2}} \qquad (5.56)$$

$$V_p = \frac{E_{m2}}{\sqrt{1-G}}\int_{r_p}^{r_s}\left[\frac{(1+\gamma)(r_s^2-r^2)}{r_p^2} + \frac{2\gamma(1-n_2Q_i r_s)}{(n_2Q_i r)^2}e^{n_2Q_i(r_s-r_p)} - \frac{2\gamma(1-n_2Q_i r)}{(n_2Q_i r)^2}e^{n_2Q_i(r-r_p)}\right]^{\frac{1}{2}}dr \qquad (5.57)$$

$G=1$ is the spark discharge breakdown condition. E_p, V_p and r_s are computed with various neutral densities and the results presented by the thinner lines in Fig. 5.2 in terms of normalized quantities, E_p/E_{m2}, V_p/r_pE_{m2} and $d/r_p=(r_s/r_p)-1$. (The notation n_2 is changed to n_W in the graph, as this graph can also be used for the case of $r_a \gg r_s$.) r_s has the limiting value of,

FIG. 5.2   The thinner lines show the relation of the reduced E_p, V_p and d at various values of n_w/n_0 (Eqs. 5.55-5.57), where $n_0=3.22\times10^{22}$ m^{-3} is the neutral density at 1 mmHg and 0°C. The upper half of the graph shows E_p/E_m, while the lower half shows d/r_p. The thicker lines are the extreme cases when $n_w=0$ or when the ionization effect in the sheath is negligible (Eqs. 5.63 and 5.64).

$\dfrac{E_p}{E_m}$

$\dfrac{E_p}{E_m}, \dfrac{d}{r_p}$

$\dfrac{V_p}{r_p E_m}$

$\dfrac{n_w}{n_0} =$

10
5
3
2

5
10
20
50
100
200
500
1000
2000
5000
10000

$\dfrac{d}{r_p}$

$\dfrac{n_w}{n_0} =$

$\dfrac{d}{r_p}$

$\dfrac{E_p}{E_m}$

10
20
50
100
200
500
1000
2000
5000
10000

FIG. 5.2 - cont'd.

$$r_s = r_p + \frac{1}{n_2 Q_i} \ln\left(1 + \frac{1}{\gamma}\right).$$

(5.58)

When r_s is sufficiently close to the value, the ratio of E_p/E_{m2} and $V_p/r_p E_{m2}$ becomes constant.

(2) $r_a \gg r_s$: The neutral density is now a function of r, as seen from Eqs. 5.106 and 5.107,

$$n(r) = \frac{1.3\, n_s \left(\frac{T_s}{T_0}\right)(r_a - r_p)}{\left(\frac{T_s}{T_0} - 1\right) r - \left(r_p \frac{T_s}{T_0} - r_a\right)}.$$

(5.59)

Since the electric field outside the sheath is very weak, all the electrons in the ambipolar diffusion region can be considered to have an energy of eV_p. Thus the ionizing cross section takes a constant value $Q_i(V_p)$ and G of Eq. 5.46 can be calculated as,

$$G = \gamma \int_{r_p}^{r_s} + \gamma \int_{r_s}^{r_a} \simeq \gamma \int_{r_p}^{r_s} + \gamma \int_{r_p}^{r_a} \equiv G_s + G_a,$$

(5.60)

where

$$G_s = \gamma \left(e^{n_w Q_i (r_s - r_p)} - 1 \right)$$

(5.61)

and

$$G_a = \gamma Q_i \int_{r_p}^{r_a} n(r)\, e^{Q_i \int_{r_p}^{r} n\, dr}\, dr = \gamma \left[\left(1.3 \frac{T_s}{T_0}\right)^{1.3 n_s Q_i (r_a - r_p)} - 1 \right]$$

$$= \gamma \cdot 1.3\, n_s Q_i (r_a - r_p) \ln\left(1.3 \frac{T_s}{T_0}\right).$$

(5.62)

In the sheath the neutral particle density is considered to be a constant, n_w (suffix w indicates the quantity at very near the electrode surface). Therefore Eqs. 5.52 and 5.53 can be reduced to Eqs. 5.56 and 5.57, with the exceptions that

suffix 2 is changed to suffix w, and

G is changed to $G_s + G_a$.

When the sheath is thin or the neutral density is low enough, the ionizing effect in the sheath can be neglected and we have, from Eqs. 5.52 and 5.53,

$$E_p = \frac{E_{mw}}{\sqrt{1-G_a}} \sqrt{\left(\frac{r_s}{r_p}\right)^2 - 1} \qquad (5.63)$$

and

$$V_p = \frac{r_s E_{mw}}{\sqrt{1-G_a}} \left[\ln\left(\frac{r_s}{r_p} + \sqrt{\left(\frac{r_s}{r_p}\right)^2 - 1}\right) - \sqrt{1 - \left(\frac{r_p}{r_s}\right)^2} \right] \qquad (5.64)$$

The graph of E_p/E_{mw} and d/r_p against $V_p/r_p E_{mw}$ is shown by the thicker lines in Fig. 5.2. (The $(1-G_a)^{\frac{1}{2}}$ term is included in E_{mw} in the graph, since the ionization effect in the ambipolar diffusion region can be interpreted as if J is increased to $J/1-G_a$.)

Especially when r_s is very thin, the above equations can further be simplified to,

$$E_p = \frac{E_{mw}}{\sqrt{1-G_a}} \sqrt{\frac{2d}{r_p}} = \frac{3}{2} \frac{V_p}{d} = \left(\frac{3JV_p}{2\pi \varepsilon_0 \mu_{iw} r_p (1-G_a)}\right)^{\frac{1}{3}} \qquad (5.65)$$

and

$$V_p = \frac{E_{mw}}{\sqrt{1-G_a}} \sqrt{\frac{8d^3}{9r_p}} = \left(\frac{4Jd^3}{9\pi \varepsilon_0 \mu_{iw} r_p (1-G_a)}\right)^{\frac{1}{2}} \qquad (5.66)$$

5.1.6 Secondary Ions Returning to Cathode from Outside the Sheath/Ambipolar Diffusion Region

Secondary electrons emitted from the cathode gain an energy of about eV_p at the sheath edge. As they leave the sheath they ionize neutrals for $(V_p-V_i)/V_i$ times. Since there is no electric field outside the sheath, these newly ionized ions diffuse away isotropically, and θ/π fraction of these ions happen to fall into the cathode sheath, where $\theta = \sin^{-1}(r_s/(r_p+\lambda_{e2}))$. The total number of secondary ions returning to the cathode per electron, ζ, is thus,

$$\zeta = \left(\frac{V_p}{V_i} - 1\right) \frac{\theta}{\pi}. \qquad (5.67)$$

Effective ion current to the cathode is therefore increased to,

$$J \longrightarrow \frac{1}{1-\eta\varsigma} J \; , \tag{5.68}$$

where γ is the secondary electron emission coefficient at the cathode

surface per incident ion.

5.1.7 Double Sheath Formation on the Cathode

If the cathode emits electrons, the potential distribution is

modified by the space charge effect created by them, especially near

the cathode where electrons have rather slow velocities. This modification

will be discussed quantitatively for a collisionless sheath below (5.7).

Consider an infinite plane cathode at $-V_p$ (<0) and a sheath edge at

zero potential at a distance d from the cathode. At the sheath edge

there will be a zero potential gradient and a finite ion current j_i per

unit area. When there is no electron emission from the cathode, j_i can be

expressed by (Eq. 2.44),

$$j_i = \frac{4\sqrt{2}\varepsilon_0}{9} \sqrt{\frac{e}{m_i}} \frac{V_p^{\frac{3}{2}}}{d_0^2} \; , \tag{5.69}$$

where d_0 is the sheath thickness when the electron emission from the

cathode is zero. Let v_e be the velocity of the electrons at any point

P which is at a distance x from the sheath edge, n_e the electron density

at P. The corresponding quantities for the positive ions are denoted by

the subscript i. Then,

$$j_e = n_e e v_e, \quad j_i = n_i e v_i \tag{5.70}$$

and assuming the ions have unit charge,

$$\tfrac{1}{2} m_e v_e^2 = e(V_p + V), \quad \tfrac{1}{2} m_i v_i^2 = -eV, \tag{5.71}$$

where V (≤ 0) is the potential at the point P. Poisson's equation gives,

$$\frac{d^2V}{dx^2} = -\frac{e(n_i - n_e)}{\varepsilon_0} \quad . \tag{5.72}$$

We may eliminate n and v and then after substituting

$$\alpha = \frac{j_e}{j_i}\left(\frac{m_e}{m_i}\right)^{\frac{1}{2}}, \qquad \phi = -\frac{V}{V_p} \quad \text{and} \quad \lambda = \frac{x}{d}, \tag{5.73}$$

we obtain,

$$\frac{d^2\phi}{d\lambda^2} = \frac{4}{9}\frac{d^2}{d_0^2}\left(\frac{1}{\sqrt{\phi}} - \frac{\alpha}{\sqrt{1-\phi}}\right)^{\frac{1}{2}}. \tag{5.74}$$

Since the ion current is limited by space charge, we impose the condition

dV/dx=0 at x=0. Integration then gives,

$$\frac{d\phi}{d\lambda} = \frac{4}{3}\frac{d}{d_0}\left(\sqrt{\phi} + \alpha(\sqrt{1-\phi} - 1)\right)^{\frac{1}{2}}. \tag{5.75}$$

The ratio d/d_0 is found by observing that $V=-V_p$ at x=d, thus,

$$\frac{d}{d_0} = \frac{3}{4}\int_0^1\left(\sqrt{\phi} + \alpha(\sqrt{1-\phi} - 1)\right)^{-\frac{1}{2}}d\phi. \tag{5.76}$$

The effect of electrons from the cathode in neutralizing the ion space

charge cannot cause an increase in j_i for this is fixed by the plasma,

but manifests itself by changing the sheath thickness as expressed in the

equation above.

According to Eq. 5.75 the potential gradient at the surface of the

cathode is proportional to $(1-\alpha)^{\frac{1}{2}}$ and so $0 \leq \alpha \leq 1$. When $\alpha=1$ the potential

gradient at the cathode is zero and the electron current as well as the

positive ion current is thus limited by space charge. Maximum electron

current is, therefore, expressed by

$$j_{emax} = j_i\left(\frac{m_i}{m_e}\right)^{\frac{1}{2}}, \tag{5.77}$$

and in such a case the curve representing the potential distribution in

the sheath is symmetrical about its central point.

(5.7) I. Langmuir: Phys. Rev. **33** 954 (1929)
       F.W. Crawford & A.B. Cannara: J. Appl. Phys. **36** 3135 (1965)

The intensity reduction ratio, $\mathcal{E}$, of the electric field at the cathode surface by electron emission from the cathode is,

$$\mathcal{E} = \frac{\frac{d\phi}{d\lambda}}{\left[\frac{d\phi}{d\lambda}\right]_{\alpha=0}} = \frac{3}{4}(1-\alpha)^{\frac{1}{2}}\int_0^1 \left(\sqrt{\phi}+\alpha(\sqrt{1-\phi}-1)\right)^{-\frac{1}{2}}d\phi. \qquad (5.78)$$

The numerically obtained plot of $\mathcal{E}$ and d/d_0 against α is shown in Fig. 5.3.

There will not be any noticeable change in electric field at the cathode surface unless $\alpha > 0.1$, or in the case of argon plasma, $j_e > 30\, j_i$. If emission of secondary electrons is due to ion bombardment, then $j_e = 0.1 j_i$ and the double sheath effect can be completely neglected. However, for breakdown due to the electron field emission, this condition appears to be quite severe for low density plasmas with a small cathode ($I_i < 10$ mA).

For an argon plasma, the electron mean free path is much longer than the ion mean free path. In our normal experimental conditions ions are collision dominated in the sheath, but not electrons. In such a case ionic charge contributes to the electric field more than in the collisionless case, and tends to approach unity and again the double sheath effect on the cathode electric field is negligible.

5.1.8 Ion-Electron Collision in the Sheath

Since electrons are emitted from the electrode which is in a positive sheath, electrons may experience collisions not only with neutral particles but with ions. In this section the collisional effect between electrons and ions is considered. Average momentum transfer collision frequency can be calculated by using Eq. 2.6 for ν_m and Eq. 5.115 for electron velocity distribution function, as,

FIG. 5.3   The variation of the sheath thickness and electric
field at the cathode surface due to double sheath formation as
a function of ion and electron current densities (j_i and j_e) to
and from the cathode.
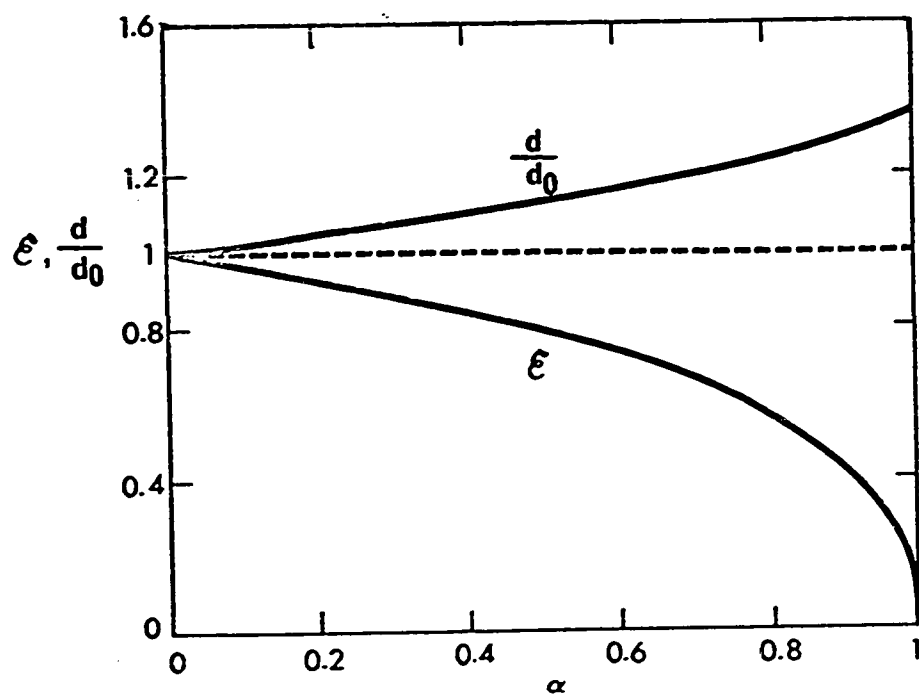
$$\overline{\nu}_m = \frac{1}{\int_0^\infty f(v)dv} \int_0^\infty \nu_m(v) f(v) dv = \frac{(2.61\times10^{-12})^{\frac{3}{2}} n_i Z^2 e^4 \ln\Lambda}{4\sqrt{\pi}\, \varepsilon_0^2 m_e^2} = 6.03\times10^{-12} n_i Z^2 \ln\Lambda . \quad (5.79)$$

This equation is valid only when the drift velocity of electrons can be neglected. For a non-Maxwellian gas, Λ of Eq. 2.7 takes a different form (the concept of temperature cannot be used). However as it is a logarithmic term, the result has only a small error. Electron mobility in the ion sheath is, from Boltzmann equation,

$$\mu = \frac{1}{\int_0^\infty f(v)dv} \int_0^\infty \frac{ev}{m_e \nu_m} \frac{\partial f}{\partial v} dv = \frac{30\pi^{\frac{3}{2}} \varepsilon_0^2 m_e}{n_i Z^2 e^3 (2.61\times10^{-12})^{3/2}} \ln\Lambda = \frac{6.81\times10^{23}}{n_i Z^2 \ln\Lambda} . \quad (5.80)$$

(If we assume a Maxwellian distribution with $T_e = 2$ eV, then we have,

$\mu = 5.85\times10^{23}/n_i Z^2 \ln\Lambda$.)

In the case where the sheath has an extremely high electric field, the concepts of $\overline{\nu}_m$ and μ cannot be applied. This is proved as follows. Let us consider an electron leaving the electrode at initial velocity of v_0. Before it collides with an ion for the first time at t_1, it keeps increasing in velocity as,

$$v = v_0 + \frac{eE}{m} t. \quad (5.81)$$

At $t = t_1$, the probability of collision with an ion becomes unity, so that we have $\int_0^{t_1} \nu_m dt = 1$. By solving the equation using Eq. 2.6, it is found that,

$$t_1 = \frac{m v_0}{eE} \left(\frac{1}{\sqrt{1 - \frac{8\pi \varepsilon_0^2 m_e E v_0^2}{n_i Z^2 e^3 \ln\Lambda}}} - 1 \right). \quad (5.82)$$

For t_1 to exist, the term in the square root must be positive, i.e.,

$$\frac{E v_0^2}{n_i} \leq 1.35\times10^{-5}.$$

In our typical conditions where $E = 2\times10^6$ V/m and $v_0 = 1$ eV (both underestimated),

$$n_i \geq 5\times10^{22}\ m^{-3},$$

which is out of our experimental range. Thus, all the electrons ejected

from the electrode "run away" and suffer no collisions with ions.

In an actual case the electrons cannot acquire infinite velocity, since they are decelerated by collisions with neutrals. Again, by choosing underestimated values such that μ_e (electron-neutral)=4 m^2/V·sec (at 100 mmHg) and E=2x10^6 V/m, the electron-ion collision frequency becomes 0.94x10^7 sec^{-1}. An electron proceeds, between each collision with an ion, $\mu_e E/\nu_m$=0.8 meters, which is many orders of magnitude larger than the sheath thickness; i.e., the electron runs away again.

5.1.9 Current Pinching Effect

When there is a current through a plasma, the plasma may be pinched by the magnetic pressure produced by the current (z-pinch). The strength of this force can be expressed by the ratio (β) of the plasma pressure which acts against the pinching force, and the magnetic pressure,

$$\beta \approx \frac{c(n_i+n_e)kT}{\frac{B^2}{2\mu_0}} = \frac{8\pi^2 R^2 (n_e+n_i)kT}{\mu_0 I^2} \quad , \tag{5.83}$$

where c is the compression ratio of the plasma density. This ratio can be defined as R^2/r^2, where R and r are the initial and final radii of the plasma column. The values of the plasma properties which yield the smallest β are, in our experimental conditions, R=10^{-4}m(=diameter of the electrode), T=10^4, n_e=10^{16} m^{-3} and I=0.01 A with β=10, i.e., the magnetic pressure is not strong enough to pinch the plasma column. Therefore the pinching force acting on the current is always negligible. Current pinching can only be formed in the presence of some other mechanism, e.g., local heating, non-uniform insulating surface layer, local breakdown of surface layer.

5.2 IONIC MOBILITY NEAR THE ELECTRODE

5.2.1 Mobility of Ar^+ in the Parent Gas

The mobility of the argon ion at room temperature has been measured by many people (5.8) and the value is consistently 1.6 $cm^2/V \cdot sec$ at 760 mmHg, 0°C or,

$$\mu_i = 0.12 \ m^2/V \cdot sec \qquad \text{at 1 mmHg and °0 C.} \qquad (5.84)$$

Theoretical calculations of argon mobility (5.9) support this result well. Unfortunately ionic mobility at high temperature has not been measured except for NO^+ in air (5.10), where it has been found that the mobility decreases with increasing temperature slowly (slower than $T^{-\frac{1}{2}}$). Mobility is strictly inversely proportional to neutral density.

In our calculations, the ionic version of Eq. 2.3,

$$\mu_i \approx 0.12 \times \frac{3.38 \times 10^{22}}{n_o \ (m^{-3})} \sqrt{\frac{300}{T_i \ (°K)}} \qquad (m^2/V \cdot sec) \qquad (5.85)$$

will be used for the mobility at high temperature. When calculating the electric field at the electrode surface from Eqs. 5.34, 5.66, etc., E_p is approximately proportional to $\mu_i^{1/3}$ or $T_i^{1/6}$, i.e., E_p is almost independent of T_i. Therefore the approximation of Eq. 5.85 is quite reasonable.

(5.8) R.M.J. Munson & A.M. Tyndall: Proc. Roy. Soc. A117 187 (1940)
       M.A.J.A. Hornbeck: Phys. Rev. 84 615 (1951)
       M.A. Biondi & L.M. Chanin: Phys. Rev. 94 910 (1954)
(5.9) H.R. Hasse & W.R. Cook: Phil. Mag. 12 554 (1931)
       T. Holstein: J. Phys. Chem. 56 832 (1952)
       E.A. Mason & H.W. Schamp, Jr.: Annals of Phys. 4 233 (1958)
(5.10) J.K. Dukowitz: AIAA Journal 8 827 (1970)

5.2.2 Stagnated Shock Wave

In the previous sections it was found that the knowledge of neutral density is of vital importance in the evaluation of mobility and hence E_p. When an electrode is surrounded by a hypersonic plasma flow, a stationary shock wave is formed around the electrode as seen in Fig. 5.4. If we denote two regions which are separated by the shock wave as 2 and 5, as in the figure, then the gas in the region 5 is stagnated by the electrode, which results in a further increase in the temperature, pressure and density of the gas. It is more convenient to derive these quantities in the stagnated shock region in terms of the conditions in the incident gas, rather than in terms of the initial conditions where the gas is stationary. The properties thus derived may then be related to the initial conditions by way of Mach number.

For an ideal gas with constant specific heats, the continuity, momentum and energy equations relating the flow variables on both sides of a shock wave can be written as (5.11),

$$\rho_2 u_{2n} = \rho_5 u_{5n}$$
$$P_2 + \rho_2 u_{2n}^2 = P_5 + \rho_5 u_{5n}^2 \tag{5.86}$$
$$\text{and} \quad \frac{\gamma}{\gamma-1} \frac{P_2}{\rho_2} + \frac{u_2^2}{2} = \frac{\gamma}{\gamma-1} \frac{P_5}{\rho_5} + \frac{u_5^2}{2},$$

by using the notation introduced in Fig. 5.4. We can write also,

$$u_{2n} = u_2 \sin \xi$$
$$u_{2t} = u_2 \cos \xi$$
$$u_{5n} = u_5 \sin(\xi - \delta) \tag{5.87}$$
$$u_{5t} = u_5 \cos(\xi - \delta).$$

(5.11)   J.A. Owczarek: "Fundamentals of Gas Dynamics" Int'l Textbook Co., pp549 (1964)

FIG. 5.4 The formation of a stagnated shock wave around the stationary cylindrical electrode.
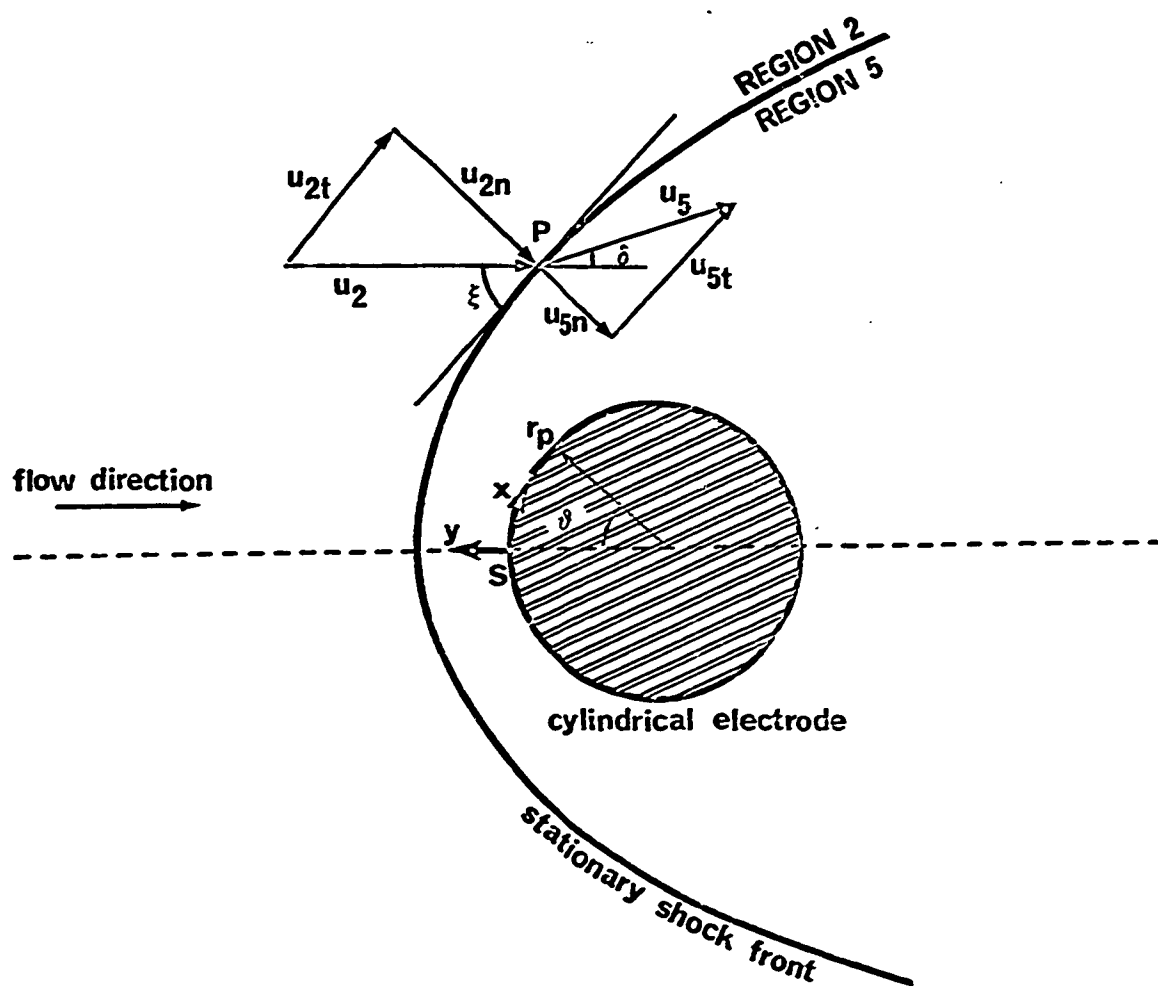
The angle ξ can take values between $90°$ and $\sin^{-1}(1/M_2)$. By solving these equations we obtain,

$$\frac{\rho_5}{\rho_2} = \frac{\gamma+1}{\gamma-1+\frac{2}{(M_2\sin\xi)^2}} \tag{5.88}$$

$$\frac{P_5}{P_2} = 1 + \frac{2\gamma}{\gamma+1}\left[(M_2\sin\xi)^2 - 1\right] \tag{5.89}$$

$$\frac{T_5}{T_2} = 1 + \frac{2(\gamma-1)}{(\gamma+1)^2}\left[(M_2\sin\xi)^2 - 1\right]\left[\gamma + \frac{1}{(M_2\sin\xi)^2}\right] \tag{5.90}$$

$$M_5^2 = \frac{(M_2\sin\xi)^2 + \frac{2}{\gamma-1}}{\frac{2\gamma}{\gamma-1}(M_2\sin\xi)^2 - 1}\left[\left(\frac{\frac{\gamma+1}{\gamma-1}(M_2\sin\xi)^2\cot\xi}{(M_2\sin\xi)^2 + \frac{2}{\gamma-1}}\right)^2 + 1\right], \tag{5.91}$$

where
$$M_2 = \frac{u_2}{c_2}. \tag{5.92}$$

ρ_5, P_5 and T_5 take their maximum values at $\xi=90°$, when the above equations are reduced to Eqs. 4.15, 4.16 and 4.17 if the subscripts 1 and 2 are changed into 2 and 5, respectively and M_1 into M_2.

There is a limiting value for M_2. From Eq. 4.15-4.18,

$$M_2 = \frac{2(M_1^2-1)}{\sqrt{((\gamma-1)M_1^2+2)(2\gamma M_1^2-(\gamma-1))}} < \frac{2}{\sqrt{2\gamma(\gamma-1)}}. \tag{5.93}$$

For argon plasma with $M_1 > 5$ and $\xi=90°$, M_2 reaches the limiting value of $3/\sqrt{5}$, with

$$\frac{\rho_5}{\rho_2} = 1.5, \quad \frac{P_5}{P_2} = 2, \quad \frac{T_5}{T_2} = \frac{4}{3}, \quad M_5 = \frac{3}{5} \quad \frac{u_5}{c_2} = \frac{2\sqrt{3}}{5}. \tag{5.94}$$

In Eq. 5.86 it was assumed that further ionization in the stagnated shock was negligible, since the relaxation time for argon gas in the stagnated shock is much longer than $r_p/\bar{v}$, the time spent by particles to pass by the electrode.

5.2.3 Neutral Particle Density in a Boundary Layer

A cylindrical obstacle in a gas flow has a surrounding boundary layer. If we choose the coordinate system as in Fig. 5.4 (x direction coincides with the surface of the electrode and y direction with the normal direction of the surface), then the gas has no motion at the point x=y=0, which is called stagnation point.

By using this coordinate system the temperature, pressure and the density distributions in the boundary layer can be found by solving the Navier-Stokes equations. In this section we shall examine these distributions on the y axis only (x=0, d/dx=0), i.e., examine the flow of normal incidence to the object. The following notations will be used:

u = particle velocity with respect to the obstacle

η = viscosity (shear viscosity, $\propto T^{\frac{1}{2}}$)

$\nu = \eta/\rho$ = kinematic viscosity

$\delta = L/\sqrt{Re}$ = thickness of velocity boundary layer

$\delta_T = \sqrt{kL/c_p \rho u}$ = thickness of thermal boundary layer

L = characteristic length such as electrode diameter

k = thermal conductivity

$c_p = \gamma k/(\gamma-1)m$ = constant pressure specific heat

$Re = uL/\nu$ = Reynold's number

$Pr = c_p \eta/k$ = Prandtl number (independent of temperature, Pr=0.67 for Ar).

Firstly, the flow velocity change along the y axis is expressed as,

$$u = -\sqrt{a\nu}\ \phi(\zeta) , \tag{5.95}$$

where $\phi(\zeta)$ is the solution of the differential equation,

$$\phi''' + \phi\phi'' - \phi'^2 + 1 = 0 , \tag{5.96}$$

and $\zeta = \sqrt{a/\nu}\, y$ where a is a constant. This equation was solved numerically by Howarth (5.12) and the results shown in Fig. 5.5. If y is large or viscosity is small, u can be approximated simply as,

$$u = -ay. \tag{5.97}$$

The displacement thickness, δ_1, is,

$$\delta_1 = 0.648\sqrt{\frac{\nu}{a}}. \tag{5.98}$$

The temperature distribution in the boundary layer around the adiabatic wall is found to be (5.13),

$$\frac{T}{T_\infty} = 1 + \frac{\sqrt{P_r}}{2c_p T_\infty}(u_\infty^2 - u^2) = 1 + \sqrt{P_r}\,\frac{\gamma-1}{2}M^2\left(1 - \frac{u^2}{u_\infty^2}\right). \tag{5.99}$$

The subscript ∞ expresses the quantity at the place where the stagnation effect is negligible. If the wall is heat conducting, then by introducing T_w, the wall temperature,

$$\frac{T}{T_\infty} = \frac{T_w}{T_\infty} + \left(1 - \frac{T_w}{T_\infty}\right)\frac{u}{u_\infty} + \sqrt{P_r}\,\frac{\gamma-1}{2}M^2\frac{u}{u_\infty}\left(1 - \frac{u}{u_\infty}\right). \tag{5.100}$$

This T(u) curve has the shape of Fig. 5.6. With these values of u and T the pressure can be determined from the Navier-Stokes equation. Especially for the pressure on y axis,

$$\frac{dp}{dy} = -\rho u \frac{\partial u}{\partial y} + \frac{\partial}{\partial y}\left(\eta \frac{\partial u}{\partial y}\right). \tag{5.101}$$

The approximate solution to this equation is,

$$P_\infty + \frac{1}{2}\rho_\infty u_\infty^2 = P + \frac{1}{2}\rho u^2 = P\left(1 + \frac{1}{2}\gamma M^2\right). \tag{5.102}$$

(This equation is valid for a cylindrical coordinate system, too.) For the stagnation point, we have,

$$P_s = P_\infty\left(1 + \frac{1}{2}\gamma M_\infty^2\right). \tag{5.103}$$

(5.12) L. Howarth: ARC R M 1632 (1935)
        H. Schlichting: "Boundary-Layer Theory" McGraw-Hill, 6th ed. pp88 (1968)
(5.13) H. Schlichting: ibid. pp316

FIG. 5.5   Flow velocity (u) vs distance from the wall (y) when the gas flow hits the wall perpendicularly (normal incidence). y=0 is the stagnation point. u=-ay makes a good approximation when y is large or ν is small.

FIG. 5.6   Gas temperature (T) vs flow velocity (u) for the case of normal incidence. Subscripts ∞ and w indicate the edge of boundary layer and the wall.
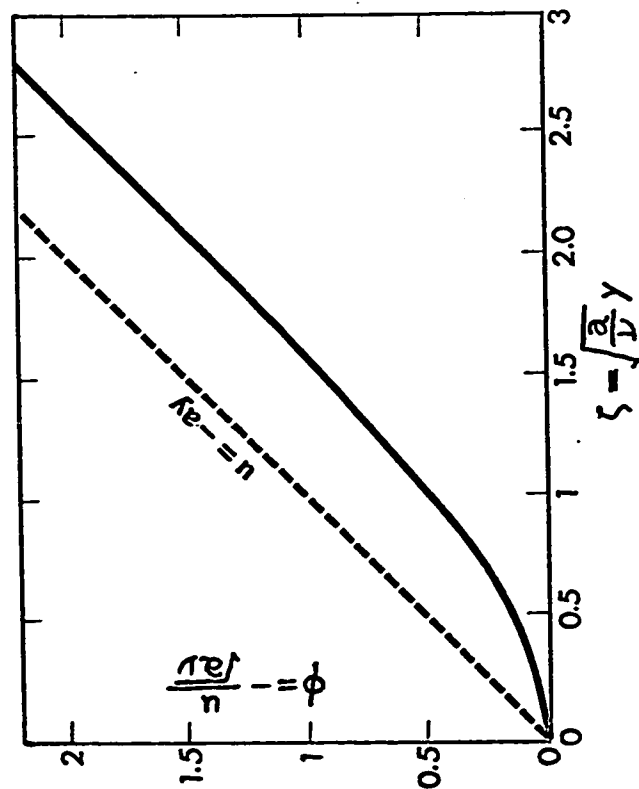
With the knowledge of the temperature and pressure we can immediately deduce the gas density from the relation of p=nkT. The Prandtl number which appears in Eqs. 5.99 and 5.100 is expressed by the square of the ratio of the thicknesses of the velocity and thermal boundary layers,

$$P_r \equiv \frac{c_p \eta}{k} = \left(\frac{\delta}{\delta_T}\right)^2. \tag{5.104}$$

Our experimental conditions will be considered for the rest of the section. The typical properties of the gas in our experiments (at M=18, T=1.2 eV) of

$\eta = 2.2 \times 10^{-4}$ (Kg/m·s)   (Fig. 4.6)

$L = 1 \times 10^{-4}$ (m)   (electrode diameter)

$m = 40 \times 1.67 \times 10^{-27}$ (Kg)   (argon atom)

$n = 3 \times 10^{23}$ (m^{-3})   (neutral density in the stagnated shock with $p_1 = 1$ mmHg)

and $u = 5 \times 10^3$ (m/s)

yield

Re=46,

$\delta = 1.5 \times 10^{-5}$ (m)

and $\delta_T = 1.8 \times 10^{-5}$ (m).   (5.105)

With this neutral density and wall temperature (300°K) the mean free path of argon is 8.4×10^{-6} (m) and more than 88% of argon atoms suffer at least one collision in the thermal boundary layer $(1 - \exp(-\delta_T/\lambda) = 0.88)$. Thus, a boundary layer can be defined and the Navier-Stokes equations can be considered as good approximating equations.

M is Eq. 5.103 is equal to M_5 in Eq. 5.91. Since M_1 (Mach number of an incident shock) is usually larger than 5, $M_5 = 3/5$ and p_s in Eq. 5.103 becomes, $p_s/p_\infty = 1.3$. As p(u) is a slowly varying function, we can say

approximately that $p=1.3p_\infty$ near the wall of the electrode. For the temperature in the boundary layer, the condition of

$$\sqrt{P_r}\frac{\gamma-1}{2}M^2 \simeq 0.1 \ll 1-\frac{T_w}{T_\infty} \simeq 1 \qquad (5.106)$$

shows that the linear distribution is a good approximation. Also by approximating the linear change of u with respect to y, T(y) can be expressed as,

$$T(y) = \frac{T_\infty - T_w}{y_\infty - y_w}\,y - \frac{y_w T_\infty - y_\infty T_w}{y_\infty - y_w}. \qquad (5.107)$$

The average neutral density can now be obtained as,

$$\bar{n} = \overline{\left(\frac{p}{kT}\right)} = \frac{1.3\,p_\infty}{k(y_\infty - y_w)}\int_{y_w}^{y_\infty}\frac{1}{T(y)}dy = \frac{1.3\,p_\infty}{k(T_\infty - T_w)}\ln\frac{T_\infty}{T_w}. \qquad (5.108)$$

Since $n_\infty = p_\infty/kT_\infty$, $T_\infty \gg T_w$ and $\ln(T_\infty/T_w)\simeq\ln(12000/300)=3.7$,

$$\frac{\bar{n}}{n_\infty} = 4.8. \qquad (5.109)$$

The density at the wall is,

$$\frac{n_w}{n_\infty} = \frac{P_w}{P_\infty}\frac{T_w}{T_w} = 1.3\frac{T_\infty}{T_w}. \qquad (5.110)$$

5.3   EFFECT OF THE ELECTRODE SURFACE

5.3.1   Field Emission of Electrons

When an intense electric field acts on the cathode surface, then an electron current flows out. This "field emission" electron current can be expressed by the Fowler-Nordheim equation, (5.14)

$$ j = \frac{4\sqrt{\mu\varphi}}{\mu+\varphi} \frac{e^3 E^2}{4\pi h \varphi} e^{-\frac{8\pi\sqrt{2m}}{3heE}\varphi^{3/2}} = 6\times10^{-6} \frac{\sqrt{\frac{\mu}{\varphi}}E^2}{\mu+\varphi} e^{-\frac{2.1\times10^8 \varphi^{3/2}}{E}} \quad (A/cm^2), \quad (5.111) $$

where E is the intensity of an electric field at the surface, φ is the thermionic work function and μ is the energy of the Fermi level inside the metal relative to the bottom of the conduction band. In the last term of the above equation φ and μ are involts and E is in V/cm.

For tungsten $\varphi=4.5$ V and the exact values of j are,

E (V/cm)	2×10^7	3×10^7	4×10^7	5×10^7	6×10^7
j (A/cm^2)	4.7×10^{-4}	3.7×10	1.1×10^4	3.9×10^5	4.2×10^6
E (V/cm)	7×10^7	8×10^7	9×10^7	10×10^7	12×10^7
j (A/cm^2)	2.3×10^7	8.7×10^7	2.5×10^8	5.7×10^8	2.1×10^9

If the temperature of the body is very high, then the current emission is enhanced (5.15). This is called thermo-field emission and the approximate current takes the form of,

$$ j(T) = \frac{\pi kT/d}{\sin(\pi kT/d)} j(0) \simeq \left(1 + 1.28\times10^8 \frac{T^2\varphi}{E^2}\right) j(0). \quad (5.112) $$

(5.14)   R.H. Fowler & L.Nordheim: Proc. Roy. Soc. A119 173 (1928)
         T.E. Stern, B.S. Gossling & R.H. Fowler: Proc. Roy. Soc. A124 699(1929)
         "Handbuch der Physik" Springer, Berlin 21 188 (1956)
(5.15)   T.H. Lee: J. Appl. Phys. 30 166 (1959)
         "Handbuch der Physik" Springer, Berlin 21 191 (1956)

··For tungsten at $E=4\times10^7$ V/cm, j(T) is given by,

T (°K)	300	1000	2000	3000
j(T)/j(0)	1.03	1.5	10	144

5.3.2 Electric Field Enhancement due to Surface Irregularities

Microgeometry of the irregularities of the cathode surface increases the electrical field by a factor we shall call β, i.e.,

$$\beta = \frac{\text{actual surface field}}{\text{applied field}} \; . \qquad (5.113)$$

Shottky (5.16) has shown how large values of β may be accounted for by a superposition principle. For example, if the emitting area under consideration is really a hemispherical boss on a cathode which on the scale of the boss is effectively an infinite plane, it is easy to show that $\beta=3$. If the area lies on a second hemispherical boss lying on the first and is small compared with it, then $\beta=3^2=9$, and so on.

Since field emission varies exponentially with E, it is evident that an intensification as small as 10% because of surface projections would cause most of the field emission current to flow from such points. This results in local temperature increase and enhanced secondary effects which lead to instability. Usually, for field emission, it has been experimentally found that (5.17),

(5.16) Shottky: Z. Physi $\underline{14}$ 63 (1923)
(5.17) W.S. Boyle, P. Kisliuk & L.H. Germer: J. Appl. Phys. $\underline{26}$ 720 (1955)
        W.J.R. Calvert: Proc. Phys. Soc. $\underline{B69}$ 651 (1956)
        C. Germain & F. Rohrback: Vacuum $\underline{18}$ 371 (1968)
        R.N. Bloomer & B.M. Cox: Vacuum $\underline{18}$ 379 (1968)

$$\beta = 3 - 100 \qquad (5.114)$$

and the electron emitting area is 10^{-10}-10^{-7} cm^2 for reasonably clean electrodes.

5.3.3 Argon Ion Interaction with a Tungsten Surface

An argon ion with a kinetic energy less than about 1 KeV incident on a metal surface undergoes two processes; (1) it becomes neutralized by an Auger transition a short distance in front of the surface, (2) the resulting gas atom transfers momentum to one or more metal atoms in predominantly elastic collisions. During both processes electron ejection can occur, while during the latter neutral metal atoms which have absorbed sufficient momentum may leave their lattice sites producing disorder, damage, and/or sputtering. The gas atom finally either comes to rest within the metal (i.e. becomes trapped) or escapes through the surface with reduced kinetic energy.

Argon ion trapping efficiency into tungsten at 20°C is, 10^{-5} at ion energy of 72 eV (experimental threshold of trapping), 0.0007 at 100 eV, 0.01 at 250 eV and 0.04 at 500 eV (5.18). Sputtering yield for tungsten bombarded by argon ion is, 0.001, 0.1, 0.2, 0.5, 0.7 and 0.8 atoms/ion at ion energy of 50, 100, 150, 200, 250 and 300 eV, respectively (5.19).

(5.18)   G. Carter & J.S. Colligon: "Ion Bombardment of Solids" Heinemann
          Educational Books Ltd., London pp363 (1968)
(5.19)   G. Carter & J.S. Colligon: ibid. pp321

5.3.4 Secondary Electron Emission from the Metal Surface

Secondary electrons can only be ejected from the surface of a metal by a positive ion if the sum of its kinetic (K_i) and potential energy (eV_i) exceeds 2e times the work function φ of the metal; this follows from the conservation of energy and the fact that for each ejected electron another electron has to escape to neutralize the positive ion. In the case of Ar^+ falling on the negatively biased probe made of tungsten, the above equation is generally satisfied and the secondary electron emission coefficient γ for various impinging ion energies is, (5.20),

V_i (eV)	10	100	1000
γ	0.096	0.095	0.099

It is important to know the energy distribution of the emitted electrons. These electrons fall into two distinct groups;

(1) small energy of 1-3 eV irrespective of primary ion energy, and

(2) a relatively narrow group of greater energy dependent on the nature of the target material and the energy of the incident ions (energy $\simeq K_i + eV_i - 2e\varphi$).

Mainly electron emission is caused by Auger de-excitation of an excited atom (first group) and the theoretical electron energy distribution for this group was obtained by Hagstrum (5.21). In the case of Ar^+ interaction with tungsten, the theoretical electron yield can be approximated by a velocity distribution function of

$$f(v) = 1.03 \times 10^{-7} v^3 e^{-2.61 \times 10^{-12} v^2} .$$

(5.115)

(5.20) H.D. Hagstrum: Phys. Rev. 104 317 (1956)
(5.21) H.D. Hagstrum: Phys. Rev. 96 336 (1954)

In the presence of intense electric field on the metal surface, γ has been observed to change its value. For instance, if H_2^+ hits steel, γ increases to about twice as large with increasing E field while for H^+ and steel there is not an appreciable change in γ (5.22). The variation of γ for Ar^+-W is not known.

It has been found that γ may become larger with ion energy of 1000 eV or more when the metal surface has adsorbed gas layers. This can be explained as follows. Since the ion has to expend energy in penetrating the adsorbed layer it has more chance of losing energy to atoms near the surface of the metal. The electrons are thus formed nearer to the surface and their diffusion through the adsorbed layer is easier than through the corresponding thickness of metal so that their escape is easier. In our case, however, the voltage applied across the sheath is usually the order of 200 volts and so the gas adsorption does not have much effect to the breakdown.

5.3.5 Ionic Charge Accumulation in the Sheath

If the charge exchange efficiency, η, between impinging ions and the electrode surface is not unity, the ionic charge is accumulated and the ion density increases in the sheath. If we denote the ion density and velocity at the electrode surface and sheath edge as $n_i(r_p)$, $v_i(r_p)$, $n_i(r_s)$ and $v_i(r_s)$, respectively, then (for a planar sheath),

$$n_i(r_s)v_i(r_s)=\eta n_i(r_p)v_i(r_p) \qquad (5.116)$$

and so it can be understood that the ion density in the sheath at

---

(5.22)   E.W. Webster, R.J. Van de Graaff & J.G. Trump: J. Appl. Phys. 23 264 (1952)

equilibrium is $1/\eta$ times the ion density when $\eta=1$. The equilibrium

is attained exponentially with a time constant of $2d/\eta\bar{v}_i$, where d is

the sheath thickness and $\bar{v}_i$ is the mean ion speed in the sheath. (The

time constant is of the order of one to ten nanoseconds for our experimental

conditions.)

The charge exchange efficiency of Ar^+ on W is approximately 80% (5.23)

and so the ion density should be considered to be 1.25 times larger than

the value obtained with $\eta=1$. If W is covered by an oxide surface layer,

η becomes smaller, and the density becomes higher. In the course of

calculation of the electric field in the sheath, the charge accumulation

effect can in effect be considered as if the ion current flowing into

the sheath is increased by a factor of $1/\eta$.

5.3.6 Adsorption and Chemisorption of Gases on the Metal Surface

The number of monolayers, N, formed on tungsten is (5.24),

$$N = 7 \times 10^7 p \frac{\tau_0}{\sqrt{AT}} e^{\frac{E_d}{RT}} \tag{5.117}$$

for $N \leq 1$. Here p is the pressure in mmHg, A is the molecular weight, T

is the surface temperature and E_d is the heat of adsorption/chemisorption.

For 10 mmHg argon, $E_d=1.9$ Kcal/mol, $\tau_0 \exp(E_d/RT)=10^{-12}$ sec (sojourntime)

and so $N=6.4 \times 10^{-6}$ monolayers. In other words, 6.4×10^{-4} % of the electrode

surface is covered by 3.2×10^9 argon atoms. Therefore the physical

adsorption of argon is negligible except when T is extremely low.

(5.23) R. Lawson: Private Communication (1970)
(5.24) G. Lewis: "Fundamentals of Vacuum Science and Technology"
       McGraw-Hill, pp45 (1965)

In the case of an oxygen molecule, $E_d=194$ Kcal/mol and so even at $p=10^{-10}$ mmHg, $N \gg 1$, which means that every oxygen molecules hitting the tungsten become trapped by chemisorption until a monolayer is formed. If the system is evacuated to 10^{-6} mmHg, the density of oxygen in the system is 6×10^9 cm^{-3}. At 300°K, 2.7×10^{14} oxygen molecules hit an area of 1 cm^2 per second. If it takes 10 seconds to fire the shock driver after ceasing to heat the electrode (actually it takes more than that), 2.7×10^{15} oxygen molecules per 1 cm^2 hit the tungsten. For tungsten trioxide (WO_3) monolayer to form, about 10^{15} oxygen molecules/cm^2 are necessary and so after 10 seconds tungsten electrode has a complete oxide monolayer. After the monolayer is formed, E_d decreases and the rate of chemisorption decreases exponentially. It is hard to find the number of layers formed, but it should be around 3-30 layers (5.25).

E_d of H_2, CO, CO_2 and N_2 on tungsten are 46, 100, 122 and 85 Kcal/mol, respectively and the chemisorption of these gases can be neglected in comparison with that of O_2. Adsorptions are, of course, much smaller than chemisorptions.

The surface structure of WO_3 formed by the chemisorption of oxygen on tungsten is (5.26),

$$\begin{array}{c}
\overset{\displaystyle O}{\overset{\|}{W}} \quad \overset{\displaystyle O}{\overset{\|}{W}} \quad \overset{\displaystyle O}{\overset{\|}{W}} \quad \overset{\displaystyle O}{\overset{\|}{W}} \\
\underset{W}{\overset{W}{\Big\rangle}} W \underset{W}{\overset{W}{\Big\langle}} \Big\rangle W \underset{W}{\overset{W}{\Big\langle}} \Big\rangle W \underset{W}{\overset{W}{\Big\langle}}
\end{array} \quad .$$
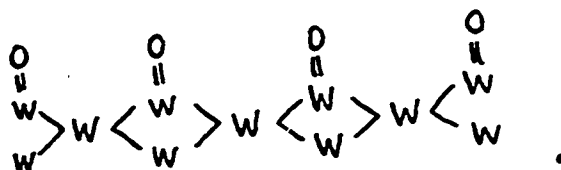
WO_2 is unstable at the room temperature and is not formed.

(5.25) R. Lawson: Private Communication (1970)
(5.26) N.K. Adam: "The Physics and Chemistry of Surfaces" Oxford (1941)

5.3.7 Cleaning of Electrode Surface by Heating

When the shock tube is driven by an intense arc discharge, small
parts of the electrode and insulator are melted, accelerated downstream
and contaminate the surface of the electrodes (or probes). Besides the
exposure of the electrode to any gas leads to an adsorption or chemisorption
of gas on the surface. The surface layers thus made form an electrical
insulator along the electrode surface and affect the electrode functioning
in many ways;

(1) Contamination affects the area of the electrode surface. The
reduction of the effective area by 1/10 or more was experienced.

(2) As will be discussed in Sec. 6.3, the electrode currents tend to have
spikes even at low electrode biases (as low as 15 volts, depending on
the surrounding plasma density and temperature), since on the surface
of the contamination are accumulated the electrical charges which, with
sufficient quantity, result in electron avalanches inside the contamination.

Most of this surface contamination can readily be removed by pre-
heating in vacuum the electrode to a sufficiently high temperature. (It
is for this purpose that tungsten was chosen as an electrode material.)
Tungsten can be repeatedly heated, cooled and air admitted without damage
to its properties, although heating renders the tungsten brittle. Espe
and Knoll (5.27) have given for tungsten wire of circular cross section
and of various diameters the current required to bring the tungsten to
various temperatures. As the melting points of tungsten and tungsten
trioxide are 3370 °C and 2130 °C, respectively, the heating to about 2230 °C
(1.3 A for 0.1 mm diameter wire) cleans the surface perfectly. The life

(5.27) Espe & Knoll: "Werkstoffkunde der Hochvakuumtechnik" Springer,
        Berlin (1936)

time of tungsten at 2230°C is 200 hours for 0.1 mm diameter wire and 150 hours for 0.05 mm diameter wire (5.28). The electrode was heated under high vacuum before each run for about one minute. The electrode of 0.1 mm diameter, therefore, can be used for at least 1000 times without any reduction in its diameter.

There is another advantage in heating the electrode, i.e., smoothing its surface. At about a quarter of the absolute melting temperature, surface migration allows the atoms on the rough tip to rearrange themselves, reducing the free surface energy. Perfect smoothness is achieved after a few minutes at 2/3 of the absolute melting temperature, provided that no oxides or other contaminations still stable at this temperature are present.

The hair pin type electrodes as seen in Fig. 3.3 were made so that they can be heated white hot. McLaren et. al. (5.29) reported the successful use of this type of probe but with shorter tungsten wires. If the probe is long, it disturbs the plasma and also degrades the spatial resolution. On the other hand, the short probe has more ambiguity in the probe area because of the small unheated part of the tungsten feed-through joint.

5.3.8 Cleaning of Electrode Surface by Ion Sputtering

When the electrode is surrounded by ionized gas, high energy ions hit the negative electrode, which results in the sputtering of oxide

(5.28) M. Pirani & J. Yarwood: "Principles of Vacuum Engineering" Reinhold Publishing Co. (1961)

(5.29) T.I. McLaren, J.N. Fox & R.M. Hobson: 6th Int'l Conf. Ionization Phen. in Gases 4 311 (1963)

surface layer on the electrode. An empirical formulation for the time during which N layers of tungsten are destroyed by argon ions is,

$$t = 10^{-8} \frac{N}{jp} \quad (\text{sec}),$$

(5.118)

where j is the current density into the electrode in A/cm^2 and p is the ambient pressure in mmHg. By substituting our typical experimental conditions of N=10, j=1 (A/cm^2) and p=10 (mmHg), we obtain t=0.1 μsec.

On the other hand, oxidation of the surface continues during this period. This rate, however, is only 1.5×10^{-5} monolayers per sec with shock processed oxygen molecules of 10^4 °K and 10^{-4} mmHg, and so further oxidation can be completely neglected. Thus with the arrival of plasma at the electrode, the WO_3 surface layer on the surface is destroyed within about 1 μsec and after that the electrode can be considered to have a tungsten metal surface.

After a long period of sputtering (a time long enough for over 100 layers to be removed), there appear on the electrode surface many irregularities which have a strong influence on the electric field at the surface (Sec. 5.3.2).

5.3.9 Breakdown of WO3 Surface Layer

Although most of the WO_3 will be destroyed by ion sputtering, there still may remain some on the electrode surface. The conductivity, σ, of WO_3 was measured to be 5×10^{-8} mhos/m at an electric field of 10^6 V/cm in WO_3 (with higher field, the conductivity becomes lower) (5.30). By denoting the current density to the WO_3 layer as j, the electric field in the WO_3 can be expressed as j/σ. If j exceeds 0.01 A/cm^2, the field becomes higher

(5.30) A. Guntherschulze & H. Betz: Z. Physik 71 106 (1931)

than 2×10^7 V/cm which is sufficient for field electron emission. In such a case the spikes may be observed in the electrode current and this may sometimes lead to the full path breakdown.

5.4 EFFECT OF THE TEMPERATURE OF THE ELECTRODE SURFACE

5.4.1 Thermionic Electron Emission

Thermionic electron current is expressed by the Richardson-Dushman equation,

$$j = AT^2 e^{-\frac{e\varphi}{kT}} \qquad (A/cm^2),$$

(5.119)

where A is the thermionic emission constant and φ is the thermionic work function. $A = 70$ A/cm^2·K^2 and $\varphi = 4.5$ V for tungsten (5.31) and $A = 5 \times 10^{11}$ A/cm^2·K^2 and $\varphi = 9.22$ V for WO$_3$ or W-O film (5.32).

5.4.2 Basic Theory of Hot Cathode Arc Discharge

In the case of an arc discharge the secondary electron emission constant due to positive ion impact, γ, must be replaced by γ', which gives the number of electrons, thermionic and secondary by bombardment, liberated per positive ion at the cathode. Thus we can write,

---

(5.31) D.A. Wright: Proc. Inst. Elect. Engrs. 100 pt. 3, 125 (1953)
(5.32) V.S. Fourenko: "Handbook of Thermionic Properties" Plenum Press, Data Division pp129 (1966)

$$\gamma' = \frac{I_e}{I_i} \, , \qquad (5.120)$$

where I_e and I_i are the electron and ion currents at the cathode. If we take I_t as the current due to thermionic emission specified by Richardson equation (Eq. 5.119), the total electron current at the cathode is then, $I_e = \gamma I_i + I_t$, and the total current, I, is, $I = I_e + I_i = (1+\gamma)I_i + I_t$. From this we can evaluate γ' as,

$$\gamma' = \gamma + \frac{1+\gamma}{\frac{I}{I_t} - 1} \, . \qquad (5.121)$$

If a current I_0 is emitted from the anode (or in our case if I_0 enters from the cathode sheath edge), then,

$$I_i = I_0 + I_e\left(e^{\int_{r_p}^{r_s}\alpha dr} - 1\right) = I_0 e^{-\int_{r_p}^{r_s}\alpha dr} + I\left(1 - e^{-\int_{r_p}^{r_s}\alpha dr}\right). \qquad (5.122)$$

By eliminating I_i and I_e we obtain,

$$I = \frac{e^{\int_{r_p}^{r_s}\alpha dr}}{1 - \gamma\left(e^{\int_{r_p}^{r_s}\alpha dr} - 1\right)} I_t + \frac{1+\gamma}{1 - \gamma\left(e^{\int_{r_p}^{r_s}\alpha dr} - 1\right)} I_0 \, . \qquad (5.123)$$

The condition of breakdown is determined by $I/I_0 \to \infty$, or,

$$I = \frac{e^{\int_{r_p}^{r_s}\alpha dr}}{1 - \gamma\left(e^{\int_{r_p}^{r_s}\alpha dr} - 1\right)} I_t . \qquad (5.124)$$

By using γ' of Eq. 5.121 this condition can be rewritten as,

$$\gamma'\left(e^{\int_{r_p}^{r_s}\alpha dr} - 1\right) = 1. \qquad (5.125)$$

When ionization effects in the sheath are negligible, Eq. 5.123 can be reduced to $I = I_t + I_0$ and the condition of breakdown is simply,

$$I = I_t . \qquad (5.126)$$

5.4.3 Self Sustaining Arc Discharge

To see how a self sustained arc can be established, we will examine the simplified case where the energy input to the cathode is due to ion bombardment ($=I_i V$, V=potential difference across cathode sheath) and the output is due to the radiant energy emission. More precise discussion of the energy balance will be done later. The basic mechanism of the discharge, however, does not change from this simplified case. The cathode temperature can be determined by equating the input and output as,

$$I_i V = S \sigma T^4,$$

where black body radiation was assumed. σ is the Stefan-Boltzmann constant ($=5.67 \times 10^{-12}$ W/cm^2°K^4) and S is the area of the cathode surface involved. The Richardson equation takes the form,

$$I_t \equiv F(I_i V) = SAT^2 e^{-\frac{e\varphi}{kT}} = SA\left(\frac{I_i V}{S\sigma}\right)^{\frac{1}{2}} e^{-\frac{e\varphi}{k\left(\frac{I_i V}{S\sigma}\right)^{\frac{1}{4}}}}$$

$$= 3.03 \times 10^7 \sqrt{S I_i V} \; e^{-\frac{80.8}{(I_i V/S)^{\frac{1}{4}}}} \quad \text{(A)}. \tag{5.127}$$

From Eqs. 5.122 and 5.123,

$$I = \frac{1+\gamma}{1-\gamma\left(e^{\int_{r_p}^{r_s}\alpha dr}-1\right)} I_o + \frac{e^{\int_{r_p}^{r_s}\alpha dr}}{1-\gamma\left(e^{\int_{r_p}^{r_s}\alpha dr}-1\right)} F\left[I_o V e^{-\int_{r_p}^{r_s}\alpha dr} + \left(1-e^{-\int_{r_p}^{r_s}\alpha dr}\right) IV\right]. \tag{5.128}$$

If ionization effects in the sheath are very small,

$$I \simeq I_o + F\left[I_o V + IV\int_{r_p}^{r_s}\alpha dr\right]. \tag{5.129}$$

Equation 5.128 will be examined further. Let us put the left hand side of the equation as y_1 and the right hand side as y_2. y_1 and y_2 as functions of I have the shapes of Fig. 5.7. Fig. 5.7-A is valid when I_0 is small. Initially I stays at I_1 (which is a stable solution). If I_0

FIG. 5.7-A   The right and the left hand side of Eq. 5.128. The solutions are I_1 and I_3.
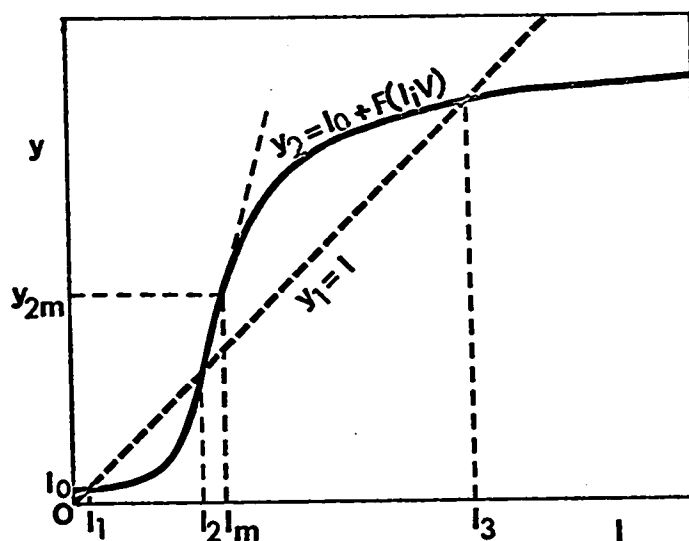
FIG. 5.7-B   The condition of breakdown for I_0 $(=I_{0b})$. I jumps from I_b to I_3.
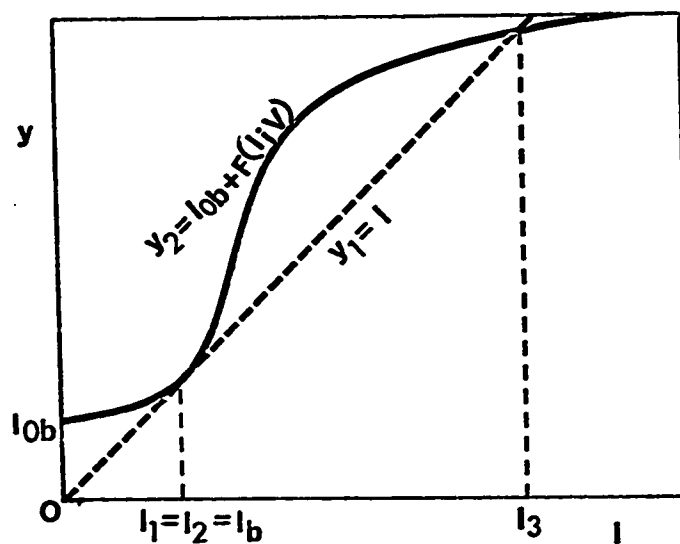
FIG. 5.9   V-I characteristics of an arc discharge of Eq. 5.128.
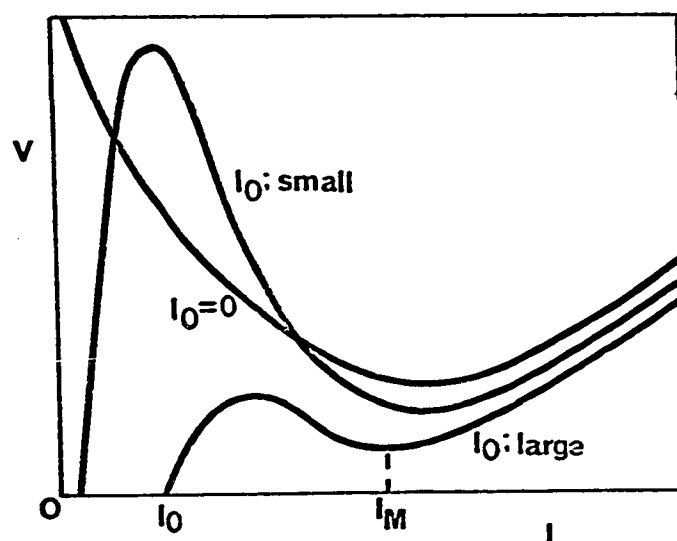
is increased, $y_2(I)$ curve floats up and with $I_0=I_{0B}$ (Fig. 5.7-B) I jumps from $I_B(=I_1=I_2)$ to I_3 (I_3 is also stable but I_2 is unstable). Now if I_0 is decreased, $y_2(I)$ curve sinks down to Fig. 5.7-A with I staying at I_3, and even with $I_0=0$, I does not become zero. This indicates a self sustaining discharge.

The relation of I vs I_0 is shown in Fig. 5.8-A, B and C for three cases of V.

(1) small V: With increasing I_0, $I(I_0)$ curve follows O→E, and E→O with decreasing I_0. I is increased slightly more than I_0 by the thermionic electron current.

(2) intermediate V: If I_0 is increased from zero, I vs I_0 curve follows O→A→B and jumps to D, then to E. If I_0 is decreased from that point, I changes as E→D→C→(jump)→A→O and I cannot be self sustained. However, I at point D usually exceeds 10^{10} A/cm^2, in which case I is restricted by an external circuit and is practically considered to be a breakdown.

(3) large V: If I_0 is increased I follows O→B→(jump)→D→E and if it is decreased, E→D→C. At point C, a self sustained arc is being formed and the condition of Eq. 5.125 is satisfied.

Let us denote the values of I and y_2 which give $d^2y_2/dI^2=0$ when $I_0=0$ as I_m and y_{2m}. Then,

$$I_m = \frac{S\sigma \left(\frac{\sqrt{17}-1}{8}\frac{e\varphi}{k}\right)^4}{\left(1-e^{-\int_{r_p}^{r_s}\alpha dr}\right)V} = \frac{9.93\times10^5 S}{\left(1-e^{-\int_{r_p}^{r_s}\alpha dr}\right)V}, \tag{5.130}$$

$$y_{2m} = SA\left(\frac{\sqrt{17}-1}{8}\frac{e\varphi}{k}\right)^2 e^{-\frac{8}{\sqrt{17}-1}} = 2.35\times10^9 S \tag{5.131}$$

and $$\left[\frac{dy_2}{dI}\right]_{I=I_m} = \frac{A}{\sigma}\left(\frac{k}{e\varphi}\right)^2\frac{32(3+\sqrt{17})}{(\sqrt{17}-1)^3}e^{-\frac{8}{\sqrt{17}-1}}\left(1-e^{\int_{r_p}^{r_s}\alpha dr}\right)V = 2.67\times10^3\left(1-e^{\int_{r_p}^{r_s}\alpha dr}\right)V. \tag{5.132}$$

FIG. 5.8   I vs I_0 of Eq. 5.128

at various values of V.

A.   Small V, $\gamma'\left(e^{\int_{r_p}^{r_s}\alpha dr}-1\right)<1$.

No breakdown occurs even with $I_0=\infty$
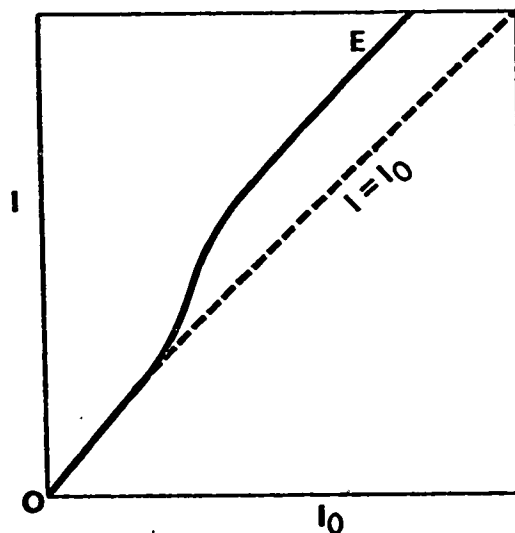
B.   Intermediate V, $\gamma'\left(e^{\int_{r_p}^{r_s}\alpha dr}-1\right)<1$.

Current jump occurs at I_{0B}. This

is not a self sustaining discharge,

since I becomes zero with $I_0=0$.

However, if I_D is larger than the

current available from the external

source, then this can be considered

as an actual breakdown.
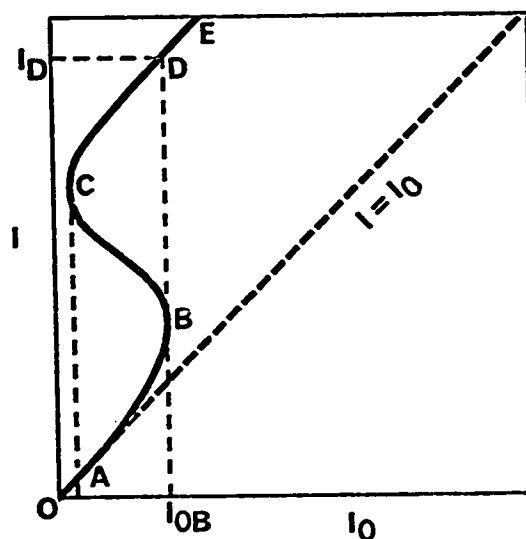
C.   Large V, $\gamma'\left(e^{\int_{r_p}^{r_s}\alpha dr}-1\right)=1$.

Self sustaining breakdown occurs if

I_0 is increased up to I_{0B} and then

decreased to zero.
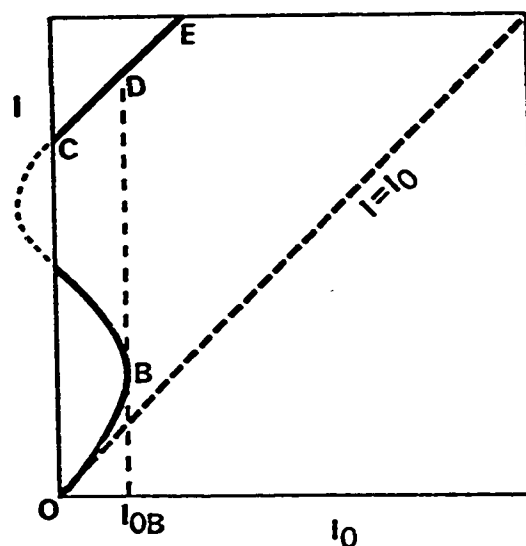
The last terms of these equations were calculated for the case of a tungsten electrode. The condition for a self sustaining discharge is that Eq. 5.128 has three solutions when $I_0 = 0$. By considering that $F(I_i V)$ is an exponential function, this condition can be replaced by the condition that $F(I_i V)$ becomes larger than I at some value of I. Therefore as a sufficient condition,

$$Y_{2m} = 2.35 \times 10^9 > I_m = \frac{9.93 \times 10^5}{(1 - e^{-\int_{r_s}^{r_p} \alpha dr}) V} \tag{5.133}$$

$$\text{or} \quad (1 - e^{-\int_{r_p}^{r_s} \alpha dr}) V > 4.22 \times 10^{-4}. \tag{5.134}$$

Even with the severest conditions that $\alpha = 0.09 \ cm^{-1}$ (at 100 mmHg) and $r_s - r_p = 5 \times 10^{-4} \ cm$,

$$V > 10 \text{ volts}$$

is the condition for a self sustaining discharge. This is always satisfied, since V never becomes smaller than the ionization potential, V_i.

The V-I characteristics of an arc discharge of Eq. 5.128 are seen in Fig. 5.9 with I_0 as step functions of various amplitudes (not impulses). Since I_M in the figure is the order of $10^5 \cdot A/cm^2$, the practical experimental range lies on the left hand side of I_M and the N shaped curve cannot be observed.

5.4.4 Energy Balance at the Cathode

The cathode temperature can be determined by equating the input energy to the output energy at the cathode, where (5.33):

(5.33) K.T. Compton: Phys. Rev. 37 1077 (1931)

Energy input $= I(1-f)(aV_p + V_i - \varphi_0) + P_J + P_H + P_F + P_N$

Energy output $= If\varphi_1 + P_E + P_C + P_D + P_R$

and f = fraction of current carried by electron at cathode.

a = accomodation coefficient (fraction of kinetic energy of ion delivered to cathode, $a = 0.9-1$)

V_p = cathode potential drop

V_i = ionization potential of gas

φ_0 = normal work function (work function at $E = 0$)

φ_1 = effective work function (work function at E present, for thermionic electron emission, $\varphi_1 = \varphi_0$ and for field emission $\varphi_1 = 0$)

P_J = Joule heating

$P_H = F(f(V_p - \varphi_0 + \varphi_i) - (1+\delta)(1-f)V_i - V_e)$ = heating by energy derived by electrons in the cathode fall space and indirectly returned to cathode

$\varphi_i = V_i - \varphi_1 + L$ = heat of neutralization of ion

L = heat of condensation of neutrals of cathode

F = fraction of the energy acquired by unelectrified carriers from the electrons which have moved through the fall space, which returns to the cathode as by radiation, metastable state, etc.

V_e = electron mean kinetic energy in plasma

P_F = radiation heating

P_N = heating by neutral particles

P_E = cooling by evaporation

P_C = cooling by conduction through cathode

P_D = cooling by gas conduction and convection

P_R = cooling by radiation.

5.4.5 Heat Conduction into the Metal

The basic equations of heat transfer are,

$$q = -Ak\nabla T \qquad (5.135)$$

and

$$\frac{\partial T}{\partial t} = a\nabla^2 T + \frac{W}{c\rho} , \qquad (5.136)$$

where $T(r,t)$ = temperature (°F)

A = area (ft^2)

q = rate of heat flow (Btu/hr)

W = heat generation per unit volume per unit time (Btu/hr·ft^3)

ρ = mass density (=1208 lb$_m$/ft^3 for tungsten)

c = specific heat (=0.032 Btu/lb$_m$°F for tungsten)

k = thermal conductivity (=87 Btu/hr·ft· F for tungsten)

and $a = k/c\rho$ = thermal diffusivity (=2.430 ft^2/hr for tungsten).

(1 watt/cm^2=3171 Btu/hr·ft^2, 1 cal/sec·cm·°C = 242 Btu/hr·ft·°F)

Equations 5.135 and 5.136 are solved for the four cases below.

(1) Constant heat flux coming into a semi-infinite body (one dimensional) (5.34).

$$T(x,t) = \frac{2q}{Ak}\sqrt{\frac{at}{\pi}}\, e^{-\frac{x^2}{4at}} . \qquad (5.137)$$

(2) Q is suddenly generated on each unit area of a plane in an infinite body at x=0, t=0 (one dimensional).

$$T(x,t) = \frac{Q}{2k}\sqrt{\frac{a}{\pi t}}\, e^{-\frac{x^2}{4at}} . \qquad (5.138)$$

(5.34) L.R. Ingersoll, O.J. Zobel & A.C. Ingersoll: "Heat Conduction" McGraw-Hill (1954)

(3) Constant heat is generated inside the body (uniform).

$$T(t) = \frac{W}{c\rho} t.$$ (5.139)

(4) Constant heat flux is emitted at r=0 (three dimensional) (5.35).

$$T(r,t) = \frac{q}{4\pi k r} \left(1 - \text{erf} \frac{r}{2\sqrt{\alpha t}}\right).$$ (5.140)

For our electrode, when immersed in a plasma, ions of energy eV_p hit the cathode surface and transfer an energy of about $j_i V_p$. In the typical case of j_i=10 A/cm^2 and V_p=100 V, the temperature rise of the tungsten electrode at the surface is from Eq. 5.137, only 19 °C after 1 msec, which is far too low for thermionic electrons to be emitted. If the surface of the electrode is covered by a layer of WO_3, then ρ=448 lb$_m$/ft^3, c=0.073 Btu/lb$_m$°F, k=0.1-1 (5.36) and Eq. 5.137 yields a temperature rise of 9-30°C.

5.4.6 Local Heating due to Current Focusing on the Electrode

When the sheath breakdown voltage is about 100 V, the current into the electrode is the order of 1 amperes. If this current is focused into a small area of the electrode, for say 10 μsec, then the temperature rise around the point is, from Eq. 5.140,

$$T(r) = \frac{5.37}{r} \left(1 - \text{erf } 2\text{b}2\, r\right),$$ (5.141)

where r is in cm and T is in °C. At r=1000 Å from the current injection point, the temperature rises to T=5.37x10^5°C.

(5.35) M. Jakob: "Heat Transfer I" John Wiley & Sons, N.Y. pp339 (1949)
(5.36) "Gmelins Handbuch der anorganischen Chemie" Verlag Chemie, Bergstrasse. 54 (1962)

At the cathode spot in the arc discharge the current density was shown to be between a few thousand and more than a million A/cm^2 (5.37). The temperature obtained above is sufficiently high to emit that amount of current density (Eq. 5.119).

5.4.7 Local Heating of Electrode by Ion Bombardment

The rate of the heat flow in our experimental conditions is enormous (even though the temperature rise is very small) and it is quite possible that thermal equilibrium is not attained in the metal. If it is so, then a microscopic treatment should be used.

The average depth, $\overline{L}$, of atoms (of atomic number Z_1, mass m_1 and initial energy E) penetrating into metal (of atomic number Z_2, mass m_2 and density n) is expressed as (5.38),

$$\overline{L} = \frac{1}{1+\frac{1}{3}\frac{m_2}{m_1}}\frac{3.06\,(1+m_2/m_1)E}{4\pi n a Z_1 Z_2 e^2} , \qquad (5.142)$$

where $a = 0.8853 a_0/(Z_1^{2/3}+Z_2^{2/3})^{1/2}$ and $a_0 = \hbar^2/m_e e^2 = 0.523 \times 10^{-8}$ cm is Bohr's critical radius. The $1+m_2/3m_1$ term is for the projected path length. In the case of 100 eV argon (atomic diameter=3.82 Å) penetrating into tungsten (atomic diameter=2.82 Å),

$$\overline{L} = 0.478 \text{ Å.}$$

The relaxation time for phonon-phonon collision is (5.39),

$$\tau_{pp} = 10^{-11} \text{ sec}$$

and that of electrons for electron-phonon collisions is,

$$\tau_{cp} = 10^{-13} \text{ sec}$$

$$\tau_{pe} = 10^{-11} \text{ sec.}$$

(5.37) J.D. Cobine & E.E. Burger: J. Appl. Phys. 26 895 (1955)

If the heat flux input is, as before, 100 W/cm^2 which is confined into a 0.478 Å thick layer along the metal surface, then the temperature rise of the layer in 10^{-11} sec is, from Eq. 5.139, 0.9°C. After this time the energy of the layer begins to be diffused into the metal by phonons, and T is specified by Eq. 5.137. Again this temperature is very low.

If an incident atom hits only one metal atom, then the atom is heated to the temperature of eV_p/k for 10^{-13} seconds, after which it begins to cool off. If ion current with ion energy of 100 eV flows into an electrode, then each ion heats electrode atoms to 1.16×10^6 °K. Thermionic electron current from one atom of $\pi \times (1.41 \times 10^{-8})^2 \times 9.7 \times 10^{13}$ (Amps) flows for 10^{-13} sec (1.41×10^{-8} is the radius of tungsten atom), so that the ratio of secondary electron current to primary ion current becomes 3.8×10^4.

Although this current increase rate looks quite impressive for the explanation of breakdown phenomena, we have to give up this idea because of the fact that the current ratio thus obtained is independent of the plasma density (i.e., ion current into the electrode). From the experimental results, the breakdown voltage is a function of plasma density. The fault of this theory might be the use of Richardson's equation, which is not proved to be correct in the thermally non-equilibrium state.

(5.38)   G. Carter & J.S. Colligon: "Ion Bombardment of Solids" Heinemann Educational Books Ltd., London pp97 (1968)

(5.39)   C. Kittel: "Introduction to Solid State Physics" John Wiley & Sons Inc. N.Y. (1967)

CHAPTER VI   EXPERIMENTS ON THE BREAKDOWN BETWEEN CYLINDRICAL ELECTRODES

IN A PLASMA

6.1 BREAKDOWN VOLTAGE IN A NEUTRAL GAS

The breakdown voltage (V_b) between two cylindrical tungsten electrodes in an unionized argon gas was measured. The radius (r_p) and the length of both electrodes were 0.05 mm and 35 mm, respectively. The interelectrode distance (d) and the ambient pressure (p) were varied. In Fig. 6.1 is shown the measured breakdown voltages. Theoretical V_b obtained from Eq.5.24 and A=13.6 ($cm^{-1}mmHg^{-1}$), B=235 (V/cm·mmHg) (5.2) and γ=0.1 are shown in Fig. 6.2.

Curves of Fig. 6.1 are replotted in terms of $V_b/\ln(d/r_p)$ in Fig. 6.3, together with the theoretical values obtained from Eq. 5.24. As expected from Eq. 5.28, all the curves tend to coincide with one line except for small p and large d. When p is small the last term of Eq. 5.24 becomes significant and Eq. 5.28 is no longer valid; when d is large the streamer mechanism takes place and changes the picture of the breakdown phenomena greatly. Also in Fig. 6.3 the results of Meek and Craggs (6.1) are plotted. In their case a cylindrical wire and concentric cylindrical electrodes were used; the wire electrode was negative (electrode material unknown).

The constancy of $V_m/2p_m(d-r_p)$ of Eq. 5.26 from our data is examined in the Table 6.1. The experimentally obtained B is approximately 30%

(6.1) J.M. Meek & J.D. Craggs: "Electrical Breakdown of Gases" Oxford, Clarendon Press pp60 (1953)

FIG. 6.1   Measured breakdown voltage between cylindrical
tungsten electrodes (of radius 0.05 mm) in neutral argon
at various pressures (p) and electrode separations (d).

FIG. 6.2   Theoretical breakdown voltage between cylindrical tungsten electrodes (of radius 0.05 mm) in neutral argon at various pressures (p) and electrode separations (d) obtained from Eq. 5.24 with $A=13.6$ $cm^{-1}mmHg^{-1}$, $B=235$ $V/cm \cdot mmHg$ and $\gamma=0.1$.

FIG. 6.3 Experimentally obtained breakdown voltage between cylindrical tungsten electrodes plotted in the form of Eq. 5.28. **X** marks show the theoretical values obtained from Eq. 5.24 and **O** marks show the experimental values of Meek and Craggs (6.1).
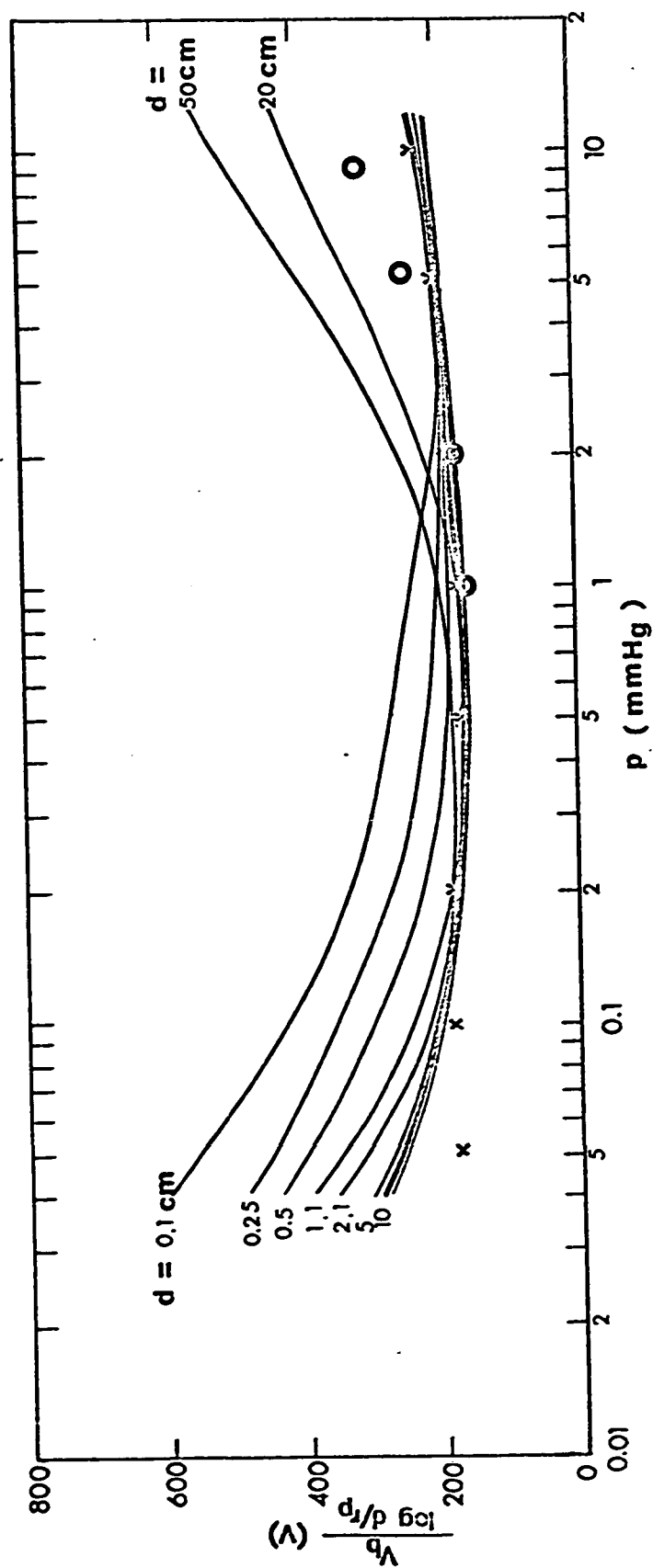
smaller than the value given by Meek and Craggs (=235) and 7% smaller

than the value given by von Engel (5.3) (=180) except for large d. When

d is large V_b and hence B is reduced by a streamer mechanism. In addition,

·the 35 mm long wire electrode has to be approximated by a point electrode

rather than a cylindrical electrode. The theoretical absolute minimum

voltage, V_{mm} can be calculated from Eq. 5.27 to be 225 volts for Meek's

values of A and B, and 195 volts for von Engel's values. The minimum

sparking voltage for parallel plate electrodes was found to be 195-275

volts (6.2).

It should be noted that contrary to the remarks of von Engel (6.3)

that in the case of breakdown between two concentric cylindrical electrodes

the equivalent formula for Eq. 5.24 does not agree with observations, the

experimental results in our case agreed reasonably well with the theory

developed here.

6.2   SHORT GAP BREAKDOWN EXPERIMENTS

The hair pin type electrodes used in the plasma breakdown experiments

were mounted face to face in a specially made electrode holder with which

the distance between the tips of the electrodes can be adjusted within

an accuracy of 1×10^{-5} inches. This device was put into the vacuum jar

(pressure=0.05 mmHg) and the breakdown voltage between these two electrodes

was measured.

(6.2)   L.B. Loeb: "Fundamental Processes of Electrical Discharge in Gases"
          John Wiley & Sons Inc. N.Y. pp414 (1939)
(6.3)   A. von Engel: "Ionized Gases" Oxford, Clarendon Press pp191 (1965)

d(cm)	p_m(mmHg)	V_m(V)	$V_m/2p_m(d-r_p)$	B from (6.1)
0.1	5	255	260	235
0.25	2.5	265	210	"
0.5	2	340	170	"
1.1	1	350	160	"
2.1	0.5	380	180	"
5	0.3	410	140	"
10	0.18	450	130	"
20	0.14	600	110	"
50	0.1	780	80	"

TABLE 6.1   The minimum breakdown voltage, V_m, and p_m which gives V_m at various values of d. In the table the experimentally obtained B ($=V_m/2p_m(d-r_p)$) and the value of B taken from Meek (6.4) are also compared.

The electrodes used were bombarded by argon ions in the shock tube for various times beforehand. The measured breakdown voltage as a function of electrode separation (d) yielded straight lines (d=0-3x10^{-3} cm, V_b=0-800 V) which showed that the electric field at the electrode surface, E_p, were constant. The value of E_p changed with the degree of bombardment and was, from Eq. 5.19,

$$E_p = 2 - 4x10^5 \text{ V/cm.}$$

The same kind of short gap vacuum breakdown has been investigated by many people, especially Kisliuk and others (7.4), and the breakdown was found to be triggered by electron field emission from the cathode surface. This theory applies to our case. For our hair pin type electrodes, $E=2-4x10^5$ V/cm is necessary to extract electrons from the cathode. The field required for the field emission is, from Sec. 5.3.1, $4x10^7$ V/cm, and the discrepancy is attributed to the field intensification by the surface irregularities. By using the notation of Sec. 5.3.2 β for our case is calculated as,

$$\beta = 100 - 200.$$

β is large due to ion bombardment.

6.3 THE EFFECT OF ELECTRODE CONTAMINATION ON THE BREAKDOWN VOLTAGE

Two cylindrical electrodes were immersed in the plasma and the electrical breakdown voltage between these two was measured. The plasma was produced by the electromagnetically driven shock tube mentioned in the previous sections.

After some trials it was found that in addition to very bad reproducibility of the breakdown voltage, there were no correlations between

breakdown voltage and plasma density, neutral particle density, electrode separation, etc. However, by integrating the electrode current with respect to time until breakdown occurs (t_b) it was found that

$$\int_0^{t_b} I \, dt = 2 - 4 \quad (\mu\text{coul})$$

for most of the cases at various experimental conditions. Detailed examples are listed in Table 6.2-A. The reason of the constancy of the integral can be considered as follows. Due to the intense arc discharge in the shock tube driver, small portions of electrodes and insulator materials of the driver are melted, pushed downstream, and some of them stick to the surface of the electrode, forming an insulating surface layer. In the presence of oxygen, the oxidation of the electrode surface also makes an insulating layer. Now, if a potential difference, V_d, is applied on two electrodes in a plasma, these electrodes act as a floating double electrostatic probes and begin to collect ions and electrons. However, because of the insulating surface layer, the electric charge starts accumulating on the surface of the layer, making an electric field of the order of $(\int_0^{t_b} I \, dt)/\varepsilon_0 S$ inside the layer, where S is the electrode surface area. When this electric field becomes large enough ($- 3 \times 10^6$ V/cm) an electron avalanche starts inside the layer, which produces enough electrons to trigger the breakdown between electrodes. The same effect was reported by Hancox (6.4), who made an artificial surface layer and found that $\int_0^{t_b} I \, dt$ was constant.

To eliminate this effect, the electrodes were heated to approximately 2300°C for one minute before each measurement (Sec. 5.3.7). With cleaned electrodes $\int_0^{t_b} I \, dt$ was measured again with the results in Table 6.2-B. In this case the integral did not take constant values. For contaminated

(6.4) R. Hancox: Brit. J. Appl. Phys. 11 468 (1960)

Date	z (cm)	V_C (KV)	P_1 (mmHg)	V_b (V)	$\int_0^{t_b} I\,dt$ (A·μsec)
Mar. 18	68	2.5	0.1	110	2
Jun. 25	"	"	0.1	130	2.5
"	"	"	0.05	150	3
"	"	"	0.5	125	4
July 22	"	"	1	350	2
"	"	"	10	350	2.5

TABLE 6.2-A $\quad \int_0^{t_b} I\,dt$ with contaminated electrodes.

DATE	z (cm)	V_C (KV)	P_1 (mmHg)	V_b (V)	$\int_0^{t_b} I\,dt$ (A·μsec)
July 22	68	2.5	0.1	600	0.2
"	"	"	0.1	200	20*
"	"	"	1	600	0.7
"	"	"	10	600	1.3
"	111	"	0.1	600	0.1
"	"	"	0.1	200	20*
"	"	"	1	600	0.56
"	"	"	5	600	0.6

TABLE 6.2-B $\quad \int_0^{t_b} I\,dt$ with clean electrodes.

* indicates that no breakdown was observed.

electrodes to breakdown, the integral, not V_d, is important and V_d can be much smaller than the true breakdown voltage.

Besides leading to an interelectrode breakdown, electric charge accumulation often causes small, successive electron avalanches in the contamination layer of the electrode surface. This effect can be seen in Figs. 6.4 and 6.5. In the following sections electrodes were always cleaned before taking measurements, unless otherwise mentioned.

6.4 PRE-BREAKDOWN CURRENT CHARACTERISTICS

If the electrode potential, V, is increased without changing the plasma properties, the electrode current, I, experiences three stages, i.e.:

Stage (1) When V is far below the breakdown voltage, V_b, the electrode works as a Langmuir probe, and I can be expressed by the equations in Sec. 2.7.

Stage (2) When V is increased, electron avalanches begin to take place in the cathode sheath, which cause an increase in I.

Stage (3) At $V \geq V_b$, I is dominated mainly by the external circuit.

In actual cases, it has been known from the experiments that there are two types of I vs V characteristics, as seen in Figs. 6.6-A and B. Three stages are clearly shown in Fig. 6.6-A, whereas in Fig. 6.6-B, stage (2) is unnoticeable and stage (3) follows immediately after stage (1).

In Fig. 6.7 are shown the C.R.O. traces of I_p with various values of V. Constant V was applied from t=0 to infinity. The plasma surrounding the electrodes was a weak precursor plasma (6.5). It reaches the electrodes
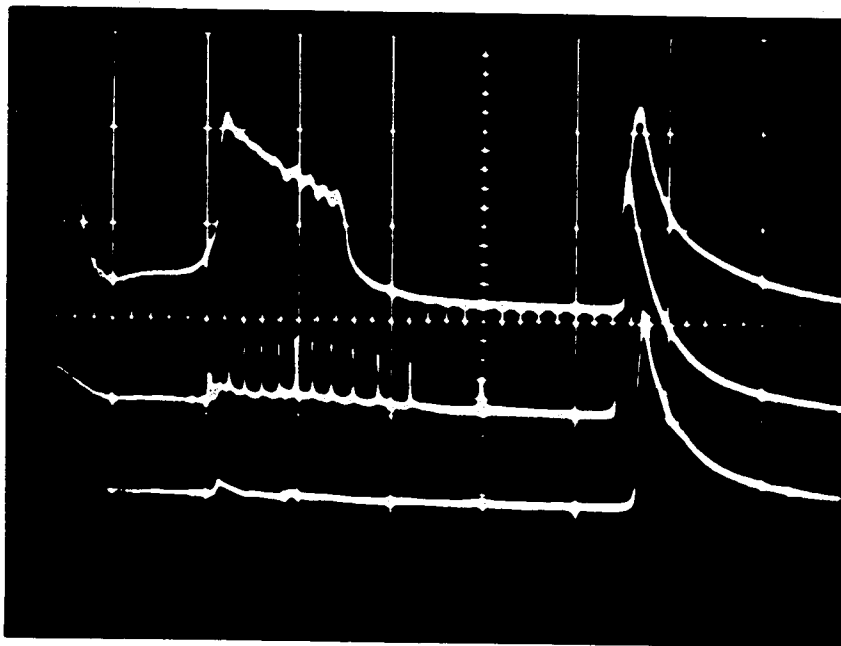
FIG. 6.4
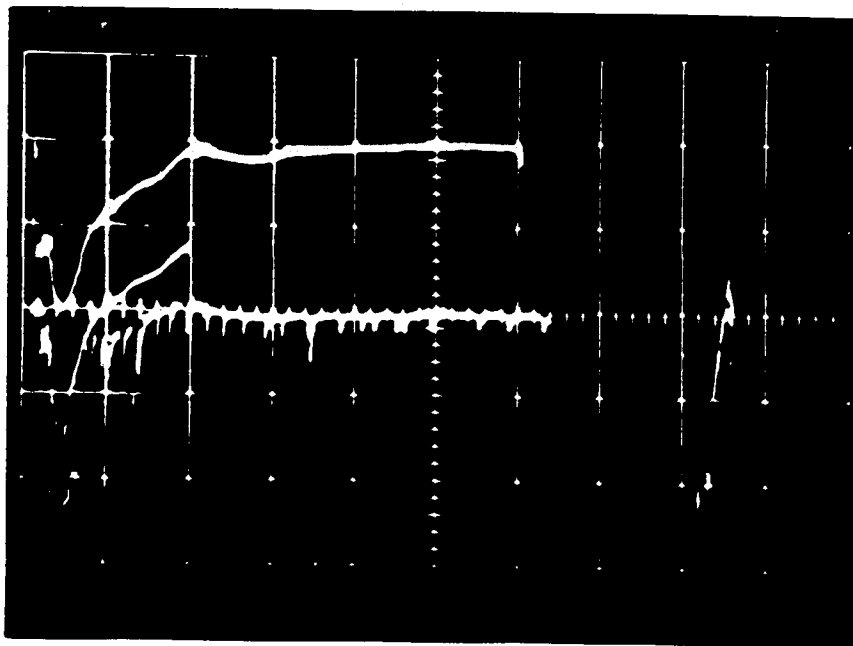
FIG. 6.5

FIG. 6.4   Oscilloscope traces of the currents flowing into a contaminated electrode. P_1=0.1 mmHg, V_c=2.5 KV and the negative and positive electrode positions = 70 cm and 140 cm from the driver, respectively. Vertical and horizontal deflections = 0.2 A/div. and 20 μsec/div. Time runs from left to right. Upper beam: V_d=80 V, middle beam: V_d=70 V and lower beam: V_d=50 V.

FIG. 6.5   The change of the electrode current with different degree of contamination. V_d=400 V. Vertical and horizontal deflections = 10 mA/div. and 20 μsec/div. Upper beam: clean electrodes, middle beam: lightly contaminated electrodes (after 2 shots without cleaning) and lower beam: heavily contaminated electrodes (after 10 shots without cleaning).

FIG. 6.6   Pre-breakdown V-I characteristics.

A.   Stages 1, 2 and 3 can be
clearly distinguished.

Stage 1: V-I_p curve follows
the probe theory.

Stage 2:   Electron avalanches
increase the electrode current.

Stage 3: I_p is mainly dominated
by external circuit.
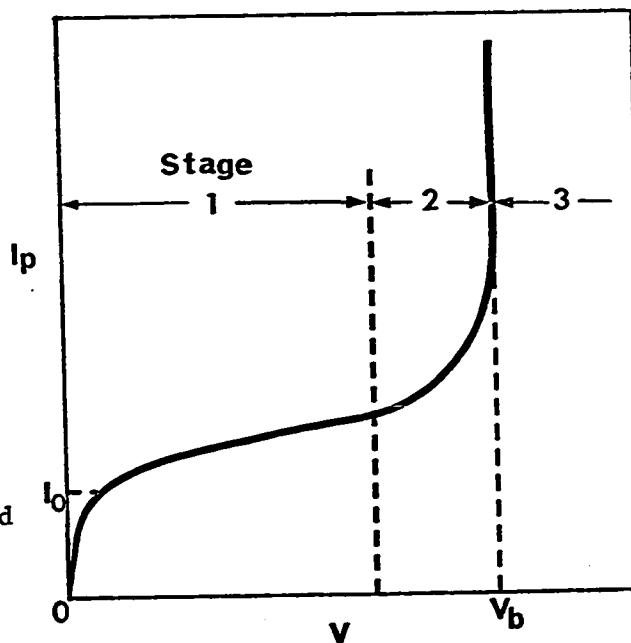
B.   Stage 2 cannot be observed,
or hidden by an experimental
error.

FIG. 6.7   Oscilloscope traces of electrode current with various values of electrode bias voltages. P_1=1 mmHg, V_C=2.5 KV and z=111 cm. The precursor plasma (6.5) was tested.
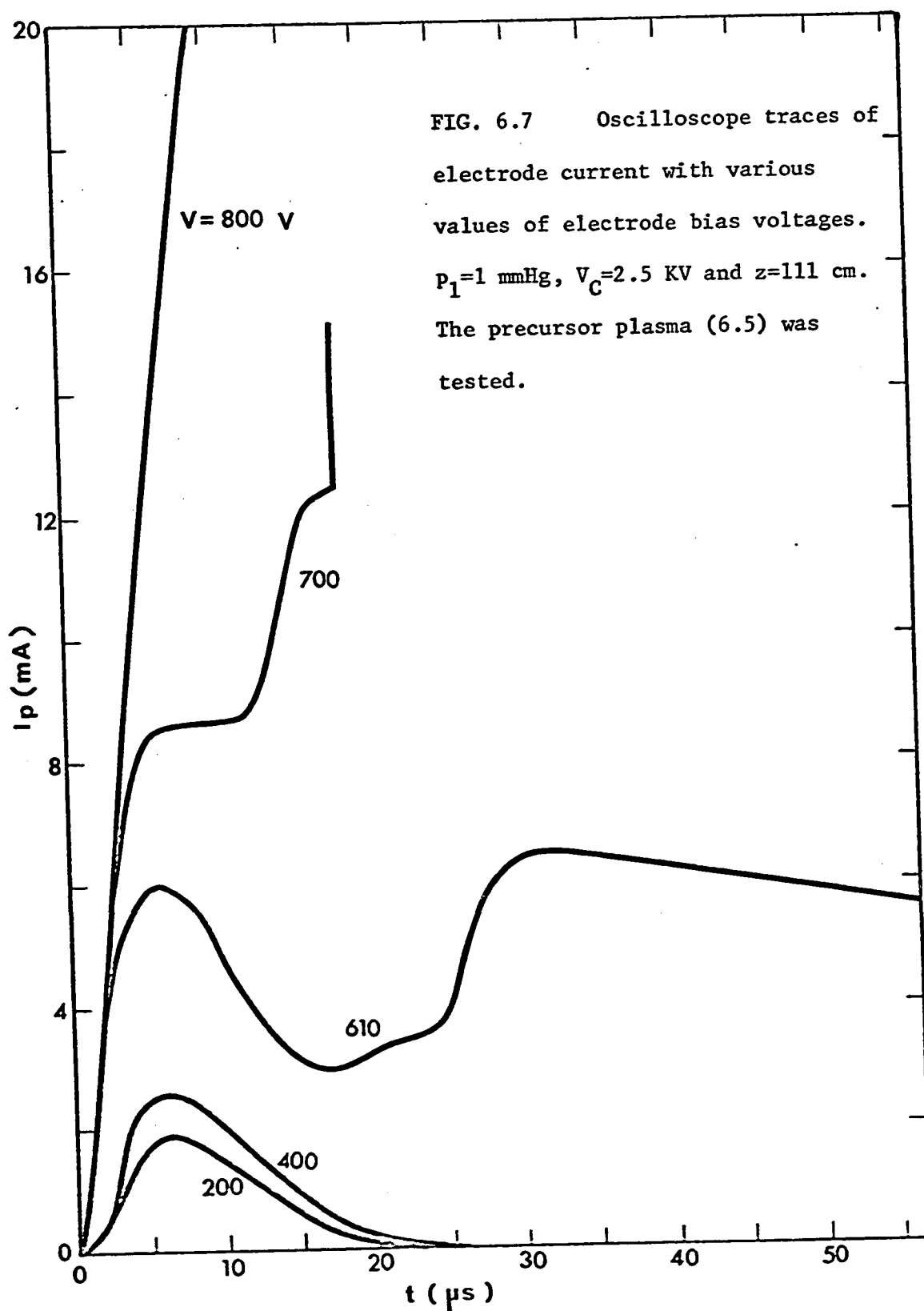
within 1 μsec and changes its density as shown approximately in the

V=200 volts wave form, where the electrodes were working as floating double

probes. The current gradually increases with increasing V and when V=610 V,

a large secondary process occurs with a time lag of 24 μsec (6.6) from the

time of the first peak current (at 6 μsec). At this time (V=610 V, t=30 μs),

the relation of $\gamma \int_{r_p}^{r_s} \alpha dr = 1$ holds, since I/I_0 approaches infinity, where I_0

is the current when electron avalanche effect can be negligible. With

higher V, I goes to infinity with a certain time lag, depending on the

magnitude of overvoltage and the plasma density.

An approximate theory expressing the relation of I and V will be

presented when the ionizing effect in the sheath by secondary electrons

is considerable. Since V is applied across the cathode sheath, I can be

considered as a current flowing between concentric cylindrical electrodes

with inner and outer electrode radii of r_p (electrode radius) and r_s (sheath

radius), respectively. I can be expressed as,

$$I = \frac{I_e \, e^{\int_{r_p}^{r_s} \alpha dr}}{1 - \gamma \left(e^{\int_{r_p}^{r_s} \alpha dr} - 1 \right)} \tag{6.1}$$

where
$$\int_{r_p}^{r_s} \alpha dr = \frac{AV}{B \ln \frac{r_s}{r_p}} \left(e^{-\frac{B p r_p \ln \frac{r_s}{r_p}}{V}} - e^{-\frac{B p r_s \ln \frac{r_s}{r_p}}{V}} \right) \tag{6.2}$$

(6.5) The precursor plasma in our shock tube is produced mainly by the photoionization by the intense radiation of the arc discharge in the driver. This precursor plasma has a high velocity (10-100 times the velocity of the shock produced plasma), a low density (10^9-10^{12} cm^{-3}) and a slow density decay along the axis of the shock tube (- 10 times the decay time of the shock produced plasma).
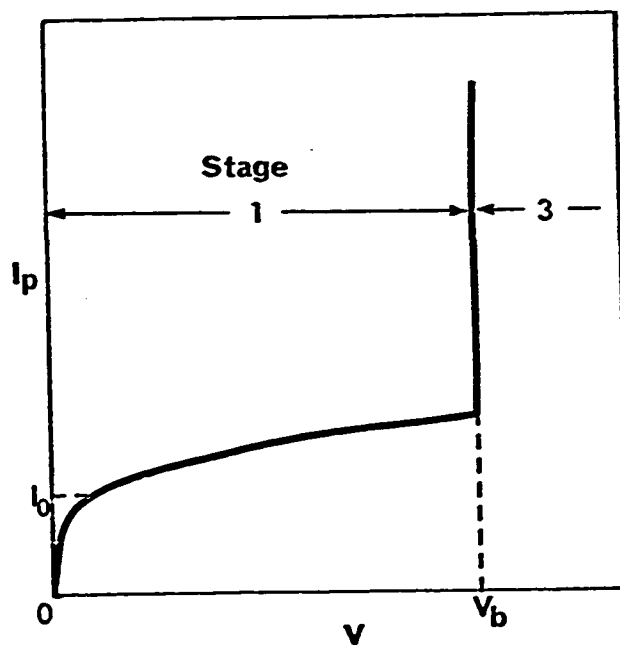
(6.6) When the breakdown voltage was measured with shock produced plasma, the breakdown occured at or before the density peak arrives at the electrode. The time lag mentioned here was observed only in the case of precursor plasma. This may be due to the incomplete surface layer cleaning by ion sputtering.

and I_e is the initially emitted electron current from the cathode. Here

$$\frac{\alpha}{p} = A e^{-\frac{Bp}{E}} \quad \text{and} \quad E(r) = \frac{V}{r \ln \frac{r_s}{r_p}} \qquad (6.3)$$

were employed. Also it was assumed that the field perturbation by space charge was negligible. Equation 6.1 was computed with $A=13.6 \text{ cm}^{-1} \text{mmHg}^{-1}$, $B=235 \text{ V/cm} \cdot \text{mmHg}$ (5.2), $r_p=0.05$ mm, $r_s=0.01-100$ cm, $V=0-2000$ V and $p=0.01-100$ mmHg and the results presented in Figs. 6.8 and 6.9. From Fig. 6.8 we can see that I/I_e becomes a maximum at a certain combination of p and r_s given by

$$\frac{V}{p(r_s-r_p)} = B = \text{constant}. \qquad (6.4)$$

At small r_s in Fig. 6.9, $\exp(\int_{r_p}^{r_s} \alpha dr)$ does not reach the value of $1+1/\gamma$ (i.e., breakdown) even with $V=\infty$. However, at large V, the electric field at the electrode surface becomes very intense and electron field emission begins to take place which leads to the voltage collapse in the sheath. In this case of field emission, stage (2) in Fig. 6.6-A will never be observed, since the field emission current is a very strong function of electric field and so V-I curve takes the form of Fig. 6.6-B. In other words, V-I curve is of type Fig. 6.6-A when p is large and/or r_s is large (n_e is small) and of type Fig. 6.6-B when p is small and/or r_s is small (n_e is large).

In our experiments V was kept constant, while n_e was increased with respect to time, i.e., r_s was decreased. In this case, too, I-r_s curves experience qualitatively the same curves as shown in Figs. 6.6-A and B. These two types of the current change, observed in the experiments at various values of p and n_e, were in good correspondense with the theory. Fig. 6.7 belongs to the Fig. 6.6-A type. In most of the cases, however, the type of Fig. 6.6-B was observed.

FIG. 6.8   Pre-breakdown current of Eq. 6.2.

V=200 V and r_p=0.05 mm.

FIG. 6.9 Pre-breakdown current of Eq.
6.2. p=0.1 mmHg and r_p=0.05 mm.
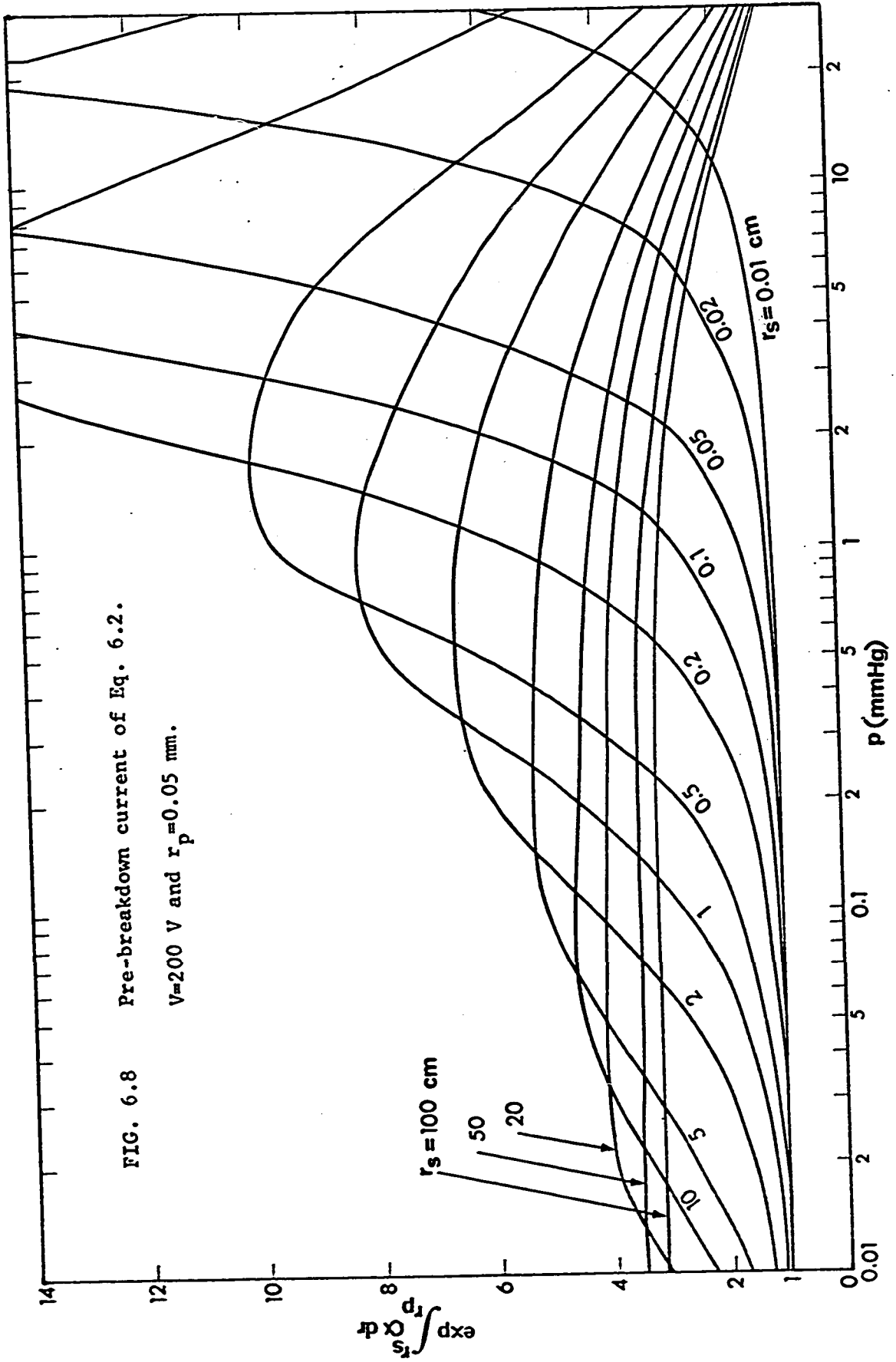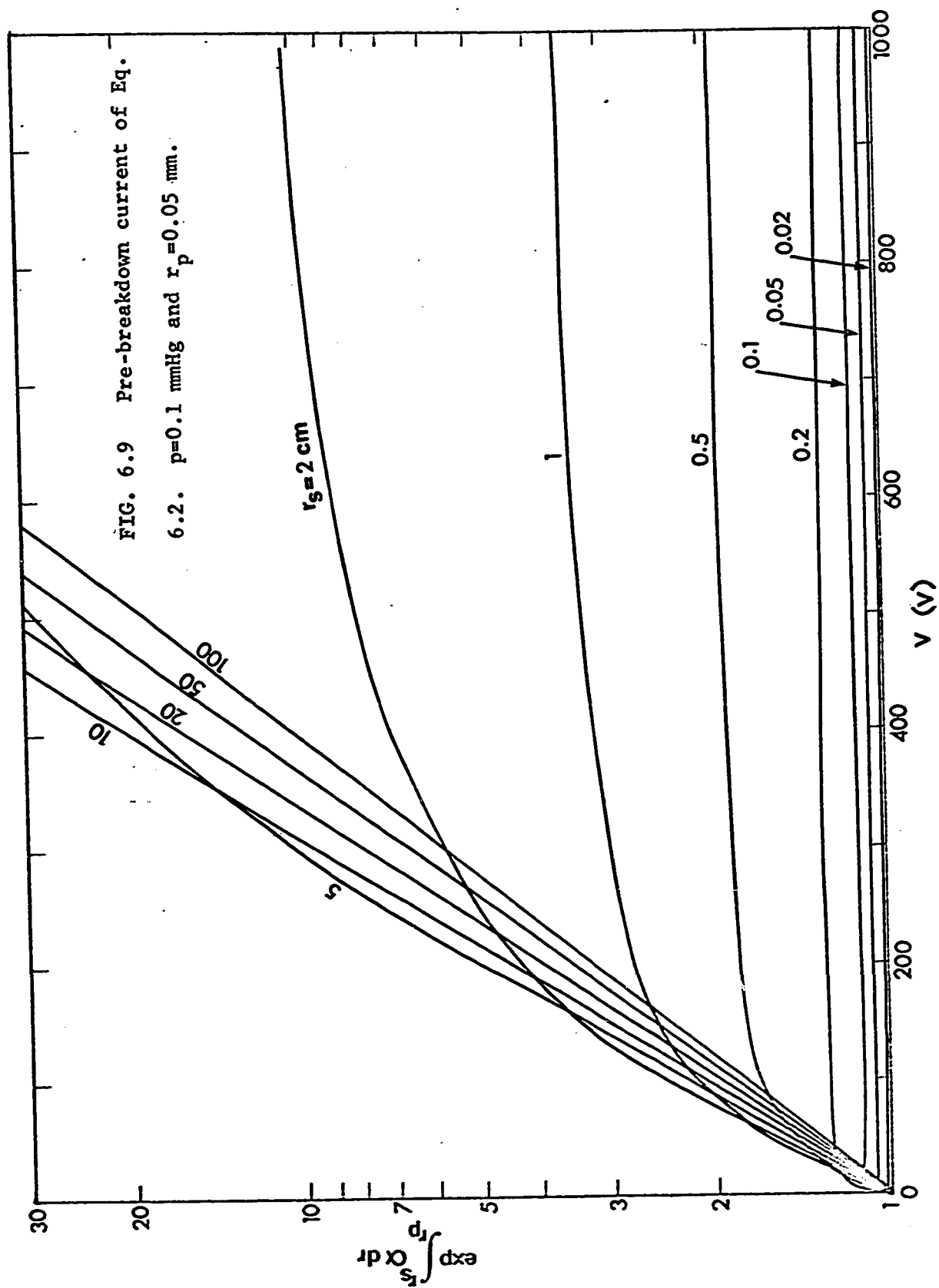
6.5 MEASUREMENTS OF BREAKDOWN VOLTAGE vs ELECTRODE SEPARATION

According to the floating probe theory mentioned before, it is shown that

$$V_1 = V_d + V_f - V_c \qquad (6.5)$$

at sufficiently large V_d (Sec. 2.7). If V_d is increased, then only V_1 is increased while V_2 and V_c stay constant. Therefore the breakdown should always occur in the sheath of the negative electrode no matter what the positive electrode condition is.

To examine this statement the breakdown voltage was measured with cathode set stationary while the anode was moved along the shock tube axis. Under these conditions the plasma density and the temperature at the anode decreased as it was moved away from the shock driver.

The measurements were carried out with the initial pressure of the shock tube of 0.15 mmHg in argon and with the cathode kept at a distance of 100 cm from the driver, where the plasma density was 2.5×10^{12} cm^{-3}. By increasing V_d while observing the change in electrode current, the breakdown voltage was measured as a function of electrode separation, with the results shown in Fig. 6.10. From the figure it is evident that the breakdown voltage was always constant and independent of the electrode separation and anode condition. In the figure the breakdown voltage in the absense of plasma is also plotted. On the other hand, when the cathode was moved, the breakdown voltage showed a change depending on the plasma density, etc. at the cathode. These facts clearly show that the breakdown took place at the cathode.

When the electrical conductivity of the plasma becomes low, there exists a voltage drop in the plasma and V_1 is decreased by some amount.

FIG. 6.10   Breakdown voltage (V_b) vs electrode separation (d) with and without surrounding plasma.

$n_e = 0$

$n_e = 2.5 \times 10^{12} \, cm^{-3}$
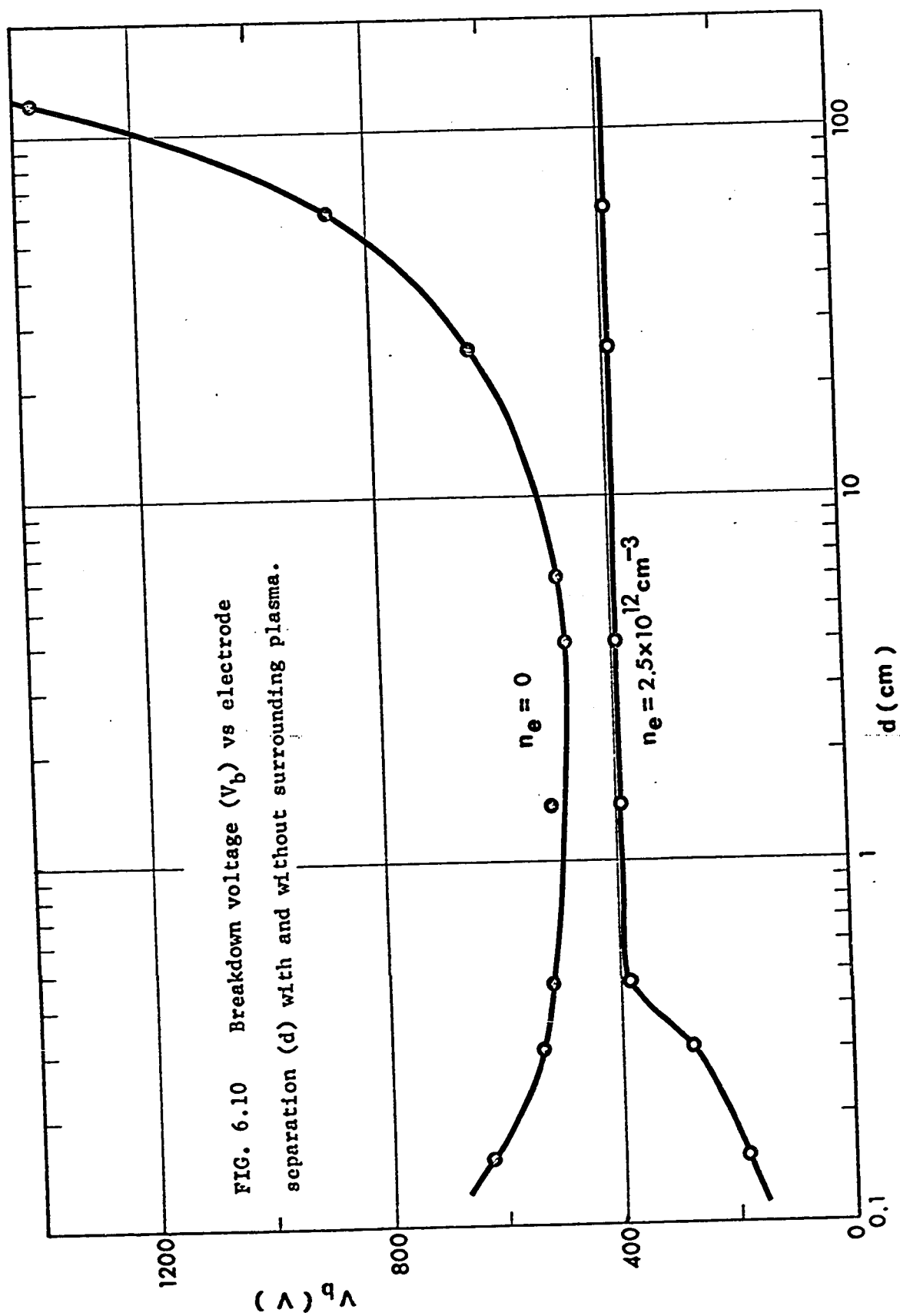
Let us examine this effect by taking the example of the severest case, as,

α (degree of ionization) = 10^{-6},

T_e = 1000 K,

Q_e = 3×10^{-21} m^2 (Fig. 2.1)

and n_e = 10^{11} cm^{-3},

then from Eq. 2.5 the plasma conductivity becomes,

σ = 40 mhos/m.

If the electrode distance is 10 cm and the effective cross section of the plasma cylinder is 10 cm^2, then the resistance of the plasma between two electrodes is,

R = 2.5 Ω.

With the electrode current of 0.1 amperes the voltage drop is only 0.25 volts, which can be neglected.

6.6 MEASUREMENTS OF BREAKDOWN VOLTAGE vs PLASMA DENSITY

Breakdown voltages between two electrodes were measured at various plasma and neutral densities. Electrode currents at the same ambient conditions as well as the plasma velocities were also measured to facilitate the calculation of the plasma and neutral densities (Sec. 7.2). The electrode current variation with respect to applied voltage at various shock driver conditions is shown in Fig. 6.11. The breakdown voltage against plasma density at initial pressures of 0.1, 1 and 10 mmHg in argon is also shown in Fig. 6.12 (see Table 7.1).

It should be noted that in Figs. 6.11 and 6.12, V_b decreases to a value much lower than the Paschen minimum voltage in Sec. 6.1 and Eq. 5.27

FIG. 6.11 Electrode current-voltage characteristics for the breakdown voltage measurements at various z and V_C. $p_1=0.15$ mmHg. The numbers in the parentheses indicate the breakdown voltages.

FIG. 6.12 Breakdown voltage (V_b) vs plasma density (n_e) at various initial pressures (p_1). When $n_e=0$, $V_b=620$, 380 and 550 volts at $p_1=0.1$, 1 and 10 mmHg, respectively.
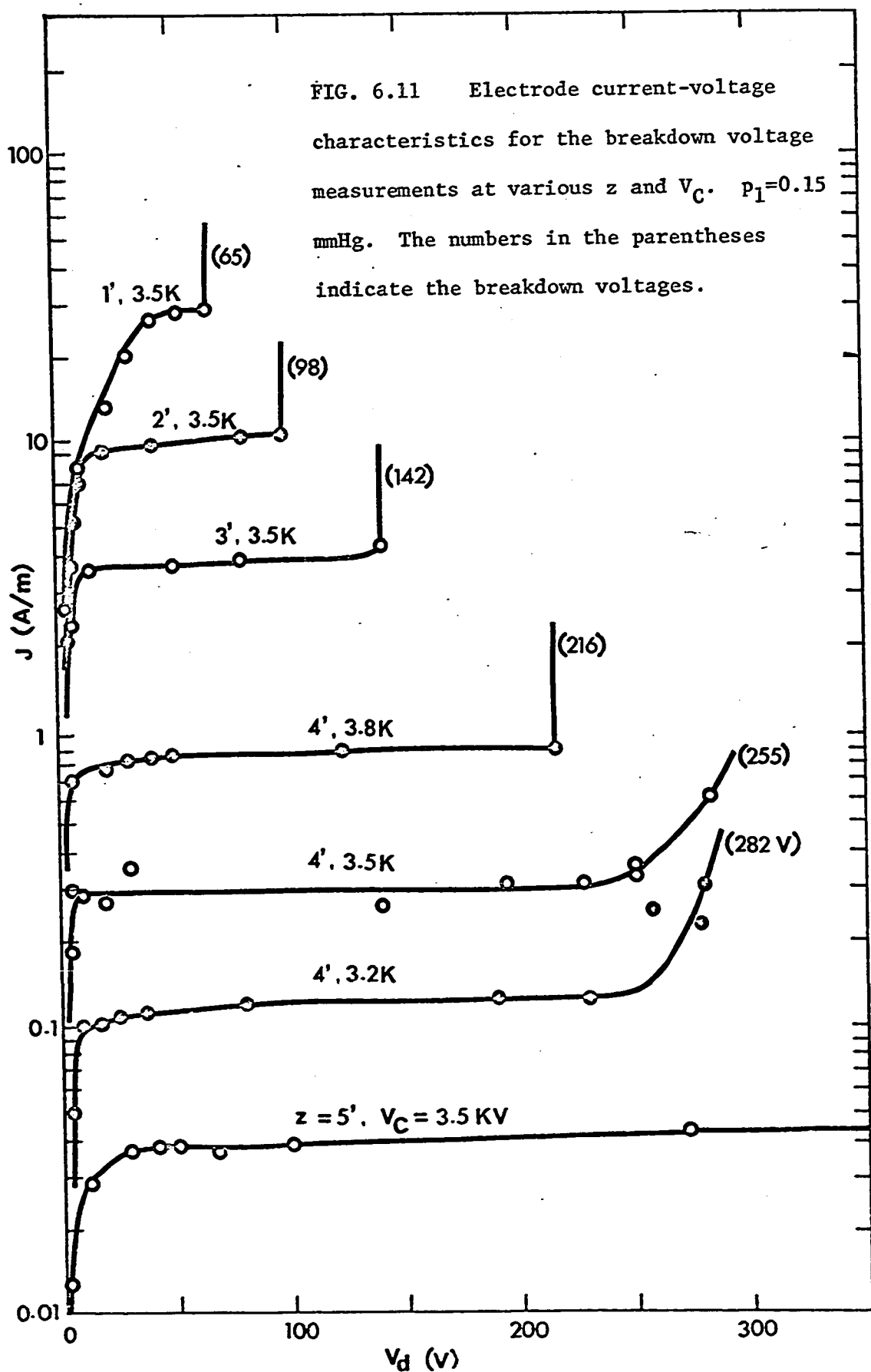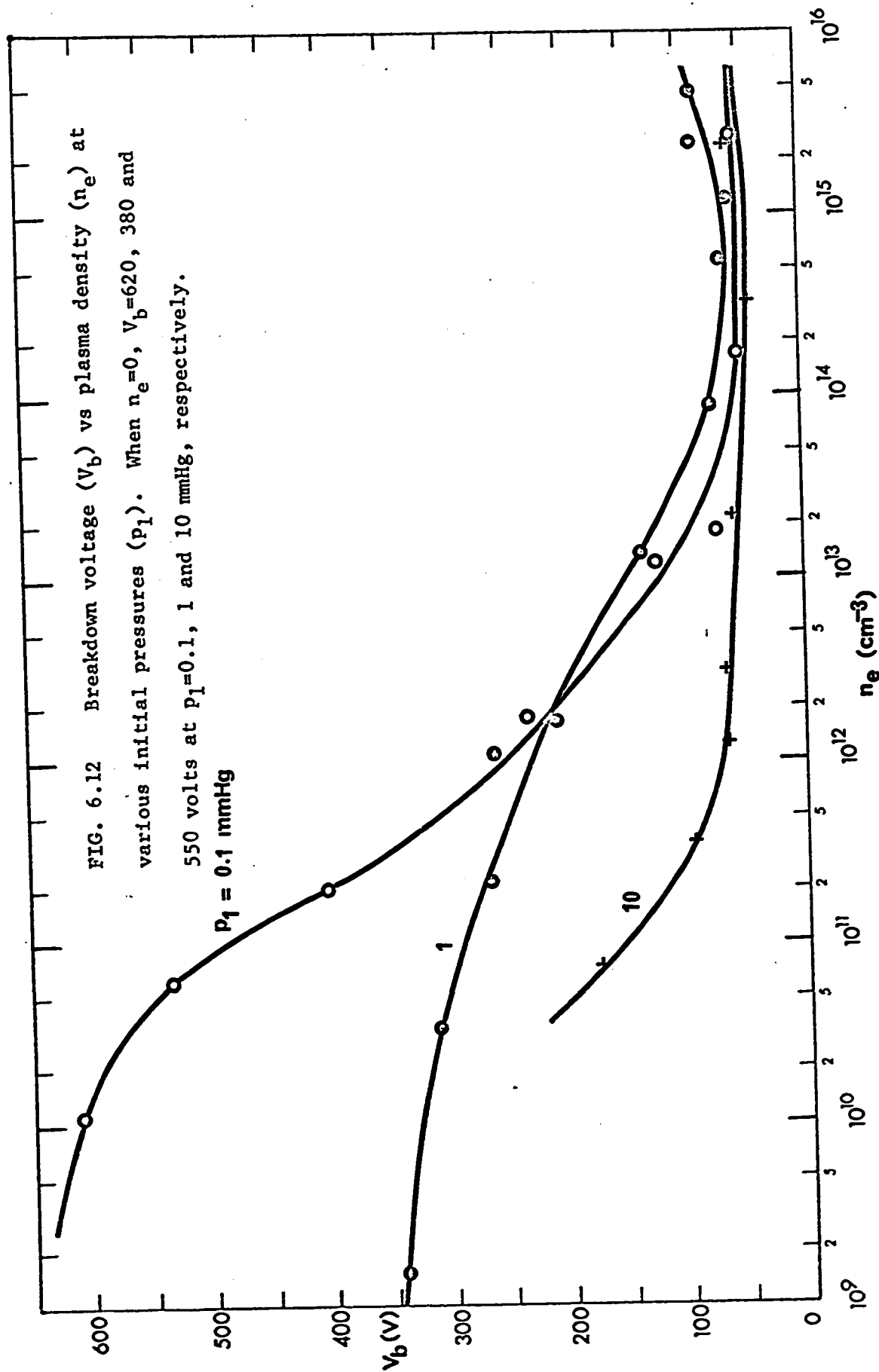
of V_{mm}=200 volts. This shows that the breakdown phenomena is not as simple as the breakdown in a neutral gas. The surrounding plasma is causing a large influence on the breakdown voltage.

The shot-to-shot method was used for the voltage and current measurements. The reproducibility was sometimes not very good. After some trials, however, it was found that if the data was interpreted as a function of time after firing the driver, instead of as a function of axial position of the shock tube, the reproducibility was fair to good. This indicated that d/dt of the plasma properties (e.g. recombination, ambipolar diffusion) was quite reproducible while $v(\partial/\partial t)$ of the plasma properties (e.g. heating the oncoming neutrals by the shock, frictional force between the wall and plasmoid) was not. Therefore the data was taken as a function of time, and then normalized into a function of axial distance whenever necessary.

6.7 EFFECT OF THE ELECTRODE EDGE ON THE BREAKDOWN EXPERIMENTS

With our electrode configuration there was a limit to measurements of the breakdown voltage. Since the electrodes used here traversed the shock tube as seen in Fig. 3.3, the tip of the electrode obviously measured the highest plasma density, while the bottom part of the electrode measured somewhat lower plasma density. This density variation can be approximated by (Eq. 2.30),

$$n_e(R) = n_e(0) \, J_0 \left(2.405 \frac{R}{R_0}\right),$$

(6.6)

where R_0 is the shock tube radius and J_0 is the Bessel function of 0th

order of the first kind.

In Fig. 6.13 are shown the V_b-n_e curves which would have been measured at various positions of the cathode if we could have separated the cathode into small segments. For instance at R=0 (cathode tip), V_b follows the curve F - E - C as n_e is increased from zero, coinciding with the Paschen curve of Eq. 5.24. With higher n_e, electron emission from the cathode becomes dominant over electron creation by collision and V_b becomes smaller again, as C - B - A. However, at the density of n_c, for instance, V_b at the position of R=R_c on the cathode is only V_{min} and so all we can detect as a breakdown voltage is V_{min}, not V_c. Consequently if the plasma density is increased gradually, measured V_b changes along the thick line as F - E - D - B - A. The E - C - B curve can never be observed.

FIG. 6.13   The breakdown voltage at various positions of the cathode as a function of plasma density. R=0 at the cathode tip and R=R$_0$ at the cathode bottom (R$_0$ is the radius of the shock tube). Measured V$_b$ changes as A-B-D-E-F as n$_e$ is decreased.
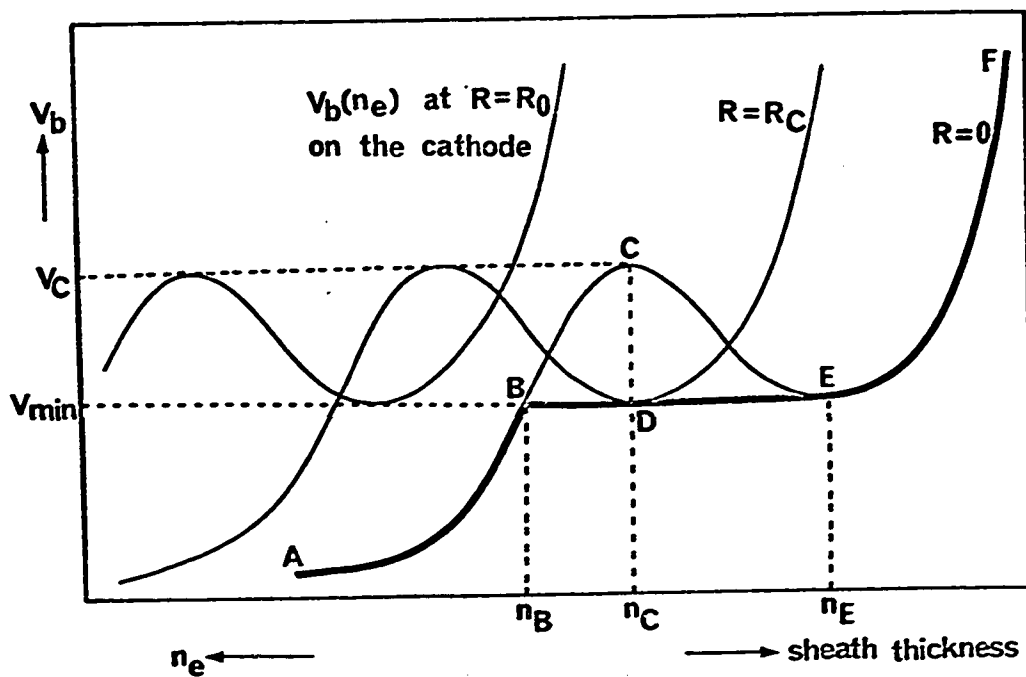
CHAPTER VII   DISCUSSIONS ON THE BREAKDOWN THEORY AND EXPERIMENTS

7.1   PROPOSED MODEL OF THE BREAKDOWN MECHANISM

By having checked all the theoretical possibilities which the author could have thought of on the breakdown mechanism and by having done many experimental investigations, the most likely mechanism of the breakdown between the electrodes immersed in a plasma is now proposed.

THE MODEL OF THE BREAKDOWN MECHANISM: There are two independent kinds of mechanisms for the breakdown between two electrodes in a plasma; one is the "Cold cathode arc discharge" and the other is the "Spark discharge".
(1)   Cold cathode arc discharge takes place at relatively high plasma densities.   A very thin sheath is formed around the cathode due to the high plasma density and low ionic mobility.   Also the current enhancement by the ionizing effect of electrons inside the sheath causes the reduction of the sheath thickness.   Because of the thin sheath thus created the electric field at the cathode surface becomes strong enough to cause electron ejection by field emission, which triggers the discharge.   After the triggering the current is concentrated into a small area of the cathode and, due to its local heating, thermionic electrons dominate the field electrons as a main current source for the full path breakdown.
(2)   Spark discharge occurs at lower plasma densities.   The secondary electrons emitted from the cathode ionize neutral particles in the cathode sheath and this ionization causes the instability of the electrode system.

When the anode is contained in the sheath, the breakdown mechanism is similar to that for zero plasma density (which is the extreme case in which the sheath is infinitely large), except that due to the space charge accumulation first ionization coefficient becomes larger and the breakdown voltage decreases.

In the following part of this section the equations which should be used in executing the proposed models will be listed. For the investigation of the cold cathode arc mechanism, the following equations and figures should be employed:

(1) Applied voltage across the cathode sheath

V_f: Eqs. 5.1-5.7

V_p: Eqs. 2.83-2.106, Fig. 2.5

(2) Ionic mobility near the cathode

μ_i: Eq. 5.85

n: Fig. 4.2, Eqs. 5.88 and 5.110

T: Fig. 4.4, Eq. 5.90

(3) Cathode sheath and electrical boundary layer thickness

r_s: Eqs. 5.52, 5.53, 5.56, 5.57, 5.63, 5.64, 5.65 and 5.66

r_a: Eq. 5.41

(4) Effective current in the sheath

η(charge accumulation): Sec. 5.3.5

G: Eqs. 5.46, 5.55, 5.60, 5.61 and 5.62

Q_i: Fig. 5.1

(5) Electric field at the cathode surface

E_p: Eqs. 5.52, 5.56, 5.63 and 5.66

β(field enhancement factor by surface irregularities): Secs. 5.3.2 and 6.2, Eq. 5.114

ε(field enhancement factor by stagnation): Sec. 5.14, Eqs. 5.36, 5.37 and 5.40.

(6) Field emission current

  j: Eq. 5.111

(7) Cathode spot temperature by local heating

  T: Eqs. 5.140 and 5.141

(8) Thermionic electron emission current

  j: Eq. 5.119

(9) Self sustaining arc discharge

  Eqs. 5.120-5.134.

As there is no collision between ions and electrons in the sheath (Sec. 5.1.8), the ion density in the sheath is not decreased due to the boundary layer effect although its temperature is decreased. This effect, therefore, need not be considered.

For the spark discharge, G and r_s are given by Eqs. 5.55-5.57 and Fig. 5.2. In the figure, if $V_p/r_p E_m$ becomes large and d/r_p becomes close enough to its final value, then even a very small perturbation to the sheath thickness can lead the system to the breakdown (i.e., $G=1$); therefore this is the condition for breakdown. If r_s becomes larger than the inter-electrode separation, then the modified form of Eqs. 5.22-5.24 should be used. (There is a change in potential distribution due to the formation of sheath.) In our experimental conditions, however, r_s is much smaller than the spark discharge criterion and the discussion on these mechanisms will not be conducted any further.

7.2   COMPARISON OF THE BREAKDOWN MODEL WITH THE EXPERIMENTAL RESULTS

In this section the experimentally obtained values will be examined

according to the model theory of the previous section. If the sheath
thickness is small for the spark discharge criterion, then the electric
field at the cathode surface should be strong enough to cause field emission,
or in other words the applied field at the cathode surface should be
$2\text{-}4\times10^5$ V/cm (Secs. 5.3.1, 5.3.2 and 6.2). Therefore the intensity of the
electric field at the cathode surface will also be calculated.

In Table 7.1 the experimentally obtained values of M, J_i, V_b and many
other calculated values are listed. (n_e vs V_b curve is shown in Fig. 6.12.)
The relation of $\lambda_{iw}\ll d\ll\lambda_{ew}$ in the table implies that, in the sheath, the
ions are collision dominated while electrons are not. For the ion saturation
current to the electrode, collision dominated theory, especially Eq. 2.74
should be used since $R_E\alpha^2\chi^2\gg1$ (not listed). For the floating potential
of electrodes, the argument of Sec. 5.1.1 is correct. $\lambda_{iw}\ll\delta_E$ is an
important relation, which indicates that Navier-Stokes equation is
applicable to our case and the boundary layer is formed around the electrode.
In all the cases $G_a\ll1$ and also $1/1\text{-}\gamma\zeta\simeq1$ (not listed) show that the
ionization effect in the ambipolar diffusion region as well as that outside
the ambipolar diffusion and sheath regions is negligible.

E_{p2} and d_2/r_p are obtained with the assumptions that the boundary
layer effect is totally negligible, i.e., $\delta_E\ll\lambda_{iw}$ and $\delta_E\ll d$. On the other
hand E_{pw} and d_w/r_p are obtained with the assumptions that the boundary
layer effect is dominating, i.e., $\delta_E\gg\lambda_{iw}$ and $\delta_E\gg d$. From the table it
can be found that $\delta_E\gg\lambda_{iw}$ and $\delta_E\simeq d$, which means that E_{pw} and d_w are
more correct than E_{p2} and d_2. Especially for the calculation of E_p, the
assumption of $\delta_E\gg d$ is not very significant to the value of E_p, since the
Poisson's equation was integrated in the cathode region and also the
charge density is the largest at the cathode surface (Eq. 5.48). However,

TABLE 7.1 Calculation of the electric field at the cathode surface

Experimental and calculated results according to Sec. 7.1 are listed here.
The notations used are:

P_1 = initial pressure in the shock tube

z = axial distance from the driver mouth

V_C = capacitor bank charging voltage

M = u_2/c_1 = normalized plasma velocity

t_{arr} = arrival time of plasmoid at the electrodes

J_i = electrode current just before the breakdown (7.1)

V_b = breakdown voltage

n_2/n_0 = the ratio of the neutral particle density in the incident shock
to the neutral density at 1 mmHg and 0 C ($n_0 = 3.22 \times 10^{22}$ m^{-3}).

n_w/n_0 = the ratio of the neutral particle density near the cathode
to the neutral density at 1 mmHg and 0 C

λ_{iw} = ionic mean free path near the cathode

λ_{ew} = electron mean free path near the cathode

R_E = electrical Reynold's number

δ_E/r_p = the ratio of the thickness of electrical boundary layer to
the electrode radius

G_a = ionizing effect in the ambipolar diffusion (Eq. 5.62)

n_e = electron density in the incident shock

T_e = electron temperature in the incident shock

σ = electrical conductivity in the incident shock

E_{p2} = electric field at the cathode surface when $r_s \gg r_a$ (Eq. 5.56)

d_2/r_p = ratio of the sheath thickness to the electrode radius

when $r_s \gg r_a$ (Eqs. 5.55-5.57)

E_{pw} = electric field at the cathode surface when $r_a \gg r_s$ (Eq. 5.56

with G and suffix 2 changed to $G_s + G_a$ and suffix w, respectively)

d_w/r_p = ratio of the sheath thickness to the electrode radius

when $r_s \gg r_a$ (Eqs. 5.55-5.57 with G and suffix 2 changed to

$G_s + G_a$ and suffix w, respectively).

(7.1) "Just before the breakdown" means that the current at the end of stage (1) of Figs. 6.6-A and B. In most of the experiments, the V-I characteristics were of type B and J_i could be measured clearly.

TABLE 7.1 - cont'd.

case	P1 (mmHg)	z (ft)	V_C (KV)	M	t_{arr} (us)	J_i (A/m)	V_b (V)
1	0.1	3	1.6	6.2	300	0.025	610
2	"	5	2.9	9.4	280	0.1	530
3	"	5	3.2	15.5	250	0.25	400
4	"	3	1.7	7.7	240	0.7	230
5	"	3	2.0	9.3	170	2.5	125
6	"	3	3.1	25	150	4	70
7	"	1	1.5	28	80	20	50
8	"	1	4.0	31	38	200	55
9	1	3	1.5	2.5	900	0.0015	340
10	"	3	2.3	4.7	800	0.02	310
11	"	3	3.0	9.4	480	0.1	265
12	"	1	1.3	3.1	340	0.2	260
13	"	3	4.2	15.5	260	0.5	207
14	"	1	1.5	3.1	250	1	135
15	"	1	2.1	9.4	131	5	75
16	"	1	2.5	12	120	20	65
17	"	1	2.8	14	96	40	60
18	"	1	3.5	22	85	100	95
19	"	1	4.5	31	68	200	90
20	10	1	2.5	1	260	0.00667	175
21	"	1	2.9	1	220	0.0166	95
22	"	1	3.2	2.1	250	0.05	65
23	"	1	3.3	2.1	300	0.1	65
24	"	1	3.5	2.65	260	0.5	60
25	"	0	2.8	7.2	62	5	40
26	"	0	4.0	9.35	50	30	60

TABLE 7.1 - cont'd.

case	$\frac{n_2}{n_0}$	$\frac{n_w}{n_0}$	λ_{iw} (m)	λ_{ew} (m)	Re	$\frac{\delta_E}{r_p}$	Ga
1	0.39	22.3	3.77×10^{-6}	17.9×10^{-5}	5.10	0.887	1.11×10^{-2}
2	0.56	43.7	1.92 "	9.15 "	9.47	0.650	1.26 "
3	1.02	98.1	0.856 "	4.08 "	25.8	0.394	1.47 "
4	0.46	33.5	2.51 "	11.9 "	6.57	0.780	1.22 "
5	0.56	45.1	1.86 "	8.87 "	9.18	0.660	1.29 "
6	1.47	175.7	0.478 "	2.28 "	54.1	0.272	1.54 "
7	1.51	196.4	0.428 "	2.04 "	59.2	0.260	1.54 "
8	0.40	230	0.365 "	1.74 "	5.31	0.868	3.06 "
9	3.2	131	0.643×10^{-6}	3.07×10^{-5}	30.2	0.364	2.11×10^{-2}
10	3.8	198	0.424 "	2.02 "	46.9	0.292	3.11 "
11	5.3	454.7	0.185 "	0.880 "	85.7	0.216	4.07 "
12	3.4	148	0.570 "	2.71 "	42.7	0.306	1.87 "
13	9.0	983	0.0855 "	0.407 "	211	0.138	4.68 "
14	3.4	148	0.570 "	2.71 "	42.7	0.306	1.87 "
15	5.3	454.7	0.185 "	0.880 "	85.7	0.216	4.07 "
16	6.9	663.4	0.127 "	0.603 "	133	0.173	4.38 "
17	8.2	852.4	0.0985 "	0.469 "	178	0.150	4.58 "
18	12.2	1554	0.0541 "	0.257 "	379	0.103	4.89 "
19	12.4	2256	0.0372 "	0.177 "	453	0.094	4.92 "
20	23	617	0.136×10^{-6}	0.649×10^{-5}	157	0.160	2.23×10^{-2}
21	23	617	0.136 "	0.649 "	157	0.160	2.23 "
22	31	1200	0.0702 "	0.334 "	320	0.112	4.66 "
23	31	1200	0.0702 "	0.334 "	320	0.112	4.66 "
24	33	1380	0.0610 "	0.290 "	352	0.107	6.16 "
25	41	2982	0.0282 "	0.134 "	548	0.0854	11.9 "
26	50	4680	0.0179 "	0.0855 "	767	0.0722	13.1 "

TABLE 7.1 - cont'd.

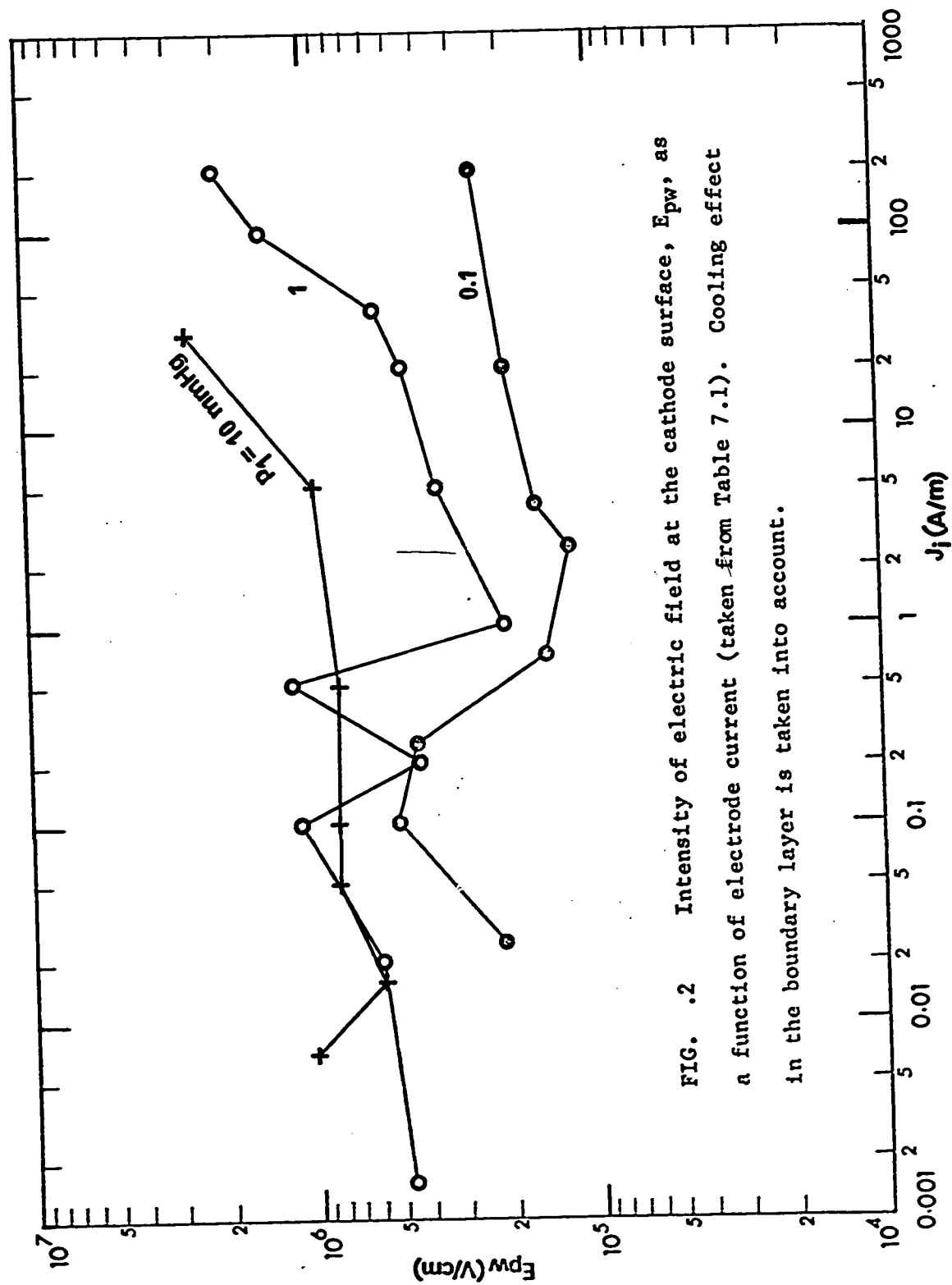| case	n_e (m^{-3})	T_e (°K)	σ (moh/m)	E_{p2} (V/m)	$\frac{d_2}{r_p}$	E_{pw} (V/m)	$\frac{d_w}{r_p}$
1	1.11×10^{16}	0.66×10^4	1.18×10	5.30×10^6	38	2.12×10^7	2.3
2	6.15 "	0.90 "	2.46 "	5.92 "	15.7	4.91 "	1.3
3	1.93×10^{17}	1.11 "	3.01 "	6.18 "	7.0	4.28 "	0.53
4	1.67×10^{18}	0.84 "	5.78×10^2	4.59 "	4.6	1.50 "	1.3
5	1.19×10^{19}	0.93 "	1.42×10^3	4.48 "	1.8	1.24 "	0.67
6	1.83 "	1.83 "	0.942 "	5.47 "	0.68	1.55 "	0.235
7	1.75×10^{20}	1.50 "	2.72 "	7.75 "	0.32	2.01 "	0.116
8	2.53×10^{21}	2.0 "	4.32 "	12.9 "	0.21	2.49 "	0.0145
9	1.61×10^{15}	0.6 "	2.59×10^{-1}	4.01×10^6	20	4.86×10^7	0.44
10	3.42×10^{16}	0.6 "	4.60	4.45 "	9.8	6.06 "	0.265
11	2.10×10^{17}	0.99 "	7.65	5.60 "	4.2	11.3 "	0.13
12	1.06×10^{18}	0.6 "	1.35×10^2	5.10 "	5.0	4.15 "	0.37
13	1.56 "	1.26 "	2.16×10	7.53 "	1.68	10.7 "	0.06
14	1.40×10^{19}	0.6 "	6.81×10^2	4.83 "	1.88	2.10 "	0.36
15	8.93 "	0.99 "	1.29×10^3	8.23 "	0.46	3.52 "	0.11
16	5.42×10^{20}	1.11 "	2.25 "	13.2 "	0.24	4.55 "	0.072
17	1.32×10^{21}	1.2 "	2.85 "	16.9 "	0.167	5.7 "	0.052
18	2.49 "	1.47 "	3.57 "	31.6 "	0.142	14.1 "	0.032
19	4.77 "	2.1 "	5.22 "	42.7 "	0.10	20.8 "	0.022
20	7.30×10^{16}	0.6×10^4	1.63	5.85×10^6	2.4	10.8×10^7	0.09
21	3.67×10^{17}	0.6 "	8.13	3.22 "	2.3	5.93 "	0.09
22	1.21×10^{18}	0.6 "	1.96×10	3.16 "	1.3	8.43 "	0.047
23	3.04 "	0.6 "	4.78 "	3.68 "	1.08	8.23 "	0.047
24	2.34×10^{19}	0.6 "	2.71×10^2	5.41 "	0.61	8.13 "	0.040
25	3.42×10^{20}	0.84 "	1.02×10^3	11.8 "	0.16	9.80 "	0.020
26	2.40×10^{21}	1.08 "	2.10 "	28.1 "	0.10	27.9 "	0.012

the invalid assumption of $\delta_E \ll \lambda_{iw}$ does affect the values of E_p significantly and E_{p2} gives smaller values than the true values. Therefore the values of E_{pw} can be regarded to be close to the true values. There is one defect in calculating E_{pw}; that is, E_{pw} has to be calculated with a few more steps than E_{p2}. Consequently E_{pw} might have large calculation errors. (An error of 30% in M gives 6% error to E_{p2} and 40% error to E_{pw}.)

In Figs. 7.1 and 7.2, E_{p2} and E_{pw} are shown as functions of electrode current. It can be understood that E_{pw} ($\simeq 5 \times 10^5$ V/cm) is not only sufficiently large for field emission of electrons (Secs. 6.2 and 7.4) but also is independent of the values of J_i and n_e over more than five orders of magnitude as well as of the values of initial pressure of 0.1- 10 mmHg. These facts strongly support the validity of the proposed model of the breakdown mechanism.

7.3   POST FIELD ELECTRON EMISSION PHENOMENA

When the field emission takes place at a particular spot (whose area is usually 10^{-14}-10^{-7} cm^2 because of the size of the surface irregularities, Sec. 5.3.2) the ions coming from the plasma tend to be concentrated into that spot in order to neutralize the electronic space charge. Also ions are produced near the area due to the ionization of neutral particles by field emitted electrons. These ionic effects increase the electric field at that spot. On the other hand, the emitted electrons form a double sheath around the emitted area (Sec. 5.1.7) which reduces the intensity of the field at the area. If, during the time electrons are emitted, the

FIG. 7.1   Electric field at the cathode surface, E_{p2}, taken from

Table 7.1. Cooling effect in the boundary layer is neglected.

FIG. .2   Intensity of electric field at the cathode surface, E_{pw}, as a function of electrode current (taken from Table 7.1). Cooling effect in the boundary layer is taken into account.
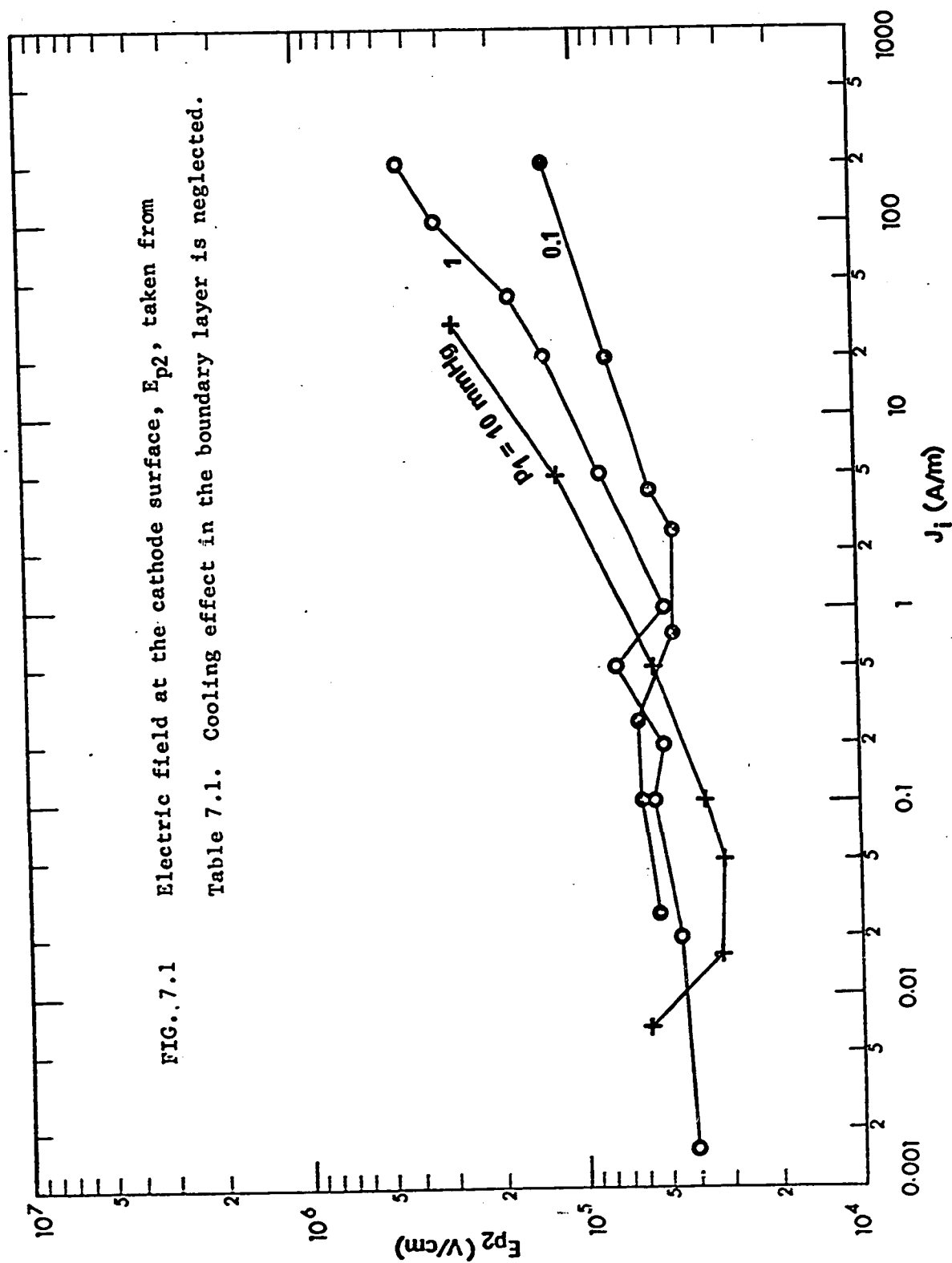
spot is heated enough by the bombardment of these energetic ions according to Eqs. 5.140 and 5.141, then the thermionic electrons can take the place of the field electrons even though the field electrons are suppressed by the double sheath after that period. Once a hot cathode spot is established, the stable self sustaining arc discharge is formed as mentioned in Sec. 5.4.3, and this arc discharge leads the electrode system to a full path breakdown.

7.4 COMPARISON OF THE RESULTS WITH EXISTING THEORIES AND EXPERIMENTS

Varney et. al. (7.2) as well as Crowe et. al.(7.3) carried out a one-dimensional analysis on the influence of the space charge on the spark discharge. In their calculations (Crowe) the space charge is so small that the cathode sheath extends much further than the anode. This means that the upper limit of the integral of the Poisson's equation is the anode position, not the cathode sheath edge. (Sec. 7.1, spark discharge) They have found that the influence of the space charge on the threshold voltage is negligible unless the initial current is significantly larger than 10^{-8} A/cm^2.

The cathode mechanism of extremely short arcs at atmospheric pressure $(\lambda_e \gg d)$ has been studied by Kisliuk, Boyle and others (7.4). They observed a breakdown voltage as low as 30 volts at small electrode separations of the order of 2000 Å. The phenomena are shown to be consistent with the hypothesis that (1) the arcs are initiated by field emission electrons, (2) after the initiation the anode material is evaporated by the secondary electrons and then ionized, and (3) the space charge thus formed enhances the electric field at the cathode, and increases

the field emission current until the breakdown occurs. Because of the steep increase in current with field, this process is able to build up to breakdown even when the probability of any particular electron having an ionizing collision is extremely small.

Their case is very similar to ours, i.e., breakdown is triggered by field emission electrons, which modifie the potential distribution between the electrodes and cause instability. The main difference is, of course, that we have a sheath edge instead of their anode. Also the vaporization of anode material (this makes it difficult to calculate the neutral particle density between the electrodes) is substituted for the dense neutral gas in the boundary layer of the stagnated shock.

The modification of their breakdown theory to fit our case will be presented briefly. Consider the field emission equation (Eq. 5.111),

$$J_E = AE^2 e^{-\frac{B}{E}},$$
(7.1)

where A and B are constants. Let $E = E_p + E'$, where E_p is the initial field and E' is the field due to the additional positive ion space charge (ions created by ionizing collisions of field emission electrons) measured at the cathode surface. Because of the steepness of the dependence of current on field, $E' \ll E_p$ and by expansion we find,

$$J_E = AE^2 e^{-\frac{B}{E_p}} e^{\frac{BE'}{E_p^2}}.$$
(7.2)

From the Poisson's equation,

$$\frac{1}{r}\frac{d}{dr}\left(r(E_p + E')\right) = \frac{n_i e}{\varepsilon_c} = \frac{J_i + J'}{2\pi r \varepsilon_0 \mu_i (E_p + E')}$$
(7.3)

or
$$\frac{d}{dr}(r^2 E_p E') = r E_m'^2,$$
(7.4)

where $E_m^{'2} = J'/2\pi\varepsilon_0\mu_i$, J_i is the initial ion current per unit length of the cathode and J' is the extra positive ion current arising from J_i.

Since the change in sheath thickness is negligible,

$$E' = -\frac{E_m^{'2}}{2E_p}\left(\frac{r_s^2}{r^2} - 1\right) \qquad (7.5)$$

or at the cathode surface,

$$E_p' = \frac{E_m^{'2}}{2E_p}\left(\frac{r_s^2}{r_p^2} - 1\right) \equiv CJ', \qquad (7.6)$$

where $C = ((r_s/r_p)^2 - 1)/4\pi\varepsilon_0\mu_i E_p$. The breakdown condition is,

$$J_E\left(e^{n_0 Q_i(r_s - r_p)} - 1\right) = J'. \qquad (7.7)$$

From Eqs. 7.2, 7.6 and 7.7, we obtain,

$$2\pi r_p A E_p^2 e^{-\frac{B}{E_p}} e^{\frac{BCJ'}{E_p^2}}\left(e^{n_0 Q_i(r_s - r_p)} - 1\right) = J'. \qquad (7.8)$$

Breakdown occurs when the plots of the right and left hand side of Eq. 7.8 are tangent, i.e.,

$$\frac{ABr_p e\left(e^{n_0 Q_i(r_s - r_p)} - 1\right)\left(\left(\frac{r_s}{r_p}\right)^2 - 1\right)}{2\varepsilon_0\mu_i E_p} e^{-\frac{B}{E_p}} = 1. \qquad (7.9)$$

Equation 7.9 is a very strong function of E_p and the exact value of E_p required. In our experiment, however, E_p is obtained after lengthy calculations and might have a considerable amount of error. In addition, this theory neglects the double sheath effect. Therefore it does not seem worth while to test our results with the condition of breakdown of Eq. 7.9.

The effect of temperature in the range of room temperature to the neighborhood of 1000°C was studied by Bowder (7.5) and Alston (7.6). In this temperature range, if the gas density is kept constant and if the electrical field is uniform, the breakdown voltage was rather insensitive

to the gas temperature.

In 1961 and 1964, Sharbaugh, Lee and others (7.7) measured the breakdown voltage of a plasma produced by a pressure driven shock tube, and observed a breakdown voltage as low as 50% (at 4000°K) of that predicted by Paschen's Law. Exact theoretical analysis has not been made. The electron density was the order of 10^{10} cm^{-3} which indicated that the thickness of the cathode sheath across which most of the potential difference was applied became comparable to the hydrodynamic boundary layer formed along the shock tube wall. However, the neutral particle density (to which first ionization coefficient is proportional) inside and outside the boundary layer was not known.

Lee et. al. also have concluded that for a high density plasma ($> 2 \times 10^{10}$ cm^{-3}), thermal breakdown takes place instead of dielectric breakdown, i.e., after the initiation of breakdown and while the breakdown process is developing, a great amount of energy (- 100 KW) is supplied to the gas and further ionization takes place which leads to the complete full path breakdown.

The electric field at the cathode surface of - 2×10^{5} V/cm may seem a bit low for the field emission. This field strength, however, is enough as supported by existing experimental results by many people other than the results obtained in Sec. 6.2. The value of electric field of the order of 10^{4}-10^{5} V/cm was reported by Llewellyn Jones and Morgan (7.8) and Morgan and Harcombe (7.9) in studies of enhanced electron emission from cold electrodes in gases, in agreement with the estimates made on the basis of the Fowler-Nordheim equation by Kerner and Raether (7.10) from their measurements of electron emission from cold metals under electric fields of the order of 10^{4} V/cm. Calvert (7.11) also reported a cold

emission of electrons under electric fields of $3-8 \times 10^4$ V/cm. His estimated emitting area of the electrons was 10^{-14} cm^2. Penning and Mulder (7.12) and Lamar and Compton (7.13) observed the field emission at 2.5×10^4 and 7.6×10^4 V/cm or more, respectively.

(7.2)   R.N. Varney, H.J. White, L.B. Loeb & D.Q. Posomin: Phys. Rev. 48 818 (1935)

(7.3)   R.W. Crowe, J.K. Bragg & V.G. Thomas: Phys. Rev. 96 10 (1954)

(7.4)   L.H. Germer & F.E. Haworth: Phys. Rev. 73 1121 (1948)
L.H. Germer & F.E. Haworth: J. Appl. Phys. 20 1085 (1949)
L.H. Germer: J. Appl. Phys. 22 955 (1951)
L.H. Germer & J.L. Smith: J. Appl Phys. 23 553 (1952)
W.P. Dyke & J.K. Trolan: Phys. Rev. 89 799 (1953)
P. Kisliuk: Phys. Rev. 92 847 (1953)
P. Kisliuk: J. Appl. Phys. 25 897 (1954)
W.S. Boyle & P. Kisliuk: Phys. Rev. 97 255 (1955)
W.S. Boyle, P. Kisliuk & L.H. Germer: J. Appl. Phys. 26 720 (1955)
W.S. Boyle & F.E. Haworth: Phys. Rev. 101 935 (1956)
R.N. Bloomer & B.M. Cox: Vacuum 18 379 (1968)

(7.5)   H.C. Bowder: Proc. Phys. Soc. 43 96 (1931)

(7.6)   L.L. Alston: Proc. IEE (london) 105 pt. A 549 (1958)

(7.7)   A.H. Sharbaugh, P.K. Watson, D.R. White, T.H. Lee & A. Greenwood: AIEE Trans. pt. 3 PAS 80 333 (1961)
T.H. Lee, A.N. Greenwood & D.R. White: IEEE Trans. PAS 84 1116 (1965)

(7.8)   F. Llewellyn Jones & C.G. Morgan: Proc. Roy. Soc. A218 88 (1953)

(7.9)   C.G. Morgan & D. Harcombe: Proc. Phys. Soc. B66 665 (1953)

(7.10) K. Kerner & H. Raether: Z. angew. Phys. 6 212 (1954)

(7.11) W.J.R. Calvert: Proc. Phys. Soc. B69 651 (1956)

(7.12) F.M. Penning & J.G.W. Mulder: Physica 2 724 (1935)

(7.13) E.S. Lamar & K.T. Compton: Phys. Rev. 37 1069 (1931)

CHAPTER VIII   CONCLUSION

The electrical breakdown phenomenon between two electrodes changes
drastically when there is a plasma surrounding these electrodes. One of
the results of this change is the lowering of the breakdown voltage (it
decreased to 40 volts or less which was much less than Paschen's minimum
breakdown voltage (Secs. 6.1 and 6.6)). It was assumed that this breakdown
phenomenon was due to electrode surface contamination. Experimental work
proved that this assumption was correct (Sec. 6.3). If the total charge
accumulated on the electrically insulating surface layer reached a
certain amount, then the field in the layer became intense enough to cause
the electron avalanche, which led the system to the full path breakdown.
Therefore the breakdown condition was that the integral of the pre-breakdown
electrode current from time zero to the time when breakdown occured was some
constant value and was independent of the applied voltage.

Consequently if the electrode surface had been clean the breakdown
voltage should have been higher than Paschen's minimum value. Therefore
the electrode was cleaned well by heating to 2300° C (Sec. 5.3.7) and the
measurements were carried out; the breakdown occured at 40 volts again.
There must be some other mechanism to cause the breakdown. The next
hypothesis was that this phenomenon was due to the hot cathode arc
discharge. The plasma density (which is roughly proportional to electrode
current) against breakdown voltage curve of Fig. 6.12 nicely coincided
with the well known V-I characteristic of the breakdown, especially with
the transition region from abnormal glow discharge to arc discharge. If

this was the case then the negative electrode (or cathode) should have been heated by the ion bombardment to a temperature high enough for thermionic electron emission. In some cases the energy input rate, $I_i V_p$, into the 0.1 mm diameter cylindrical electrode reached 1000 watts, which appeared abnormally large. After some calculations, however, it was found that the energy loss by heat conduction into the metal was so large that the cathode temperature rise was only $10°C$ at most (Sec. 5.4.5). Thus the hot cathode arc hypothesis was proved invalid.

Many effects happening in the sheath region such as current pinching, oxide surface layer, local heating by ion bombardments, etc. were tested (Secs. 5.1.6, 5.1.8, 5.1.9, 5.3.9, 5.4.6, 5.4.7) to explain this peculiar breakdown phenomena, in vain. The last hypothesis was to assume cold-cathode arc where the field emission of electrons from the cathode dominates the situation. From rough calculations, the intensity of the field at the cathode surface was only approximately 10^4 V/cm, which was too low for field emission. However, after careful examination of the neutral density change in the incident and stagnated shock as well as in the boundary layer around the electrode, the ionic mobility was found to be considerably lower than that used in the rough calculations, and this increased the field intensity by approximately ten times. Also this increase in neutral particle density enhanced the ionizing collisions of neutrals by secondary electrons and brought the resultant field to about 5×10^5 V/cm. This intensity could be considered to be strong enough for field emission by looking into the supplementary experiments (Sec. 6.2) and many reports of vacuum breakdown experiments (Sec. 7.4). In addition, this electric field strength at the cathode was constant over a wide range of plasma density (10^9-10^{16} cm^{-3}) and initial pressure (0.1-10 mmHg). Thus the

breakdown mechanism was finally made clear.

The application of the theory of the breakdown mechanism developed in this thesis is virtually limitless. The most important application arises, as mentioned in Chapter I, to the reignition phenomena after current zero of an alternating-current circuit breaker where the electrodes are surrounded by the high density post-arc plasma. Also this theory is applicable to the mechanisms of the unipolar arc discharge as well as the vacuum breakdown and the analysis of electrostatic probe current in a dense plasma.

During the course of this research work many other valuable results were also obtained. One of them is the development of a new technique of determining the electrical conductivity of plasma by using radio frequency magnetic fields (Sec. 3.2.5). In section 4.2 a new theory which predicts the variation of the plasma velocity is introduced, with good agreement with the experimentally obtained values (Sec. 4.3.1). Also in sections 4.3.2-4.3.7 many properties of the plasma produced by the electromagnetically driven shock tube were carefully examined by many diagnostic techniques and the validity of the shock relations was tested.

Section 2.7 describes a generalized floating double probe theory as well as an interesting application of the double probe to measure a low density plasma (-10^7 cm^{-3}). The ion current to the probe which was aligned parallel to the plasma flow was measured in the case of continuum high speed plasma flow and an explanatory theory was developed (Sec. 2.6.4).